January 2018

Polarized Localization Microscopy (plm) Detects Nanoscale Membrane Curvature And Induced Budding By Cholera Toxin Subunit B (ctxb)

Abir Kabbani
Wayne State University, abirmk24@gmail.com

POLARIZED LOCALIZATION MICROSCOPY (PLM) DETECTS NANOSCALE MEMBRANE CURVATURE AND INDUCED BUDDING BY CHOLERA TOXIN SUBUNIT B (CTxB)

by

ABIR KABBANI

DISSERTATION

Submitted to the Graduate School

of Wayne State University,

Detroit, Michigan

in partial fulfillment of the requirements

for the degree of

DOCTOR OF PHILOSOPHY

2018

MAJOR: PHYSICS

Approved By:

_____

Advisor Date

_____

_____

_____

_____

_____

DEDICATION

I dedicate this work to my loving parents, my husband Mohamad, my sisters, and my special friend for their continuous support, encouragement, and for believing in me. Specially, I dedicate my dissertation to my kids, Mostafa and Abdallah.

DECLARATION

I, Abir Kabbani, declare that this dissertation titled, Polarized Localization Microscopy (PLM) Detects Nanoscale Membrane Curvature and Budding Induced by Cholera Toxin Subunit B (CTxB) and the work reported in it are from my own original research.

I confirm that:

- This work was done wholly or mainly while in candidature for a research degree at Wayne State University.
- Where any part of this dissertation has previously been submitted for a degree or any other qualification at this University or any other institution, this has been clearly stated.
- Where I have consulted the published work of others, this is always clearly cited.
- Where I have quoted from the work of others, the source or reference is always provided or cited. With the exception of such quotations, this dissertation is completely my own work.
- I have acknowledged all main sources of help.
- Where the dissertation is based on work done by myself jointly with others, I have made clear exactly what was done by others and what I have contributed myself.

ACKNOWLEDGEMENTS

I would like to start by thanking our department chair Prof. David Cinabro (current) and Prof. Ratna Naik (former). I am thankful to Prof. Naik and Prof. Jogindra Wadehra for their heartwarming welcome into the physics department. Their advice for registering the required courses, and kind support in putting together my plan of work for the degree was especially helpful.

I would like to express my sincere gratitude to my advisor Dr. Christopher V. Kelly for his continuous support of my Ph.D. research, the countless research discussions, his patience, immense knowledge, and understanding. I joined Dr. Christopher V. Kelly's research group in 2012. I am honored to be working side by side with a smart, talented, research driven, and enthusiastic professor as my research advisor. Under his supervision, I learned the various imaging and microscopy techniques as I entered the interdisciplinary field of biophysics. He was always available to engage in research discussions, answer any question, and alleviate any ambiguity. He encouraged and provided me with a great opportunity to learn about the cutting-edge research, and to meet with great scientists while attending the Biophysical Society Meetings. I could not have asked for a better Ph.D. mentor. His guidance enabled me to conduct research, think independently, and solve problems. Conducting experiments, writing, publishing the results, and completing this dissertation would not have been possible without his help. I was very fortunate to have the honor to work with Dr. Kelly as my advisor.

I would also like to thank my thesis committee: Prof. Peter Hoffman, Prof. Takeshi Sakamoto, and Prof. Bhanu P. Jena, for their insightful comments, helpful assistance in editing, and reviewing my thesis. I also appreciate their valuable time spent on reading and evaluating my work.

I’m very grateful to obtain the Thomas C. Rumble and the Summer Dissertation Fellowships from the graduate school while I was in the Ph.D. program. I’m very thankful to the research assistant support from Dr. Kelly’s startup funds, and the teaching assistantship (GTA) from the Department of Physics and Astronomy. I earned a great experience by teaching the undergraduate laboratories, discussion sections, and quiz classes. I would like to thank Dr. Scott Payson, the faculty members, my colleagues, and the department staff for their guidance and support in preparing the labs and class materials. Special thanks are due to my friends Laura Gunther, Utsab R. Shrestha, Chris Zin, Rebecca Meerchaert Culcasi, Eric Stimpson, and Doaa Taha for their relentless support. I had a great time working with our former and past lab group members. Specially, I appreciate our group meetings as I find them an opportunity to learn something new.

Apart from my academic career, I would like to thank my family for supporting me throughout my educational path. I am very thankful to my husband for encouraging me to purse my dream of earning a Ph.D. in Physics, and for understanding me.

PREFACE

This dissertation presents the outcome of five years of research work carried out to pursue a Ph.D. degree at the department of Physics and Astronomy, Wayne State University. The main goal of this study is to understand the biophysics of cell membranes. In particular, understand the nanoscale changes in membrane structure for various cellular processes and the dynamics of biomolecules. All experiments were carried out by me and performed at Wayne State University. The work presented here mainly demonstrate the enhanced ability of detecting nanoscale membrane curvature by Polarized Localization Microscopy (PLM), and the discovery of cholera toxin effect on the membrane. PLM is a novel microscopy technique developed by our lab to overcome current experimental limitations in studying nanoscale membrane curvature. The microscopy setup, theory, experimental methods, data analysis, and the interpretation of the results in comparison to simulations, use the broad knowledge of physics to understand biological systems.

This dissertation starts with a brief introduction regarding cell membrane components and lipids behavior discussed in Chapter 1. Chapter 2 discusses the available microscopy techniques and their limitations in detecting nanoscale membrane curvature, driving the need for a novel technique that enables the detection of nanoscale membrane deformation, given by PLM in Chapter 3. The enhanced resolution, and membrane orientation information, provided by PLM allowed the discovery and the first direct report of visualizing nanoscale membrane budding induced by Cholera Toxin Subunit B. This is mainly discussed in Chapter 4. The importance of crosslinking, valency, and their effects on membrane structure are described in Chapters 5 and 6. Finally, a collective summary of the dissertation subjects is discussed in Chapter 7.

TABLE OF CONTENTS

LIST OF ABBREVIATIONS

MLV Multi Unilamellar Vesicle

SLB Supported lipid bilayer

GUV Giant unilamellar vesicle

LUV Large unilamellar vesicle

SUV Small unilamellar vesicle

Lo Liquid ordered

Ld Liquid disordered

NP Nanoparticle

SPT Single particle tracking

TIRFM Total internal reflection fluorescence

PALM Photo activated localization microscopy

STORM Stochastic optical reconstruction microscopy

WT Wild Type

AF Alexa fluor

POPC 1-palmitoyl-2-oleoyl-sn-glycero-3-phosphocholine

GM1 Monosialotetrahexosylganglioside

DiI 3-dimethyl-1-octadecylindole

DPPE-Rh 1,2-dihexadecanoyl-sn-glycero-3-phosphoethanolamine Rhodamine

DOPC 1,2-dioleoyl-*sn*-glycero-3-phosphocholine

DPPC Dipalmitoylphosphatidylcholine

PLM Polarized localization microscopy

NA Numerical aperature

SNR Signal to noise ratio

r_{NP} Radius of nanoparticle

SMLM Single Molecule Localization Microscopy

LIST OF SYMBOLS

D	Diffusion rate
λ	Wavelength
β	Polar tilt angle
σ	Uncertainty
exp	Exponential
θ	Polar angle
ψ	Rotation angle
φ	Azimuthal angle
r	Radius

LIST OF FIGURES

CHAPTER 1 INTRODUCTION

1.1 Cell membrane

The cell is a complex machine and a fundamental building block of life. This highly organized submicron structure possesses various components, subcellular structures, and organelles. The attributes of this unit of life are countless including growth, energy transformation, and replication. The plasma membrane encloses the cell, define its boundaries, maintains its components, organizes the transport of molecules, and performs various biological functions such as endocytosis/exocytosis and trans-membrane signaling. The unique structure and composition of the membrane facilitates its complex functional role. The supramolecular assemblies and composition of proteins, lipids, and cholesterol is critical for the membrane specific function. Biological membranes consist mainly of a thin lipid bilayer film that serves as an impermeable barrier to most water-soluble molecules and proteins. The lipid bilayer maintains its structure via hydrophobic interactions which is critical for the assembly of the lipids and the permeability properties of the membrane. Further, the biological structure of the membrane is conserved via weak forces such as covalent hydrogen bonds, ionic bonds, hydrophobic interactions, Van der Waal forces, and attractive forces between molecules. These week chemical forces ensure the structural stability of the membrane at physiological conditions. Membrane continuous thermal fluctuations impart stability across the bilayer by allowing molecules to explore more space, and to exist in close proximity with neighboring molecules allowing some bonds to form or break with time.

1.2 Lipids

The amphiphilic nature of lipids make them a suitable component of the plasma membrane representing ~70% of its mass[1]. Lipid molecules have a polar hydrophilic head group “water-

loving" and a hydrophobic nonpolar "water-fearing" tail. The tails of the lipids may vary in length and shape. For example, the presence of an unsaturated double bond results in a kink in the lipid tail and resistance to order molecular packing (Fig. 1). The saturation level of the tails determine the lipid transition temperature. The specific properties of each lipid reflects its fitness to serve in a specific membrane mechanism such as membrane bending during viral infection. If dispersed in aqueous solution it is energetically favorable for the amphiphilic lipids to aggregate and form a micellar structure where the hydrophobic tails are enclosed between the hydrophilic head groups. Multi unilamellar vesicles (MLVs) also assemble spontaneously upon exposing lipids to aqueous environment. Lipid bilayers can me created artificially, as discussed later, or extracted from cells (Giant Plasma Vesicles (GPV)). One of the most important aspect of the two dimensional lipid bilayer is fluidity; lipids and other membrane-incorporated molecules laterally diffuse within the membrane.

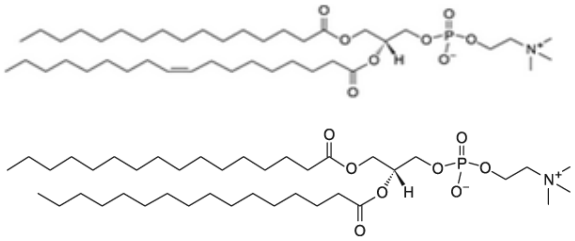

Figure 1. Lipid structure with varying tail saturation level. (A) POPC lipid and (B) DPPC lipid. The difference in the lipid tail saturation results in differing phase preferences and T_m for these lipid molecules where Tm is -2 ºC and 41 ºC for (A) and (B), respectively.

To mimic the complex composition of the cell membrane and understand its structural and functional role, a wide variety of natural or synthetic lipids can be used. Some of the lipids major classes are: phospholipids, sphingolipids, and sterols. Phospholipids possess two long hydrocarbon chains with a hydrophilic phosphorylated head group with a glycerol backbone, while the sphingolipids have sphingosine head group instead. Cholesterol belongs to the sterol class with a rigid ring structure and a small head group. Most lipids can also be bio-synthesized or purchased

for a bilayer assembly in vitro. Utilizing a binary or a ternary mixture of phospholipids, sphingolipid, and cholesterol results in phase separation with co-existing domains of liquid-ordered, liquid-disordered, or gel phases at specific temperatures. Lipid packing in ordered/disordered/ or gel compartments strongly depend on the lipids tail saturation and transition temperature. For lipids with low transition temperature i.e. they are in the fluid state at room temperature with unsaturated tails tend to partition in liquid disordered phase. While lipids with high transition temperature and high level of saturation of the tails preferentially partition in liquid ordered phase.

1.3 Lipid phases

Liquid ordered phase (L_o) is a crystalline fluid phase of the lipid bilayer strongly dependent on cholesterol and saturated lipids. The nanoscale area enriched with highly ordered, closed packed lipids, is generally attributed and associated with lipid rafts. The unique intrinsic properties of the small rigid cholesterol molecules is suitable for them to fill in the voids between the tails of the lipids within this L_o region. Cellular membrane components assemble into specialized domains known as lipid rafts that is composed of a heterogeneous sterol- and sphingolipid-enriched domain (Fig. 2), which facilitate molecular sorting in vitro[2]. Lipid rafts have been implicated in a variety of fundamental cellular mechanisms such as transmembrane signaling[3]. Some membrane-bound proteins are bound to lipid rafts which serve as a platform for membrane signaling. Lateral segregation by rafts is mediated by cholesterol molecules that favors interactions with saturated lipid tails forcing lipids to segregate and form domains. Despite extensive experimental data, there exist no clear confirmation of the existence of such region over a long range of time. However, it is hypothesized that such rafts form and dissipate within a short period of time, while a membrane signaling or internalization event occur.

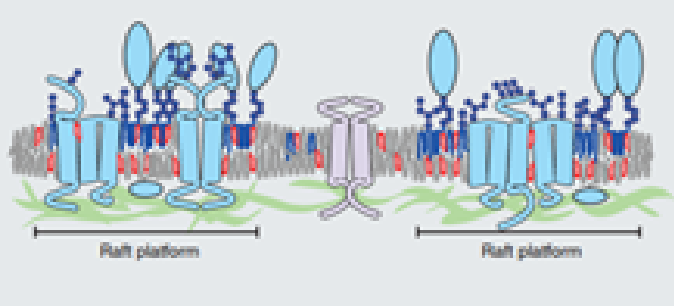

Figure 2. Lipid raft platform. Lipid rafts are made up of GPI-anchored protein, transmembrane proteins and cholesterol[2].

The gel phase is a higher order packing version of the liquid ordered phase, also sometimes referred as "the solid phase". Lipids in this phase have long extended saturated carbon tails, are less fluid, highly ordered, closely packed, periodic, locked in position, and restricted in their orientation. The liquid disordered phase (L_d), on the other hand, is a cholesterol deficit, unsaturated lipid rich fluid bilayer phase. The lipid tails are randomly oriented, loosely packed, allowed to explore more space, and undergo free non- restricted diffusion.

Each phase possess unique properties of diffusion, packing, composition, thickness, bending rigidity and shape[4]. Generally, lipids undergo free diffusion in the L_d phase, while they experience restricted diffusion in the L_o and gel phases. Closed packed, long saturated carbon tail lipids tend to be enriched in the in L_o and gel phase increasing the stiffness of the bilayer. Thus the length of the existing lipids in each phase affect the bilayer core thickness, resulting in a substantial thickness mismatch between the L_o and gel thick phases in comparison to the L_d phase[5]. Further, the boundary shape of the different phases is affected by the rigidity of each. Circular fluid L_o compartments in an L_d background, and vice versa, have been visualized on giant unilamellar vesicles (GUVs)[6]. However, gel phase tend to have a more rigid structure, less diffusing, sharper shape boundary than the other fluid phases[7]. Temperature, lipids composition, and cholesterol concentration, and line tension are critical factors in determining the phase state of the bilayer and the possibility of phase co-existence. It is critical to understand the lipid tail length and degree of

unsaturation and it's relation with phases as it's associated with its impact on the membrane structure, function, and behavior.

1.4 Model membranes

Model membranes are frequently used to probe the fundamental properties of the cell membrane structure and the particular effects of membrane proteins, sterols, and sphingolipids. Model membranes can be fabricated by several methods, in a variety of vesicle sizes, or as a planar supported lipid bilayer (SLB). Free floating bilayers are more biologically relevant due to the decreased interaction between the bilayer and the substrate, however, there are also some disadvantages associated with such systems in regards to limitations in imaging. Substrate-free synthetic bilayers include: giant unilamellar vesicles (GUVs) and black lipid membranes (BLM). GUVs are giant liposomes (~<100 μm in diameter) created by electro formation where a dried lipid film of desired composition is placed on an ITO plate, and exposed to an alternating electric field. Blistering of the liposomes away from the flat film is observed over the course of incubation. Whereas, BLM is created over an aperture of hundreds of microns in size by spontaneous assembly of the dispersed lipids as the aperture is dropped into the aqueous solution. The disadvantage of such a system is the presence of defects and oils within the membrane. Planar bilayers are a powerful system, widely used for the convenience of imaging a two dimension hundreds of microns size area, while testing biological phenomena with the desired controlled molecular components. The creation of a SLBs on glass is performed by the fusion of vesicles (small or large vesicles) on a plasma cleaned glass dish forming a continuous bilayer. Small unilamellar vesicles (SUVs) are vesicles of diameter that ranges from 30 to 50 nm. Preparation of SUVs incorporates mixing of non-fluorescent phospholipids (e.g. POPC, DOPC, etc..) and fluorescent lipids for molecule tracking and bilayer visualization by fluorescence microscopy (e.g., DPPE-Rhodamine).

Adding an aqueous solution to the dried lipid mixture initiate the formation of MLVs, while when followed by rigorous sonication these MLVs will break down into smaller nanometer unilamellar structures (SUVs). The desired size of the resulting unilamellar vesicles is determined by the preparation technique. For instance, to obtain large unilamellar vesicles (LUVs) with diameter of 100-300 nm, extrusion is required. Basically, passing the MLVs repeatedly through a polycarbonate membrane filter of a specific pore size results in a more consistent size distribution of the created LUVs.

1.5 Membrane substrate interaction

In order to decrease the membrane substrate interactions, several membrane cushions have been utilized to eliminate the contact between the created bilayer and the underlying glass. Some widely implemented substrates include agarose thin films[8,9], polymers such as Polydimethylsiloxane (PDMS) films, Poly (methyl methacrylate) (PMMA), Poly-l-lysine (PLL), and tethered bilayers by DNA or polyethylene glycol (PEG) lipids. These systems are highly desirable for their high efficiencies, unique properties of providing minimal background fluorescence, and having minimal interactions with the membrane. It is critical to utilize membrane cushions in the case of studies that incorporates transmembrane proteins, helix inserting proteins, membrane structure change, and lipid phase micro domain segregation.

1.6 Membrane Curvature

Membrane bending is an active membrane activity that is dynamically fostered by changes in lipid composition[10], line tension[11], protein helix insertion[12], creation of lipid rafts, leaflet mismatch[13], and the sorting of phospholipids and membrane proteins[14]. For instance, the amino-terminal homology of Epsin 1 (ENTH) binds to phosphatidylinositol-4,5-bisphosphate (PtdIns(4,5)P_2) lipids and insert an amphipathic helix (helix0) into the membrane[15]. ENTH

influence the membrane shape by increasing the membrane outer leaflet area, thus causing a convex curvature. Similarly, proteins with BAR (bin, Amphiphysin, Rvs) domains tend to force the membrane to bend upon binding to accommodate the physical structure of the protein. Moreover, it has been demonstrated that the lateral pressure generated by the repulsion between closely packed bound proteins drives membrane bending, thus protein densities on the membrane surface induces curvature and tubulation.

The 2D fluid membrane can take on a 3D shape in space, which is mainly described by the concept of principal curvatures. At each point in space, there exist two principal curvatures that characterizes the shape of the membrane at each location. The two principal curvatures denoted by c_1 and c_2 are inversely proportional to the principal radii R_1 and R_2, and their product is defined as the Gaussian curvature. Determination of the principle curvatures is an indicator of the cellular processes. For instance, in clathrin-dependent endocytosis the membrane is curved into a sphere with a smooth connecting neck between the spherical vesicle and the surrounding bilayer. Such structure would possess a positive Gaussian curvature at the top of the sphere with a negative Gaussian curvature at its neck. Other biological mechanisms include vesiculation or tubulation. The principal curvatures indicates the shape of the membrane curvature such as a positive or negative Gaussian surface, a saddle point, a plane, or a cylinder.

The energy required to bend the membrane at any point is described by Helfrich free energy model such that:

$$E_{Bend} = \int (\kappa(H - H_0)^2 + \bar{\kappa}K)dA\ . \qquad \text{(Eq. 1)}$$

This integral incorporates the membrane bending rigidity (κ), membrane Gaussian curvature modulus ($\bar{\kappa}$), the mean local membrane curvature (H), the local Gaussian curvature (K), and the intrinsic membrane curvature ($H_0 \approx 0$) and the area of the desired membrane structure (A).

The interplay between cellular membrane deformation and the diverse biological processes makes membrane curvature a prime player in membrane trafficking. Formation of membrane domains is associated with the redistribution of membrane-bound proteins and phospholipids. Investigations of the mechanisms of curvature-sensing and curvature-generating proteins such as Epsin[16] has been driven to study bacterial localization and internalization process into the cell. Bacterial toxins, including cholera toxin and Shiga toxin, have been reported to partition on negative curvature regions and segregate from positive ones[17]. Further, Studies have showed that membrane bending is invoked by chemical organization. Membrane geometry is altered due to phase separation of phospholipids, a consequence of the bending rigidity difference between the two regions[18]. Some lipids possess an intrinsic curvature or a curvature preference. For instance, lipids with smaller head group such as dioleyl phosphatidylethanolamine (DOPE) are represented by an inverted cone shape which preferentially partition in negative curvature regions allowing the small head groups to be closely packed with a larger volume for the tails to explore. However, lipids with larger polar head group and shorter acyl chain are represented by a cone, and tend to partition at positive curvature regions allowing the head group to explore more area while possessing a crowded hydrophobic core.

The shape of the membrane and its curving mechanism is important in countless cellular processes, in particular, the size of the curvature region is also important. Nanoscale Membrane curvature is a critical component in many biological processes such as presynaptic vesicle fusion[19], endocytosis/exocytosis, trans-membrane signaling, lipid phase dynamics[18], antimicrobial peptides, infection and egress of envelope viruses such as via HIV-1 Gag[20] ,SNARE proteins [21], and interferon-inducible transmembrane proteins[22]. Thus detecting and resolving nanoscale membrane

curvature is a critical component in understanding basic functions of trans-membrane molecules, viruses, membrane bound proteins and lipids.

The change in membrane structure affects the biophysics of its constituents. The lateral sorting of membrane lipids and proteins coupled with membrane curvature in an interdependent manner. The initiation and regulation of complex cellular processes are induced by membrane curvature such as membrane bending by curvature sensing proteins. For example, endocytosis, exocytosis, transmembrane signaling, and membrane-binding toxins are all hypothesized to be largely regulated by these fundamental biophysical properties of the membrane. Further, many physiological processes depend on both the nanoscale membrane curvature and lipid phase[23]. For instance, the interplay of membrane phase and curvature have been demonstrated with envelope viruses that 40-100 nm diameter [24], dynamin-regulated vesicles that are 60-80 nm diameter[25], and vesicle fusion events requiring local membrane radii of curvature as small as 20 nm [26]. Therefore, exploring the effects of membrane heterogeneity and curvature with various proteins is critical to understand cellular processes and the mechanisms they are governed by.

CHAPTER 2 IMAGING TECHNIQUES

2.1 TIRF Microscopy

Several fluorescence-based imaging techniques have been implemented to observe the cell membrane and study its dynamics through observing fluorescent membrane probes within. Fluorescence occurs when an electron in the excited singlet state is paired to an electron in the ground state with opposite spins. The electron is initially excited by the absorption of light by the fluorophore. As the electron decays from the excited singlet state to the ground state, it emits a photon. The emission photon is of longer wavelength than the excitation photon due to vibration relaxation. The emission is chromatically filtered to reveal the location of the fluorophore. More sophisticated microscopy techniques are utilized depending on the desired sample such as total internal reflection fluorescence microscopy (TIRFM).

TIRFM is an optical imaging technique that utilizes the evanescent wave generated at the glass-oil interface in the high numerical oil emergent objective. TIRF is achievable when the excitation light beam is off centered from the back focal plane of the objective, it passes through the objective lens, the immersion oil, before it reaches the sample placed on the glass coverslip. The propagating laser beam encounters the glass-sample interface, where the index of refraction of the sample (e.g. aqueous buffer n_s ~ 1.38) is less than the index of refraction of the glass coverslip (n_g = 1.5), the incident light beam will undergo refraction. Further, if the incident angle was greater than the critical angle given by Snell's law:

$$\sin(\Theta_c) = n_s/n_g \qquad \text{(Eq. 2)}$$

the propagating beam will be totally internally reflected back to the first medium with a generated electromagnetic field that propagates parallel to the interface. The generated evanescent wave travels in x-y direction with an exponentially decaying z component. The decaying nature of the

evanescent electromagnetic field allows the selective illumination and excitation of samples within close proximity to the glass substrate. The selective excitation of the fluorophores within the sample is enabled by the TIRF range, in which the probability of exciting a fluorophore at a distance d from the coverslip decays exponentially. The TIRF range, the depth of the evanescent field denoted by "d", depends on the excitation light wavelength, critical angle, and the two refractive indices of the media at the interface according to the following equation[27,28]:

$$d = \frac{\lambda_{exc}}{4\pi\sqrt{n_s^2 * \sin\Theta^2 - n_g^2}} \quad \text{(Eq. 3)}$$

where λ_{exc} is the excitation wavelength, and Θ is the incident excitation light propagation angle. In particular, decreasing the background fluorescence of thick samples such as cells prohibiting the observation of any fluorescence molecules that exist on a z greater than 50-100 nm. This lead to an increase in the signal to noise ratio of the detected fluorescence signal as well as enabling the detection of faint molecules. TIRFM is commonly used to investigate the plasma membrane of cells and the interaction of molecules at the cellular surface providing visualization of key events occurring at the sample surface. TIRFM has been used to detect and characterize the dynamics and stages of granules fusion[29–31]. Although TIRF microscopy provides better images with less background noise than the typical fluorescent microscopy, but it fails to detect nanoscale curvature regions and distinguish between regions of positive and negative membrane curvature at the cell membrane.

2.2 Polarized TIRFM

Polarized TIRF microscopy is usually applied to probe and detect membrane bending regions. Light is an electromagnetic wave that exhibits polarization. The evanescent electric field wave vector's direction is parallel to the coverslip and linear polarization enables s- and p-polarized excitation light. Polarization parallel to the plane of incidence is p-polarized, while the component

perpendicular to the plane of incidence is s-polarized. pTIRF microscopy is based on the principle of selectively exciting fluorophores in the membrane with p- or s- polarized light independently. Illuminating the sample with polarized excitation light will excite the fluorophores whose dipole moments are aligned with the electric vectors of the polarized light. S-polarized light will excite the fluorophores with dipole moments that are parallel to the coverslip. On the other hand, p-polarized light will only excite the fluorophores with dipole moments perpendicular to the coverslip. Membrane bending regions are highlighted by a combination of emission from p- and s-polarized excitation, mainly detected in p-polarized excitation. The combination of both polarizations demonstrates the total local fluorophore concentrations independent of fluorophore orientation. pTIRFM provides a high temporal resolution in the observations of membrane processes that involves membrane topology change, a sequence of images acquired in p- and s-polarized excitation demonstrates the local membrane deformation as it occurs with time. Sub micrometer membrane change can be visualized and rapid variation in membrane structure can be reported as observed for granule vesicles fusion[32].

One key component to pTIRFM is utilizing a membrane probe sensitive to excitation light polarization. For instance, indocarbocyanine dyes (e.g. 1,1'-Dioctadecyl-3,3,3',3'-Tetramethylindocarbocyanine Perchlorate ($DiIC_{18}$)) are lipophilic membrane stains with a unique molecular structure. The lipid probe structure mainly consists of two indoline rings at each terminal of the head group connected with a conjugated 3-carbon bridge and two methyl group, and two alkyl hydrocarbon tails. A wide variety of this tracer is available with varying saturation level of the hydrocarbon tails denoting the lipid phase preference of the label. Other analogs of the dye with varying bridge length and atoms in the terminal rings exhibit different spectral properties. DiI molecular structure and head group configuration prohibit the molecule from exploring all

orientations in space within the membrane[33], providing an effective transition dipole moment parallel to its head group. Selective excitation of parts of the membrane is possible upon incorporating this tracer allowing it to diffuse, stain the membrane, and maintain its transition dipole moment within the plane of the membrane. Therefore, DiI that is in curved membranes perpendicular to the coverslip will preferentially be excited by p-polarized incident light. While, s-polarized light will excite DiI that is in the membrane parallel to the coverslip twice as brightly as DiI in membrane that is perpendicular to the coverslip. Measuring the overlap between DiI's dipole moment and the linearly polarized excitation light, enables the detection of membranes of varying orientations [34]. pTIRF microscopy has been used recently to study the details of presynaptic vesicle fusion[35], endocytosis/exocytosis[34],interactions of peptides with model membranes[36], the rotation of motor proteins[37], peptide binding to membrane-associated receptors[38], and the effects of hydration on membrane structure[39]. The ratio of the emission from p-polarized excitation (*P*) divided by that from s-polarized excitation (*S*) reveals the membrane perpendicular to the coverslip while the intensity *P+2S* reveals the total fluorophore density[40]. However, all current uses of pTIRF microscopy utilize diffraction limited resolution, which prohibits the resolution of vesicle size below 200 nm. Biological structures range in size from few nanometers to several microns, current microscopy techniques such as pTIRFM proved to be powerful in detecting local membrane deformations however limited to sizes >200nm. This limit is dictated by the Abbe diffraction limit for microscopes, in particular, a single nanometer spot will appear as a blur Airy disk image of few hundred nanometers in radius (named point spread function (PSF)) due to the optics of the microscope. The radius of the PSF depends on the objectives' numerical aperture (NA) and the excitation light wavelength[41] according to $r = \frac{\lambda_{exc}}{2NA}$. To achieve

sub diffraction resolution, Localization microscopy is implemented by determining the center of the point spread function (PSF) of fluorescent molecules.

2.3 Super resolution microscopy

Fluorescence microscopy is an optical imaging technique commonly used in molecular biology to obtain resolved imaging of bimolecular dynamics. The conventional limitation in the resolution of this technique is set by the diffraction limit of light (~200 nm). The resolution of sub-diffraction-limited features requires the implementation of other microscopy techniques such as multi-photon fluorescence[42], stimulated emission depletion (STED)[43], and saturated structured-illumination microscopy (SSIM)[44]. Even though these techniques have achieved lateral resolution of tens of nanometer, but they also have their own limitations.

Localization microscopy is a high resolution optical technique based on the reconstruction of the image with high accuracy localization of each excited photo-switchable fluorescent molecule. Stochastic optical reconstruction microscopy (STORM) and photoactivated localization microscopy (PALM) are two types of localization microscopy. In both STORM and PALM, a series of images are collected in which an optically resolvable subset of the fluorophores are excited and turned *on*, imaged, then turned *off*. In a subsequent image, a different subset of the fluorophore molecules are excited, imaged, and deactivated. The series of images are the computationally analyzed to locate each fluorophore in each image and a sub-diffraction-limited image can be reconstructed with a resolution of 20 nm[45]. The limitations of this technique relies primarily in the number of photons collected from each excited fluorophore.

STORM and PALM differ in the photochemical mechanisms by which the individual fluorophores are made to blink. In PALM, photoswitching of fluorophores between fluorescent and dark state is controlled, reversible, and may not alter the chemical composition of

molecules[46,47]. It has been reported that commonly used dyes such as rhodamine[48] and cyanine dye, Cy5, can be induced to blink by exposing the dye to light of different wavelengths, mainly photoactivation of molecules is performed utilizing a secondary "photoactivating laser" of a different excitation wavelength. For instance, DiI can be excited and allowed to blink by a laser of λ_{exc} = 561 nm, while another laser of λ_{exc} = 405 nm can be utilized to photoactivate the DiI in the membrane allowing them to photoswitch from the transient dark state back to the fluorescent state. Further, Red Laser light excite Cy5 dye from fluorescent state to a dark state, while green laser converts Cy5 back to the fluorescent state[49,50]. Alternatively for STORM, reversible blinking of fluorescent dyes can be achieved by adding thiols in the imaging buffer that will transition the fluorophores to a stable and reversible *off* state also known as long non-fluorescent state[51,52]. To achieve STORM, fluorophores are surrounded by buffers are consisted of a thiol, glucose, glucose oxidase, and catalase, leading to an increase in the acidity and scavenging the oxygen from the buffer solution[53], influencing the photophysical properties of dyes[54], and increasing the probability of photoswitching back to the fluorescent state from a transient dark state. Glucose oxidase and catalase target and remove oxygen from the buffer, which is the main source of photobleaching. By limiting the oxygen within the buffer, the fluorophore is more likely to undergo a controlled reversible switching between *on* and *off* states. Additional chemicals such as mercaptoethanol and methyl viologen are reducing agents that are added to the buffer although they are highly toxic[55]. Complex STORM buffer with various chemicals induce reversible blinking of dyes, thus enabling STORM imaging.

Localization microscopy depends on the determination of the true fluorophore location relative to the point spread function (PSF). A radiative point source is imaged as an extended blurry point of a finite area in the image plane upon observing it through a diffraction-limited optical

system. A fitting of image of a single fluorophore to a Gaussian function (Eq. 4) enables the determination of the center of the PSF thus localizing the point source[56].

$$G(x,y) = b + h\,exp(-2\,\frac{(x-x_0)^2}{w_x^2} - 2\,\frac{(y-y_0)^2}{w_y^2}) \qquad \text{(Eq.4)}$$

where h is the peak height, b is the background, x_0 and y_0 are the center of the peak, and w_x and w_y are the widths of the PSF in the x and y directions respectively.

The precision of localization (i.e., the error in the PSF center determination) depends on the quality of the image of the PSF, as shown in Eq. 5.

$$< (\Delta x)^2 > = \frac{s^2+\frac{a^2}{12}}{N} + \frac{\sqrt{\pi}*4*s^3*b^2}{a*N^2} \qquad \text{(Eq.5)}$$

Where Δx is the error in localization, s is the standard deviation of the PSF, N is the number of photons collected, a is the pixel size, and b is the background noise. The localization accuracy is inversely proportional to the square root of the number of collected photons in the spot in case of a negligible background noise[56].

Another subtle but equally important factor is the density of photoactivable molecules present in the sample. As stated by Nyquist-Shannon sampling theorem[57], the desired resolution must be around twice the sampling interval, which represents the mean distance between adjacent localized molecules, otherwise the fluorophores will be unresolved.

Localization microscopy surpasses the diffraction limit enabling the detection of previously unresolvable phenomena, however, it is still limited in detecting membrane bending or 3D nanoscale structures. Recent achievements include optimizing the localization microscopy procedure to enable 3D super resolution data acquisition. For a 3D localization microscopy data acquisition, a cylindrical lens is added to the optical setup to additionally enable the axial fluorophores location via astigmatic modification to the PSF[58]. The shape of the PSF reveals

information concerning the particle axial position while minimally compromising the lateral positioning information. The cylindrical lens create a focus offset between x and y direction, reshaping the PSF into an elliptical shape that reveals the lateral and vertical position of the individual fluorophore. A circular PSF is achieved approximately half way between the x and y focal planes. Ellipticity of the image with its major axis is along the x direction, for example, may signify that the fluorophore is above the average focal plane hence the image is more focused in y than in the x direction. Conversely, when the fluorophore is below the focal plane the ellipsoidal major axis may be along the y axis revealing a more focused image in x than in y direction.

A bright nanoparticles sample is usually needed to create a stack of tiff images to record the locations and width of the nanoparticles PSF in x and y direction as the distance from the focal plane is controllably varied. The acquired data is then plotted and saved as a calibration metric for (x,y,z) locations of detected fluorophores. A cross-correlation between the recorded 3D PSF of the gold particles and the PSF of the excited fluorophores in the sample reveal the 3D localization of the molecules. Extensive data analysis is required in 3D STORM including: the creation of a calibration stack from the 3D PSF of the gold beads; detecting the molecular fluorophore in each image and fitting its PSF; localizing the molecule under study by referring to the calibration stack; correcting for stage drift; and reconstructing a super resolution image from the localization data[58].

3D localization microscopy has been performed through a variety of methods such as: the insertion of a cylindrical lens into the emission light path [59]; single-fluorophore interference in a 4π configuration [60], biplane imaging [61], and emission phase manipulations[19]. In these methods, single fluorophore z location is obtained through manipulation of the PSF or the emission path. The vertical location of fluorophores is determined at the expense of the localization precision or modification of the optical system such as including a multi-camera interferometric in the detection

path. The localization precision in z is greater than that of the xy plane ($\sigma_z \sim 2\sigma_{xy}$ *, where* σ_{xy} = 20 nm and σ_z = 40 nm*).* Other advanced implemented techniques overcome the disadvantages of an enlarged multi-lobed single-fluorophore images and reduced positional localization accuracy, and measure the single fluorophore orientation within the membrane. Precise information regarding fluorophore location is obtained by a combination of image defocusing, emission phase modulations, steerable filters, birefringent wedges, and advanced fitting routines [62–71]. However, such techniques include complex optical setups and extensive computational analysis that are particularly challenging when applied to dual multi-color super resolution imaging.

CHAPTER 3 POLARIZED LOCALIZATION MICROSCOPY

3.1 Background

Nanoscale membrane curvature is a critical component in various cellular processes. Fundamental biological questions and disease-related processes are yet to be addressed. A growing interest is emerging in probing the nanoscale organization of biomolecules, dynamics, and the membrane topology simultaneously. Limitations in current imaging techniques inflict a pressing need for a novel optical microscopy technique that enables the understanding of nanoscale membrane behavior, measuring, and controlling nanoscale membrane orientations with 20 nm resolution in living systems.

Nanoscale curvature is essential for many biological functions [72], including the regulation of lipid rafts [2], exocytosis/endocytosis [73], viral fusion/egress [74], nano-therapeutics [75], membrane remodeling [76], and the shedding of circulating microvesicles [77]. Membrane curvature can be induced by the line tension between coexisting liquid lipid phases, the aggregation of curvature preferring molecules, the steric pressure between crowded proteins, and the molecular shape of either lipids or proteins [78–80]. However, quantifying the relative contributions of these curvature-generating mechanisms at physiological length scales remains elusive due to limited experimental capabilities for detecting nanoscale bending.

3.1 PLM advantages

Polarized Localization Microscopy (PLM), overcome the inabilities and limitations of other techniques, require no manipulation of the emission path, minimal alteration to the excitation optics, image samples in aqueous conditions, enable simultaneous dual multi-color imaging of sample, and reveal single fluorophore location and orientation with 20 nm resolution. PLM is

capable of addressing important questions in nanoscale membrane behavior, dynamic curvature generation, and curvature induced variation in biomolecules dynamics.

Basically, PLM combines the advantages of fluorescence localization microscopy (FLM) with polarized TIRFM to reveal single molecule location and orientation. The advanced techniques of localization microscopy such as PALM[39], Fluorescent PALM[36] (FPALM), STORM[20], and direct STORM (dSTORM)[81], and polarized total internal reflection fluorescence (pTIRF) microscopy are progressing the understanding of topics such as lipid phase dynamics, transmembrane signaling, and endocytosis/exocytosis. Yet, individually, these techniques are severely limited. Localization microscopy and diffraction limited pTIRF microscopy separately are not sufficient to resolve and measure membrane orientation below ~200 nm. The combined techniques of localization microscopy and pTIRF microscopy yields an order-of-magnitude improvements in the resolution of membrane curvature. The differential excitation of the membrane-confined probe (such as DiI) by polarized excitation light provides information regarding fluorophore orientation, while fitting each fluorophore PSF provides sub nanometer resolution. PLM is an elegant optical imaging technique that will expand experimental capabilities and provide an insight to fundamental membrane characteristics such as lipid phase, membrane curvature, and lipid packing. PLM has been developed to address and test hypotheses concerning nanoscale membrane curvature and its relation to molecular organization and dynamics. PLM can be performed on a conventional TIRF microscope by adding a single optical component that controls the polarization of the excitation light.

3.3 Theory of PLM

PLM is sensitive to various membrane orientations, in particular, PLM depends on the relative orientation between the membrane probe (DiI) and the direction of polarized excitation

light. The coordinate system is set such that the glass-water interface is the xy-plane, and the optical axis of the microscope represents the z axis. The evanescent wave propagates along the xy plane with an exponential decaying z component. The local membrane orientation is represented by the polar angle (Θ), which represents the tilt angle between the membrane and the z-axis, and the azimuthal angle (φ), which represent the rotation angle of the membrane within the xy-plane. As the membrane is represented by its normal vector $\boldsymbol{n}$, then Θ is the angle between $\boldsymbol{n}$ and z-axis, while φ is the angle between the projection of $\boldsymbol{n}$ onto the xy-plane and the x-axis. The incorporated DiI molecules in the membrane also experience an additional tilt, undergo azimuthal rotation, and considered to be distributed with azimuthal symmetry. The orientation of DiI within the membrane is defined by two components relative to the membrane normal, the polar tilt (β) and the azimuthal rotation angle (ψ) (Fig. 3).

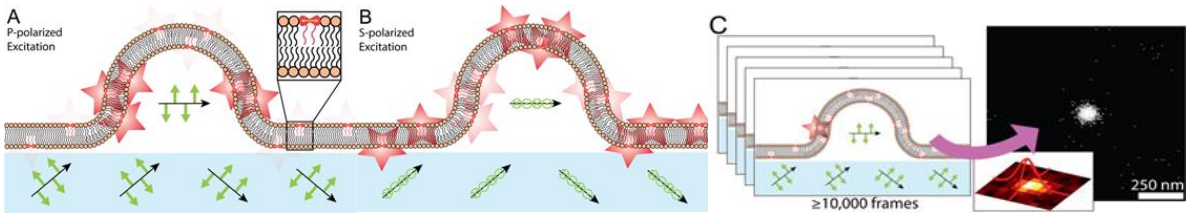

Figure 3. PLM combines the techniques of polarized TIRFM and SMLM. By controlling the linear polarization of incident excitation light, the electric field (green arrows) of the evanescent wave for fluorescence excitation can be either (A) vertical with p-polarized light or (B) horizontal with s-polarized light. This results in differential fluorophore excitation depending on membrane orientation. (C) Imaging and localizing individual blinking fluorophores in separate frames enable the reconstruction of super-resolution images with embedded information on membrane orientations.

If $\beta = 0$ then DiI would be parallel to the membrane. Therefore, the Cartesian components of the fluorescent label dipole moment $\boldsymbol{\mu}$ are given by [82]:

$$\mu_x = \cos\theta\cos\phi\sin\beta\cos\psi - \sin\phi\sin\beta\sin\psi + \sin\theta\cos\phi\cos\beta,$$

$$\mu_y = \cos\theta\sin\phi\sin\beta\cos\psi + \cos\phi\sin\beta\sin\psi + \sin\theta\sin\phi\cos\beta,$$

$$\mu_z = \cos\theta\cos\beta - \sin\theta\sin\beta\cos\psi \qquad \text{(Eq. 6)}$$

The probability of exciting a fluorophore with a certain orientation is proportional to the average over ψ of the square of the dipole component along the polarized excitation light. For instance, that number in s-polarization in proportional to $< {\mu_x}^2 >$. Averaging over ψ and the squaring step reveal the strong dependence of s-polarization on θ and ϕ, whereas p-polarization is only dependent on θ regardless of the membrane ϕ. This is clearly manifested theoretically in figure 4 and experimentally when imaging spherical structures such as GUVs (fig. 5). Given the probability of exciting a single fluorophore of a certain orientation with s-pol (xy-plane) or p-pol (z-axis) polarization, the emission is also defined into two components in the corresponding planes.

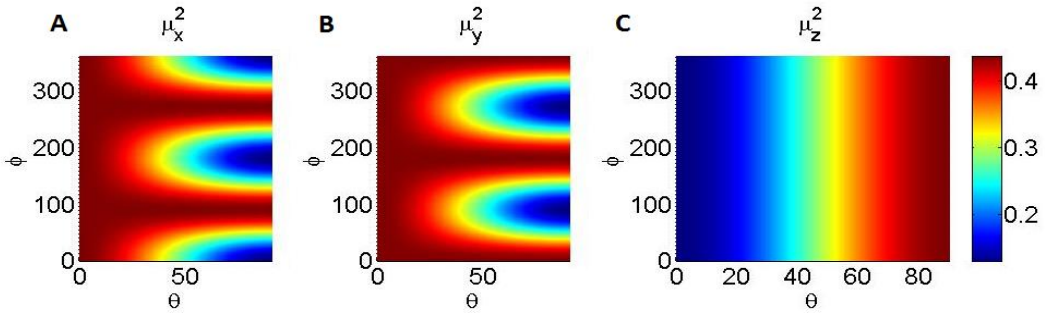

Figure 4. Probability of exciting a single fluorophore with a certain orientation. The probability of is proportional to the plotted dipole moment components squared estimated theoretically.

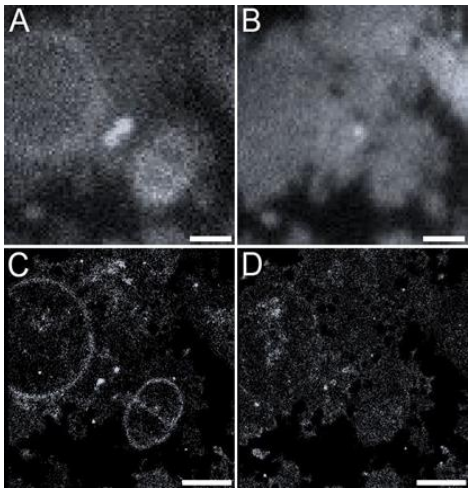

Figure 5. S-polarization exhibit a phi-dependence of the excited fluorophores. Polarized Localization Microscopy detects the vertical edge of a GUVs adhered to an SLB, as shown schematically in Fig. 5B. (A) Diffraction-limited pTIRFM image of the supported lipid bilayer and the GUVs shows increase in brightness corresponding to the vertical edge of the GUV. Black region is glass surrounding the labeled lipid membrane. (B) The uniform fluorescence in the

diffraction-limited sTIRFM image indicates the presence of membrane without specificity to membranes of varying orientation. (C) Histograms of localizations from pPLM demonstrate the increased density of localizations from vertical membranes. The vertical membrane perpendicular to the glass is clearly observed within the super resolution image, in addition to the membrane between the two adjacent GUVs. (D) Histograms of localization in sPLM demonstrate a more uniform distribution of localizations. Scale bars represent 1μm.

The collection efficiency by the microscope objective of the emitted light is proportional to the square of each emission component, this have been reported to be proportional to $(\cos\theta)^2$ and $(\sin\theta)^2$ for p-pol and s-pol excitation polarization. An effective collection bias of the objective for emission light from a dipole oriented parallel or perpendicular to the coverslip is dependent on the NA of a certain objective and on the dipole relative distance to the coverslip. This bias is prominent for low NA TIRF objectives (e.g. NA = 1) and larger distances from the coverslip (z >100nm). In the current PLM setup, the NA of the TIRF objective utilized is equal to 1.49 with images samples of few nanometer thickness and z_{max} ~ 120 nm. Therefore, the effective collection efficiency of both polarization emission are consistent and fall within 10% variation for all given fluorophore orientation. The high numerical objective and the small separation distance between the fluorophores and the coverslip result in minor collection bias, the collection efficiencies will be set to unity in the probability estimation of detecting a single fluorophore with a certain orientation.

The dipole tilt β is set to be 69° to match experimental results of DiI in planar membranes in HEK cells performed previously[32]. Applied variation in β by 5° has a less than 5% effect on the theoretical results [83]. Further, the dipole moment experience rotational motion around $\boldsymbol{n}$. The azimuthal rotation of the dipole passes through a series of azimuthal angles ψ from the instance the azimuthal location upon excitation to the azimuthal location upon emission. This time interval was shown to be ~ 0.2 ns[82]. Within the camera exposure time of 18 ms, hundreds of excitation events occur, where the rotational diffusion of the dipole results in an averaging over all their ψs.

For PLM experimental setup, the p-polarized excitation light possess an evanescent electric field ($\boldsymbol{E_p}$) which is elliptically polarized in the xz-plane with mainly a z-component and a slight polarization in the x-direction. The z- and x- components are out of phase by π/2. The s-polarized light exhibits an evanescent electric field ($\boldsymbol{E_s}$) which is linearly polarized in the y-direction with a simply y-component. The corresponding components of the evanescent wave electric field is calculated according to[84]:

$$E_x = \left[\frac{2\cos\Theta_i \sqrt{(sin\Theta_i)^2 - (n)^2}}{\sqrt{(n^2 cos\Theta_i)^2 + (sin\Theta_i)^2 - (n)^2}}\right] A_p$$

$$E_z = \left[\frac{2\cos\Theta_i \ \sin\Theta_i}{\sqrt{(n^2 cos\Theta_i)^2 + (sin\Theta_i)^2 - (n)^2}}\right] A_p$$

$$E_y = \left[\frac{2\, cos\Theta_i}{\sqrt{1-(n)^2}}\right] A_s\,, \qquad \text{(Eq. 7)}$$

where n = n_g/n_s, Θ_i represent the excitation incident angle, and A_p and A_s represent the amplitude of incident electric field in p-pol and s-pol, respectively. Taking into consideration the utilized excitation light wavelength (λ_{ex} = 561 nm) and the indices of refraction of the sample and glass (1.33 and 1.52, respectively), the electric field components were evaluated as[82]:

$$\boldsymbol{E}_p = E_p^0\,(0.5\boldsymbol{x} + 1.9i\boldsymbol{z}).\exp\left(\frac{-z}{2d}\right),$$

$$\boldsymbol{E}_s = E_s^0\,(1.7\boldsymbol{y}).\exp\left(\frac{-z}{2d}\right), \qquad \text{(Eq. 8)}$$

where *d* is the evanescent wave characteristic penetration depth and E_p^o and E_s^o are the magnitudes of the p- and s-polarized incident electric field, respectively. For simplicity, E_p was approximated to be linearly polarized in z. The elimination of the x-component induces a 7% error in the intensity measurement for excited DiI molecules. The detected intensity by pTIRM for an excited single

fluorophore in p-pol and s-pol excitations are proportional to the fluorophore dipole moment multiplied by the electric field squared as $I_p = \left(\mu_z \cdot \boldsymbol{E}_p\right)^2$ and $I_s = \left(\mu_y \cdot \boldsymbol{E}_s\right)^2$.

The localization portion of PLM depends on the probability of exciting a single fluorophore and detecting it. This probability incorporates the intensity of an excited DiI molecule by either light polarization. The brightness distribution of localized individual fluorophores exhibit an exponential behavior with average fluorophore brightness proportional to the intensity of fluorophores. A brightness threshold (B_o) is generally set to allow only the detection of fluorophores that are brighter than B_o and discard dim fluorophores. This procedure enhances the signal to noise ratio of reported data, increases the localization precision which is dependent on the brightness of detected fluorophores, increases PLM sensitivity to membrane orientation, and in case of high B_o value specific information regarding θ can be extracted. The value of B_o was set theoretically to match the experimental cut-off values used.

Thereby, the probability of detecting a DiI molecule with a certain membrane orientation (θ, φ), DiI orientation (β, ψ), distance from the focal plane (z), and averaged over all ψ within a single-frame exposure time for p-polarized and s-polarized excitation is approximated as:

$$\boldsymbol{P}_p = \exp\left(\frac{-B_0}{3.6 < \mu_z^2 > \exp(-\frac{z}{d})}\right),$$
$$\boldsymbol{P}_s = \exp\left(\frac{-B_0}{2.9 < \mu_y^2 > \exp(-\frac{z}{d})}\right), \qquad \text{(Eq. 9)}$$

As the fluorophore exists in distances farther away from the objective focal plane, the single fluorophore will exhibit a wider PSF as it become out of focus. Typically, the detection probability depends on the distance of single fluorophores from the focal plane. In the current PLM setup, the objective focal plane is ~ 200nm which is much larger than the membrane heights within

the presented study. Thus no change in the probability of detecting a single fluorophore as function of its distance from the focal plane was included in this analysis. Membrane curvature detection depends on both excitation polarization in PLM, where p-polarized excitation localization microscopy (pPLM) reveal membrane tilt (θ), and s-polarized excitation localization microscopy (sPLM) reveal information regarding θ and ϕ.

3.4 Modeled membrane topography and diffusion

In order to demonstrate the powerful capabilities of PLM and its increased sensitivity over current imaging methodology in detecting and resolving nanoscale membrane curvature, simulations of various membrane topographies with the corresponding detection probabilities were performed. The membrane topography was simulated by smoothly connecting the spherical NP coating to a planar sheet with no less than 20 nm radii of curvature. With custom MATLAB routines, a random distribution of points on these simulated topographies mimicked the possible 3D locations of localized fluorescent lipids. These points were used to reconstruct simulated PLM images and lipid trajectories by incorporating the localization probabilities and localizations impressions and inaccuracies.

The membrane topography was simulated starting with creating a random distribution of points over the simulated membrane topography (Fig. 6C) with an average density of 1 point/nm^2. A simulated single lipid was allowed to randomly step between points. Single simulations steps were equivalent to 3.1 μs and 2.6 nm and the simulated lipid positions that were separated by 6400 simulation steps were compared to mimic a 50 Hz camera frame rate to match the experimental data. Whereas the experimental data incorporated camera blur and t_{exp} of 0.018 s, simulated positions had an equivalent t_{exp} = 0 and no camera blur. 7,800 steps were simulated and considered in the diffusion analysis over the curved membrane.

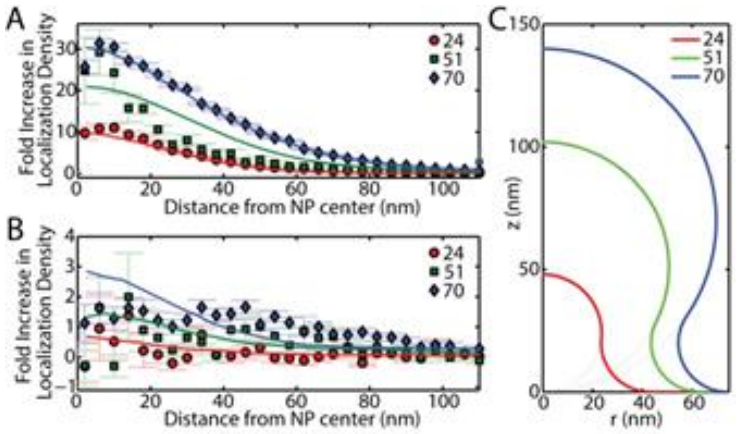

Figure 6. Radial density line scans for localizations from membrane topography.Radial density line scans for localizations from membrane topography observed in (C) over rNP = 24, 51, and 70 nm via (A) pPLM and (B) sPLM. Data points show the experimental results while the simulation results are plotted as solid lines. A single B0 value and out-of-focus magnitude for anisotropic inaccuracy were fit all six data sets.

For a typical electron multiplying device, the sensor area gets exposed to the emitted light captured by the objective. The captured image, depicted as incident photons on the camera sensor, is then multiplied, for signal amplification before it's transferred to storage. The storage area is usually made up of aluminum, and acts as a shutter between capturing the image and storing it. The charge multiplication process and the electronic shutter occur in MHz rate to ensure high speed readout mode. The readout time typically is set by the user as exposure time, but the frame transfer requires an additional couple ms to transfer the image to storage. Upon setting the camera exposure time, one have to keep in mind the "dead time", which is the time required for amplifying the signal and transferring it for storage, which also contributes to the final reported camera frame rate (~50Hz). The fraction of the exposure time (t_{exp}) to the time between frames (Δt) is critical for the diffusion analysis.

To mimic the local change in membrane viscosity due to curvature exhibited as an apparent slowing in the lipid diffusion, the effective time per simulation step was modified. Single simulations steps on the flat membrane were kept equivalent to 3.1 μs and 2.6 nm, while these

values changed to (3.1* D_{ratio}) μs for each 2.6 nm when the simulated lipid was on the curved membrane. This enabled simulation the slowing of lipids by D_{ratio} on the curved membrane compared to the flat bilayer. In the absence of simulated error, the step lengths (v) were calculated as

$$v(t_S) = \sqrt{(x(t_s) - x(t_s + 6400))^2 + (y(t_s) - y(t_s + 6400))^2}, \qquad \text{(Eq. 10)}$$

and the distribution of $v(t_S)$ was used to fit Eq. 16.

3.5 Comparison between SMLM methods

Comparison between pPLM, sPLM, TIRFM, epifluorescence microscopy, and 3D TIRF localization microscopy were performed on a budding event of 50 nm radius surrounded by a planar bilayer. The number of localizations obtained at the site of budding is expected to increase regardless of the imaging technique simulated. This is due to the local increase in membrane area per pixel proportional to ($1/\cos\theta$). Illumination modes were compared based on the expected number of localizations detected for the vesicle budding event. The number of localizations obtained in p-polarization excitation is expected to show a higher increase, from flat bilayer, than other excitation modes since the bud membrane have larger θ which p-polarization is specifically sensitive to.

Detected number of localization estimation was performed based on the probabilities P_s and P_p of detecting a fluorophore in sPLM and pPLM, respectively. On the other hand, the detection probability for an unpolarized TIRFM illumination does not depend on membrane orientation. In concept, unpolarized TIRFM is a combination of all polarizations with equal probability of exciting all fluorophores independent of their orientation though it is dependent on the fluorophore distance from the coverslip (z). For an unpolarized TIRF illumination, it is not required to include a polarization sensitive dye in the membrane such as DiI. Other membrane

probes can be incorporated, such as DPPE-Rhodamine, which binds to the membrane by a long flexible linker allowing the fluorescent part of the dye to have random orientations. Thus the probability of detecting a fluorophore in unpolarized TIRF was estimated as:

$$P_{uTIR} = \exp\left(\frac{-B_0}{1.7\exp(-\frac{z}{d})}\right), \qquad \text{(Eq. 11)}$$

As for epifluorescence illumination, the probability of localizing a fluorophore depends only on the intensity of the illumination light and the detection threshold, which are assumed to be the same for all other illumination modes. Therefore, P_{epi} is set to be a constant in the simulations.

In a TIRF setup with a fixed angle of approach to the coverslip, as used in the following experiments, the evanescent wave is traveling in the x-direction and the light may be polarized in the y- or z-directions. If the TIRF illumination were spun in a circle around the back aperture of the objective, then the evanescent wave would travel in x and y directions allowing all polarizations to be accessible. However, since the fluorophore is presumed to be tumbling randomly for these unpolarized analyses, the increased number of accessible polarizations has no effect on the results. The key components that affect the probability of localizing a randomly tumbling fluorophore is the illumination intensity and the localization threshold (B_0). Thus in the cases of unpolarized TIRF and unpolarized epifluorescence illumination, there is assumed to be no dependency on the light polarization, as if the fluorophore is randomly tumbling while attached by a long, flexible linker. This would be analogous to using DPPE-Rhodamine rather than DiI; we see no polarization or membrane-orientation dependence in the density of localizations from DPPE-Rhodamine.

3.6 Membrane bud identification

The presence of the simulated membrane bud affects the local localization density, as the bud increases in size, the area of membrane per pixel is expected to increase, resulting in a significant increase of expected detected localizations. The expected localizations from a planar

membrane obey a Poisson distribution. Quantitatively, the presence of a membrane bud is detected with statistical significance of a p-value (p) when the number of localizations at the bud region (N_{bud}) is greater than the mean number of localizations from the planar membrane (N_{plane}) according to

$$p = e^{-N_{plane}} \sum_{i=N_{bud}}^{\infty} \frac{\left(N_{plane}\right)^i}{i!}. \quad \text{(Eq. 12)}$$

The value of N_{bud} that satisfies Eq 12 (N_{bud}^0) mainly depends on the fluorophore incorporated within the membrane. The number of detected localizations at the membrane bud depends on the sensitivity of the fluorophore to the illumination excitation light. For polarized TIRF, DiI is incorporated into the membrane and reveal up to a 20x more localizations on the bud than on the flat planar membrane.

Direct determination of the z location of a single fluorophore within the membrane is possible with 3D localization microscopy. However, that comes on the expense of an increased localization uncertainty in z, where the uncertainty in z is double that in the x and y ($\sigma_z \approx 2\ \sigma_x \approx 2\ \sigma_y \approx 40$ nm). Obtaining information in the third dimension enables detecting change in membrane topology by monitoring the change in the z location of fluorophores instead of membrane orientation. As it might seem appealing to use direct fluorophore location to determine membrane bending regions, but there are some limitations to this technique. The present uncertainty in the fluorophore height requires the averaging of multiple fluorophores to obtain a better measurement of average membrane height within a given area. Due to this uncertainty, 3D localization microscopy requires the acquisition of a higher number of localizations than pPLM to detect membrane curvature. Statistically significant determination of bud presence in 3D localization microscopy incorporated the average z location of the localizations at the membrane bud along

with the associated uncertainty in z. Bud detection dictates that the standard error of the mean of the average z location of fluorophores to be small such that the bud is clearly distinguished from the planar membrane according to

$$p = 0.5\, erfc\left(\langle z_{bud} \rangle \frac{\sqrt{N_{bud}^{0}}}{\sigma_z \cdot \sqrt{2}} \right), \quad \text{(Eq. 13)}$$

where erfc represents the complementary error function. A planar membrane was simulated with generation of a membrane bud of 50 nm radius was simulated. The various stages of the budding event initiating from a planar membrane to a detached vesicle mimics the stages of endocytosis. The expected increase in the number of localizations due to the presence of the membrane bud was evaluated and plotted for all illumination modes under study. Further, comparison between N_{bud}^{0} with a p value of 0.0001 was plotted for the different budding stages and imaging techniques. These plots demonstrate the sensitivity of each single technique in detecting nanoscale membrane deformation, and determine their increased sensitivity over other techniques.

3.7 PLM sensitivity

During the budding event, when the top of the membrane bud was 40 nm above the surrounding bilayer, the number of localizations at the location of the bud was 9x greater than that of the planar bilayer when imaged by pPLM. While epifluorescence, TIRFM, and sPLM had only double the localizations of that of a flat bilayer. The 4-fold increase in the ratio of localizations of bud to plane in pPLM versus other techniques reveal the pPLM increased sensitivity to detecting nanoscale membrane buds. Further, when the top of the bud was 120 nm away from the bilayer, with a detached vesicle configuration, pPLM is expected to exhibit a 22x increase in the

localizations on the bud versus the planar bilayer. Similarly, only 5x, 4x, and 3x more localizations are expected from epifluorescence, TIRFM, and sPLM respectively (Fig 7).

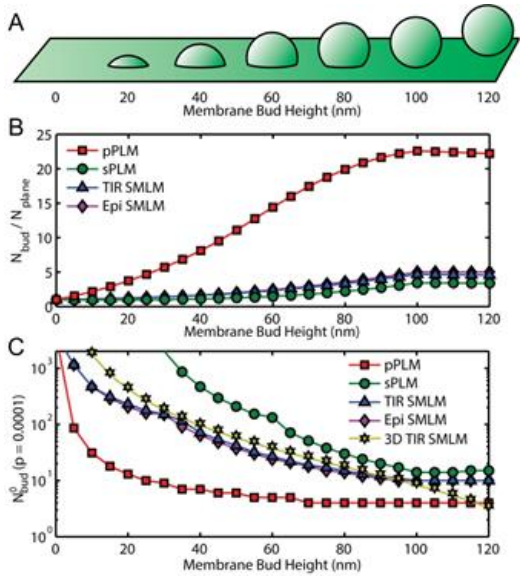

Figure 7. Sensitivity of PLM compared to other optical methods. Estimation for observed localizations of a budding membrane reveals the sensitivity of PLM compared to other optical methods. (A) Membranes containing buds of 50 nm radii of curvature were analyzed at varying protrusion distances from the surrounding connected planar membrane. The fractional increase in localizations due to the bud are plotted. (B) The increased number of localizations expected due to non-planar membrane shape relative to the number of localizations expected from a planar membrane demonstrated a 22.5x increase in localization density with pPLM, which is over 4x larger than expected for sPLM, unpolarized epifluorescence SMLM, and unpolarized total internal reflection (TIR) illumination SMLM. (C) The required number of localizations to identify a membrane bud from the surrounding SLB ( ) with p = 0.0001 are plotted for pPLM, sPLM, unpolarized TIR, unpolarized epifluorescence SMLM, and 3D SMLM.

Further, pPLM requires less number of localizations for the detection of membrane curvature over epifluorescence, TIRFM, sPLM, and 3D localization microscopy for all bud heights less than 110 nm. In particular, for p = 0.0001, pPLM requires 10% of the total number of localizations required for 3D localization microscopy at bud height of 40 nm. This means that pPLM is capable of detecting nanoscale membrane bending earlier than 3D localization microscopy and with less total number of localizations. Keeping in mind that 3D localization microscopy requires averaging of fluorophore locations with incorporated localization uncertainty

while pPLM depends directly on the collected localization density within a given area for identification of local membrane bending sites. In this simulation, pPLM proves to be a more sensitive technique with faster curvature identification than epifluorescence, TIRFM, and sPLM. For instance, pPLM requires 11%, 10.5%, and 2% of the total localizations expected for TIRFM, epifluorescence, and sPLM respectively. Experimental comparison between pPLM and sPLM are discussed later.

sPLM represent an internal control for the possible membrane structures. Direct comparison between localization densities obtained in sPLM and pPLM reveal information regarding membrane orientation. sPLM represent areas of flat membrane with direct control to its quality. For certain membrane structures, pPLM is expected to convey a higher localization density while sPLM convey a nearly uniform distribution with minor fluctuations. This is especially the case of a membrane hemisphere, while a membrane vesicle bound to the top of a planar bilayer is expected to induce an increase in local localizations in both PLM polarizations due to the present membrane orientations and the presence of more membrane per pixel.

3.8 MATERIALS AND METHODS

Sample dish preparation

Glass bottom dishes (MatTek Corp.) were cleaned by immersion in 7x detergent overnight, rinsed with diH2O (18.2 MΩ-cm, EMD Millipor Corp.), bath sonicated for 30 min, dried with nitrogen gas, and cleaned by air plasma (Harrick Plasma Inc.). NPs were diluted in diH_2O, sonicated for 15 min, and deposited on a glass coverslip. NP sedimentation occurred for 10 min to achieve a density of 0.02 NPs/μm^2. Separate polystyrene NPs were used for both engineering membrane curvature and tracking stage drift. The index of refraction of polystyrene is 1.59. NPs for creating membrane curvature were either 26 nm radius, λ_{ex} = 647 nm (FluoSpheres, Life

Technologies); 51 nm radius, λ_{ex} = 405 nm (FluoSpheres, Life Technologies); or 70 nm radius, λ_{ex} =488 nm (Fluoro-Max, Fisher Scientific). NPs for detecting stage drift (100 nm diameter, Tetraspecs, Life Technologies) were fluorescent in all color channels. Dishes were placed on a 55 °C hot plate for 5 min to ensure their stability on the coverslip. NP shape after exposure to the hotplate was confirmed by scanning electron microscopy (Fig. 8).

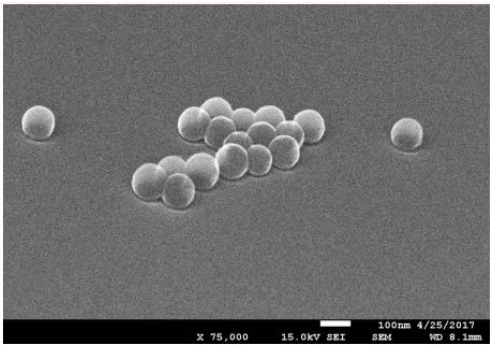

Figure 8. SEM images of NPs. To confirm the fidelity of the nanoparticles shape, structure, and size after exposure to the hotplate, scanning electron microscope (SEM) images were then acquired using a field emission scanning electron microscopy (JSM-7600F from Jeol USA, Inc.) in the Wayne State University Electron Microscopy Laboratory. These 51 nm diameter polystyrene nanoparticles were carbon coated and imaged at an angle of 55° with a secondary electron detector to reveal the heights of the nanoparticles from the coverslip.

Supported lipid bilayer formation

Giant unilamellar vesicles (GUVs) of primarily 1-palmitoyl-2-oleoyl-sn-glycero-3-phosphocholine (POPC, Avanti Polar Lipids, Inc.) labeled with 0.3 mol% 1,1'-didodecyl-3,3,3',3'-tetramethylindocarbocyanine perchlorate (DiI, Life Technologies) were prepared by electro-formation, as described previously [85]. This fluorophore density yielded 110 nm^2 of bilayer per DiI molecule. In brief, GUVs were formed by mixing lipids in chloroform and spreading them uniformly on a conducting indium tin oxide (ITO)-coated slide (Sigma-Aldrich) via spin coating. The resulting lipid film was dried under vacuum for >20 min. A second ITO-coated slide and silicon spacer enclosed the dried lipids into an incubation chamber. A hydration buffer of 200 mM sucrose was added to the dried lipid films and the ITO slides were connected to a sine wave

function generator. The growth of the GUVs occurred over 3 hours at 55 °C with alternating voltage of 10 Hz and 2 V_{rms}. GUVs were stored at 55 °C and discarded after 3 days. GUVs were created varying in diameter from <200 nm through 100 μm.

The GUVs were placed up the glass bottom dishes and the NPs for up to 1 hour at room temperature. The interaction between the GUVs with the plasma cleaned glass coverslip resulted in bursting of the GUVs and the formation of patches of SLB over the glass and NPs. This method of SLB creation proved to create more uniform SLBs over the NPs than SLBs formed by the fusion of large unilamellar vesicles (LUVs).

Large unilamellar vesicles (LUVs) preparation

POPC, DiI and occasionally DPPE-Biotin in chloroform were mixing in a glass vial. DiI was added to 0.3 mol% of all lipids, DPPE-Biotin was occasionally added to 1 mol% of all lipids, and POPC was the remaining >98.7 mol%. The mixture was dried under nitrogen gas and placed under vacuum >20 min. The lipid films were hydrated in 1X phosphate buffer saline (PBS) buffer of pH =7 to a concentration of 1g/L. The sample was vortexed, pre-extruded once through a polycarbonate membrane filter of 400 nm pore size, and extruded 20 times through a membrane filter of 100 nm pore size. 5 μL of 10 mM CaCl2 and 120 μL of 1 g/L LUVs were added to a cleaned MatTek dish and incubated for 30 min. Excess LUVs were washed away with PBS buffer. When DPPE-Biotin was included, 20 μL of 50 μg/mL of streptavidin solution was added to immobilize the remaining unfused LUVs to the underlying SLB.

Optical setup

PLM was performed with an inverted IX83 microscope with Zero-Drift Correction and a 100x, 1.49NA objective (Olympus Corp.) on a vibration-isolated optical table. Four continuous wave diode lasers were incorporated at wavelengths 405, 488, 561, and 647 nm, each with at least

120 mW max power for fluorescence excitation, with the appropriate beam expanders to control the size of the laser spot. The laser beams are then directed to dichroic mirrors that will combine the different wavelength laser beams into a single beam. The lasers then pass through a linear polarizer and liquid crystal wave plate.

The excitation polarization was rotated with computer-controlled liquid crystal wave plate (Thorlabs Inc, LCC1111-A). The intensity of the p- and s-polarized light were separately measured versus applied voltage to the liquid crystal wave plate (LCWP). The 561 nm laser was passed through the liquid crystal wave plate and through the TIRF microscope objective with an existing angle of 65°, as would be the case for PLM. After the objective, the laser passed through a linear polarizer (LPVISE100-A, Extinction ratio: 18000:1, Thorlabs, Inc.) in either a vertical or horizontal orientation prior to being incident on a power meter (PM100D, Thorlabs, Inc.). After transmitting through the LCWP, the microscope objective, and the linear polarizer, the laser power was measured while sweeping through voltages to the LCWP with a custom-made LabVIEW program. The power ratios of the P/S and S/P are plotted in Fig. 9 . At the optimal voltages of 1.924 and 1.245 V, the power ratio of P/S and S/P are 207:1 and 54:1, respectively. These ratios were approximated as infinite for the theoretical analysis.

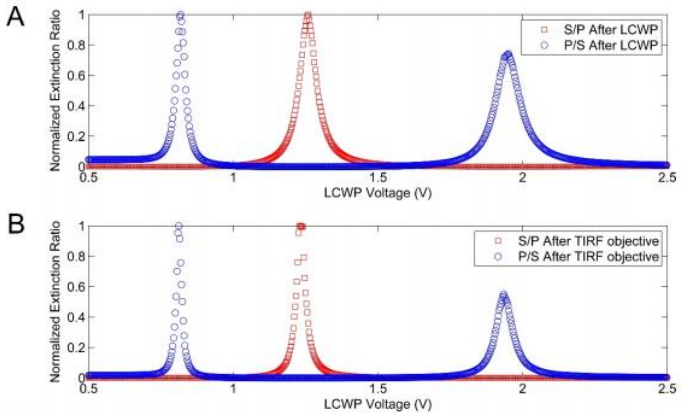

Figure 9. Uncompromised polarization of light after passing through the LC. The extinction ratio of p-polarized and s-polarized excitation light after passing

through the liquid crystal and the TIRF objective demonstrates the uncompromised polarization of light after passing through the two optical components. The chosen voltages to perform PLM for the two polarizations show the high extinction ratio for P/S and S/P for p-polarized and s-polarized light, respectively. The ratio of output powers at a range of voltages after passing through (A) the liquid crystal wave plate, and (B) the TIRF objective are plotted. The ratios of the eventual p-polarization to s-polarization after passing through the liquid crystal are: P/S = 68:1 and S/P = 135:1. The ratios of the p-polarization to s-polarization after passing through the TIRF objective are: P/S = 207:1 and S/P = 54:1 when the appropriate voltages were applied to the liquid crystal.

The beam direction is steered by a rotating dichroic mirror onto a quad-band mirror (ZT405/488/561/647rpc, Chroma Technology Corp.) designed to reflect the laser wavelengths of 405, 488, 561, and 647 nm while reflecting the intermediate fluorophore emission wavelengths, before reaching the back of the objective (100x, 1.49 NA, Olympus Corp.) and ultimately exciting the fluorophores in the sample. This mirror provide control over incident excitation angle, which enables the switching between TIRF and epifluorescence excitation. The different emission wavelengths are individually selected with a filter wheel (LB10-W32-Y73, Sutter Instrument Co.) capable of 40 ms changes between filters specific for the emission ranges between the lasers wavelengths. Image acquisition was performed with an iXon-897 Ultra EMCCD camera (Andor Technology) proceeded by emission filters (BrightLine single-band bandpass filters, Semrock, Inc.), a 4-band notch filter (ZET405/488/561/640m, Chroma Corp.), and a 2.5x magnification lens (Olympus Corp). This setup provided high laser power (>80 mW) at each polarization and integrated computer control of all equipment via custom LabVIEW routines (National Instruments Corp.).

Data Acquisition

A key event in collecting raw data for post-acquisition analysis is the synchronization of all pieces of hardware within a single graphical user interface computer controlled program. A graphical software based on LabVIEW was developed (fig. 10) . This LabVIEW program synchronizes electronic hardware used for pTIRF localization microscopy, acquires data from the

EMCCD, and saves it for later processing. It connects the inputs and outputs of 10 different pieces of computer-controlled equipment: (1) four Coherent lasers with wavelengths of 405 nm, 488 nm, 561 nm, and 647 nm; (2) three shutters that open and close allowing the passage of the laser beam with 8 ms open/close durations; (3) neutral density (ND) filter wheels for laser light attenuation; (4) a high-speed emission filter wheel; (5) liquid crystal wave plate for the polarization of light and (6) and the electron multiplying charge coupled device camera for single-fluorophore observations. This program achieved optimum performance of the hardware, including the optimization of the camera acquisition parameters and macros for commonly performed experimental protocols. Help features, instructions within the software, a feedback note that constantly updates and display the status, and an error indicator to prevent new users from damaging sensitive equipment are also a part of this program.

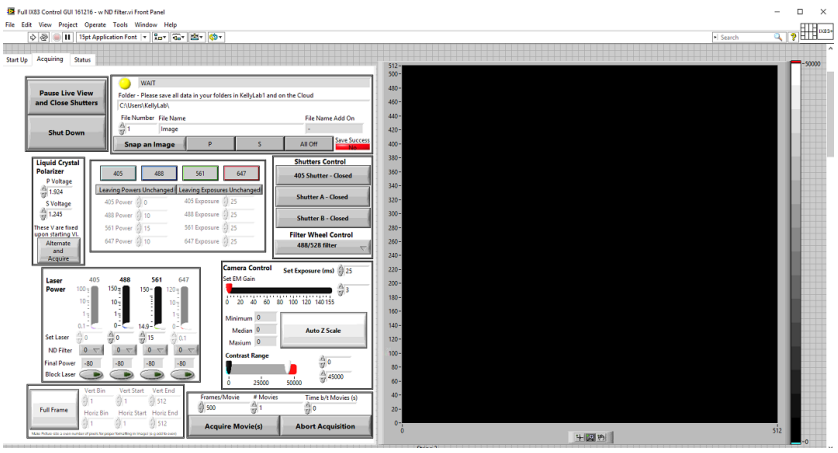

Figure 10. LabView program that controls hardware and enables data acquisition.

Imaging buffer

PLM was performed on samples present in an oxygen-scavenging buffer (150 mM NaCl, 50 mM TRIS, 0.5 mg/mL glucose oxidase, 20 mg/mL glucose, and 40 µg/mL catalase at pH 8). Buffer proteins were purchased from Sigma-Aldrich and salts were purchased from Fisher Scientific. These conditions maintain a low free oxygen concentration in the buffer to minimize

non-reversible fluorophore bleaching and encourage transient fluorophore blinking, as is necessary for SMLM.

Imaging procedure

Exposure of the sample to >80 mW of excitation light with λ_{ex} = 561 nm for 3 s resulted in converting most of the DiI from the fluorescent state '*on'* to the transient non-fluorescent, dark state *'off'* to provide steady state fluorophore blinking. The '*on'* fluorophores were imaged at a density of <1 fluorophore/μm^2. Sequential movies were acquired with alternating p-polarized TIRF (pTIRF) excitation at λ_{ex} = 561 nm for pPLM and s-polarized TIRF (sTIRF) excitation at λ_{ex} = 561 nm for sPLM. Between 10,000 and 30,000 frames were acquired for each polarization at a frame rate of 50 Hz on a region of interest with 18 ms acquisition per frame.

Single-fluorophore localizations

The analysis of the raw, diffraction-limited images included low-pass Gaussian filtering, median background subtraction, lateral stage drift correction, and the fitting of each isolated fluorophore images via the ImageJ plug-in ThunderSTORM [86]. ThunderSTORM provided the single fluorophore positions, localization uncertainty, and photon per fluorophores for further analysis. A threshold value 100 photons per fluorophores was used to keep only the bright localizations for further analysis. Single-molecule DiI localizations had 13 ± 5 nm precision (Fig 11). The localizations from s- and pTIRF excitation were analyzed separately to reconstruct separate super-resolution images for polarization.

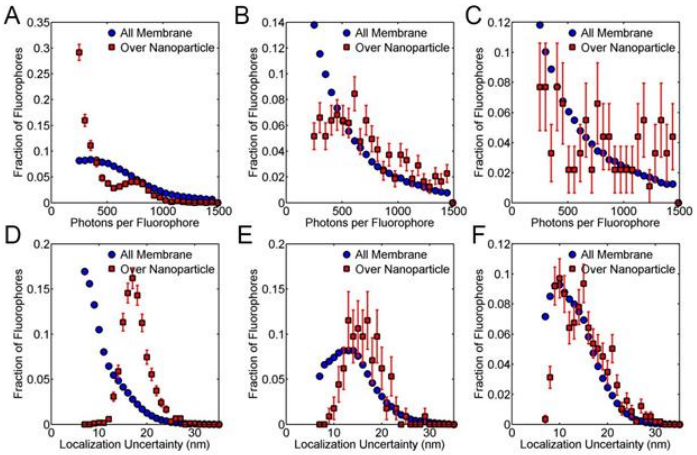

Figure 11. Histogram plots of brightness and uncertainty of localizations in PLM. The distribution of the number of photons per fluorophore obtained from pPLM data of the whole membrane in comparison to the detections from the curvature region and the corresponding localization uncertainty for membrane over 24 (A,D), 51 (B,E), and 70 (C,F) nm radius nanoparticles.

Single-particle tracking (SPT)

Single particle tracking is a technique that utilized the tracking fluorescent molecules over sequential frames and identifying their trajectory to reveal their dynamics. This technique is commonly employed to investigate the diffusion rates of molecules in various environments. Standard SPT procedure requires the localization of fluorescent molecules in each frame (up to 25 nm accuracy)[87], then processing the locations in a tracking program (written In MatLab). When the center of the Gaussian functions are present within a user-defined distance for consecutive frames, the centers are identified to belong to the same trajectory for a single fluorophore. For diffusing molecules, a cutoff is chosen for a given time lag based on the probability that a molecule with diffusion coefficient D has diffused a distance L in a time Δt set by the user.

$$P = 1 - e^{\frac{-L^2}{4D\Delta t}} \qquad \text{(Eq. 14)}$$

Trajectories are analyzed to obtain the diffusion coefficients by calculating the mean squared displacements (MSD) for all trajectories for different step sizes, and then performing a

linear fit of the MSD graph as function of time. The resulting MSD vs Δt curve for Brownian diffusion should follow

$$<r^2> = 4D\Delta t \qquad \text{(Eq. 15)}$$

Where r is the step sizes, D is the diffusion coefficient, and Δt is the time step. High-throughput single particle tracking[88] enables the observation of the distribution of single particle trajectories, and correlate the molecular diffusion rates with membrane properties such as membrane phase, curvature, and electrostatics within a noisy background.

The sequential localizations of single fluorophores were analyzed to reveal the diffusion rate of individual molecules versus membrane topography. The individual fluorophore trajectories projected onto the imaging plane were identified with custom MATLAB code. Single-fluorophore localizations were linked as a trajectory if they were in sequential frames, within 500 nm of each other, and there was no alternative localization for linking within 1 μm. The single-molecule step lengths (v) were grouped based on their distance from the NP center, and their normalized distribution was fit to a 2D Maxwell-Boltzmann distribution (Eq. 16) as would be expected for 2D Brownian diffusion, to find the fit diffusion coefficient (D_{fit}).

$$P(v) = \frac{v}{2D_{fit}\Delta t} e^{-\frac{v^2}{4D_{fit}\Delta t}} \qquad \text{(Eq. 16)}$$

The projection of the lipid trajectories onto the imaging plane yielded a decrease in their apparent step lengths depending on the membrane tilt (θ); this effect is considered in the simulations of single molecule trajectories described below. The localization imprecision (σ_r = 13 ± 5 nm) increased the apparent step lengths. A camera blur was caused by the single-frame exposure time (t_{exp}) being a significant fraction of the time between frames (Δt) [89,90]. The diffusion coefficient (D) was calculated from D_{fit} according to

$$D = (D_{fit} - \frac{\sigma_r^2}{2\Delta t})/(1 - \frac{t_{exp}}{3\Delta t}). \qquad \text{(Eq. 17)}$$

With σ_r = 15 nm, Δt = 20 ms, and t_{exp} = 18 ms, if D_{fit} = 0.5 μm^2/s then D = 0.7 μm^2/s or if D_{fit} = 0.1 μm^2/s then D = 0.13 μm^2/s. Since the microscopy methods used here reveal only the *z*-projection of the diffusion, D calculated from Eq. 17 is reported as D_{xy} to emphasize that only the diffusion through the *xy*-plane has been measured.

With the 50 Hz frame rate and a D = 0.2 μm^2/s, the fluorophores are expected to move an average distance of sqrt(4DΔt) = 130 nm between adjacent frames, which is a large fraction of the size of the bud. However, by averaging many single-molecule steps, we have found that lipids near the curvature on average moved less distance than expected if the local effective membrane viscosity was dependent on membrane curvature. The distance moved by the lipids within the time between adjacent frames is a large source of blurring of the data. This blurring would be significantly prominent if a MSD analysis was performed for a trajectory of n steps. MSD analyses incorporate an effective spatial blurring over the whole trajectory, which traverses sqrt(n) farther than a single step.

Diffusion coefficients from SPT are typically extracted by fitting the mean squared displacement versus Δ*t*. However, fitting a whole trajectory to a single diffusion coefficient blurs the effects of nanoscale curvature with the lipid trajectory sampling both curved and flat membranes [90]. Therefore, in the current study, a single step analysis approach was adopted to study the dynamics of lipids diffusing between curved and flat membrane.

Fluorescence recovery after photobleaching (FRAP)

FRAP is an optical imaging method utilized to study the kinetics of a diffusing label through a biological sample such as a membrane bilayer. In brief, the intensity profile of a sample is monitored, a brief exposure of a circular small spot on the sample (~2 μm in diameter) to high power laser pulse, ensures the conversion of the bright fluorescent molecules to a dark state. The

intensity within the bleached area is then recorded, a gradual increase in the fluorescence brightness within the observed area is detected. The unbleached fluorophores diffuse into the bleached region and allowed to exchange with the bleached labels within. Eventually, a uniform intensity is observed, however at a lower value than the initial pre-bleaching intensity. The fraction of the new uniform intensity to the pre-bleached steady-state intensity presents the recovered fraction of the dye. The recorded intensity profile is then fitted to[91]:

$$\mathrm{I}(t) = A\left(1 - e^{\frac{t}{\tau_D}}\right) \qquad \text{(Eq. 18)}$$

where A represents the initial uniform steady-state magnitude of the intensity, which is an indicator of the fluorophore density and laser power, while τ_D represents the characteristic recovery time. The lateral diffusion is then quantified based on the radius of the bleached spot (w) and the characteristic recovery time (τ_D) given by:

$$D_{xy} = \frac{w^2}{4 * \tau_D}. \qquad \text{(Eq. 19)}$$

3.9 Results

3.9.1 Resolution and sensitivity of PLM experimentally

PLM was used to detect engineered nanoscale membrane curvature and correlate curvature to single-molecule trajectories. PLM provided visualization of nanoscale curvature in agreement with theoretical predictions. PLM was demonstrated to provide order-of-magnitude improvements in detection and resolution of membrane curvature. Curvature in model membranes was created by draping supported lipid bilayers (SLBs) over nanoparticles (NPs) of known sizes, ranging in radius (r_{NP}) from 24 to 70 nm. The resulting membrane curvature and curvature-influenced diffusion of individual lipids were resolved. In sum, these studies demonstrate the capabilities of PLM to advance optical imaging capacities while providing order-of-magnitude improvements in spatial and temporal resolution than comparable single molecule localization microscopy (SMLM) techniques.

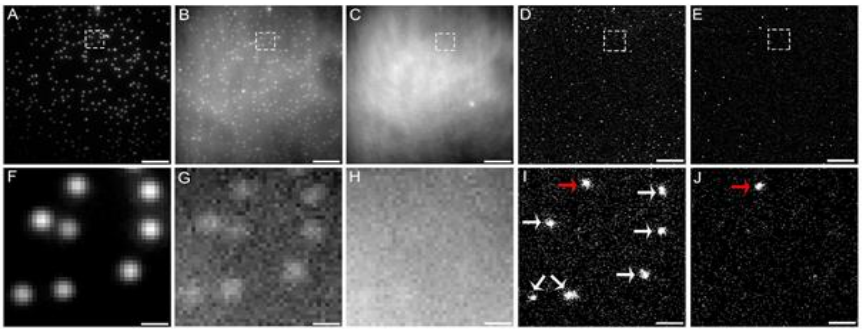

Figure 12. Engineered membrane curvature by draping a SLB over NPs. (A) The 70 nm radius fluorescent NPs on glass were imaged with λex = 488 nm. (B-C) Diffraction-limited p-polarized and s-polarized TIRFM image, respectively. (D-E) Reconstructed images of the membrane over the NPs presented as 2D histograms of the localizations in pPLM and sPLM, respectively. (B-D) The membrane was imaged with λex = 561 nm and the differences between the polarizations provide internal controls for chromatic bleed through. (F-J) Magnified images from (A-E), as indicated by the dashed boxes. The detected membrane curvature over the 70 nm NPs is indicated by white arrows. A multi-colored fiduciary mark is indicated by red arrows. Scale bars represent (A-E) 5μm, and (F-J) 400 nm.

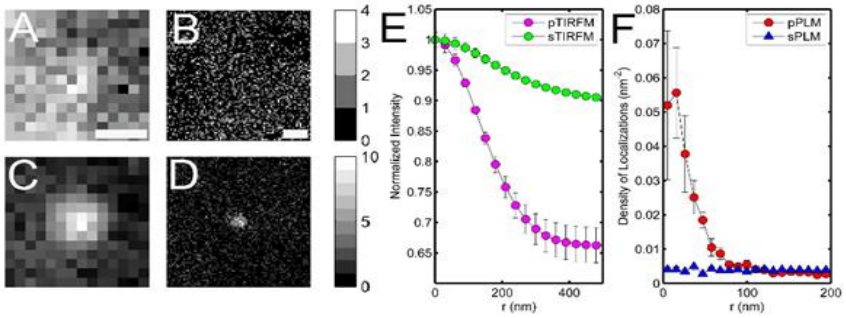

Figure 13. Membrane curvature detection over 24 nm radius NPs. (A, C) Diffraction-limited sTIRF and pTIRF, respectively. (B, D) Super-resolution reconstructed images of sPLM and pPLM, respectively. Average radial line scans (E) for TIRM and average radial density line scan (F) for PLM are for membrane over 10 NPs events of rNP of 24 nm. (E) The diffraction-limited PSF limits the ability to identify the size of each event. Error bars represent fitting uncertainty to 95% confidence bounds. (F) PLM provides improved resolution in detecting and sensitivity in detecting curvature. Error bars represent standard error of the mean. Scale bar in (A, C) represents 200 nm. Scale bar in (B, D) represents 100 nm.

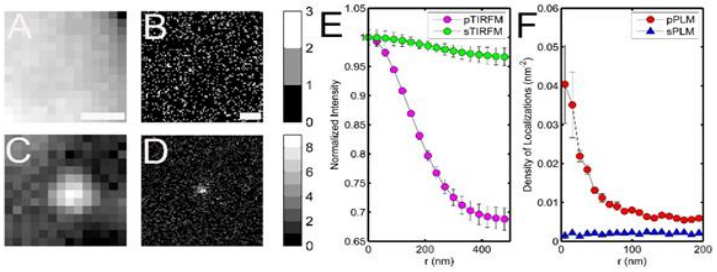

Figure 14. Membrane curvature detection over 51 nm radius NPs. (A, C) Diffraction-limited sTIRF and pTIRF, respectively. (B, D) Super-resolution reconstructed images of sPLM and pPLM,

respectively. Average radial line scans (E) for TIRM and average radial density line scan (F) for PLM are for membrane over 10 NPs events of rNP of 51 nm. (E) The diffraction-limited PSF limits the ability to identify the size of each event. Error bars represent fitting uncertainty to 95% confidence bounds. (F) PLM provides improved resolution in detecting and sensitivity in detecting curvature.(F) Error bars represent standard error of the mean. Scale bar in (A, C) represents 200 nm. Scale bar in (B, D) represents 100 nm.

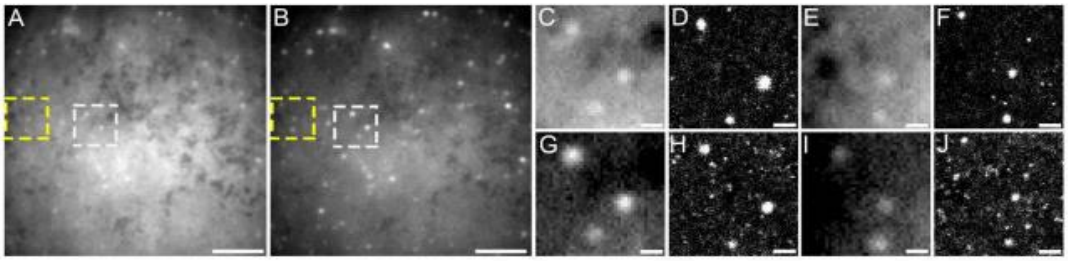

Figure 15. Membrane curvature detection of LUVs on an SLB. (A-C, E, G, I) Diffractionlimited polarized TIRFM images and (D, F, H, J) PLM images of a POPC/Biotin/DiI membrane with unfused LUVs where the excitation light was s-polarized in (A, C-F) or p-polarized in (B, G-J). (C-F) and (G-J) are magnified images for regions within the white and yellow box, respectively. Scale bars represent (A, B) 5μm, (C-J) 200 nm.

To demonstrate the ability of PLM to detect membrane curvature, we created membrane bending by three different methods: SLBs draped over NPs (Figs. 12, 13, and 14); LUVs above an SLB (Fig. 15); and unfused GUVs adhered to the glass coverslip (Fig. 16). The best control and consistency of the engineered membrane curvature came from the SLBs draped over the NPs. SLBs composed of 99.7 mol% POPC and 0.3 mol% DiI were draped over NPs to create the desired membrane topography. Continuity of the SLB over the NP was verified with fluorescence recovery after photobleaching (FRAP) (Fig. 17). This procedure was reproduced for 37, 29, and 175 NPs of r_{NP} = 24, 51, and 70 nm, respectively. pPLM provided an increased density of localizations at the site of membrane curvature and the size of the nanoscale membrane bud was measured (Figs. 18 and 19). For example, the density of localizations at the curved membrane over the 70 nm NP in pPLM was (2.2 ± 1) x10^{-6} localizations/nm^2/frame, a 27x increase over (8.2 ± 3) x10^{-8} for flat SLB (Fig. 6). As an important internal control, no significant increase in the number of sPLM

localizations was observed with nanoparticle-induce membrane curvature (Fig. 12J), which provides a second verification that chromatic bleed through from the NP was not present (Fig. 20).

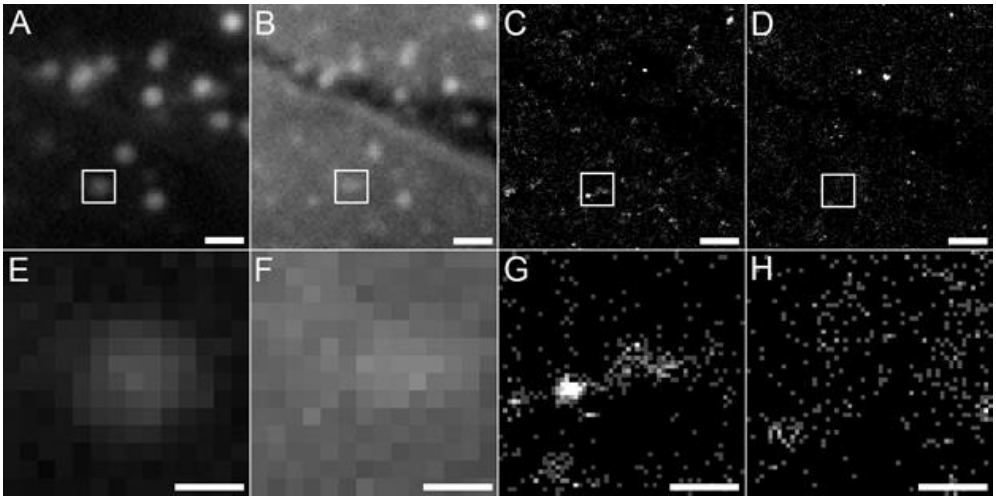

Figure 16. LUV imaging challenges. Diffusion on the SLB proved to be problematic when resolving the LUV size via PLM. A 'tail' of localizations is detected as the LUV diffused across the SLB. (A, E) Diffraction-limited pTIRFM image of the membrane, the white box labels the LUV location with an increase in brightness in the pTIRFM image indicating the presence of curved membrane. Black region is glass. (B, F) Diffraction-limited sTIRFM image, the uniform brightness within the white box indicates the presence of membrane. (C, G) Histograms of localizations in pPLM, the increased density of localizations indicate the presence of membrane curvature. The region to the right of the central bright pixels shows a lower density of localizations as the LUV diffused through this area. (D, H) Histograms of localization in sPLM demonstrate a more uniform distribution of localizations and the presence of membrane. (E-H) are zoomed in regions for marked white boxes in (A-D) respectively. Scale bars represent (A-D) 3μm, and (E-H) 300 nm.

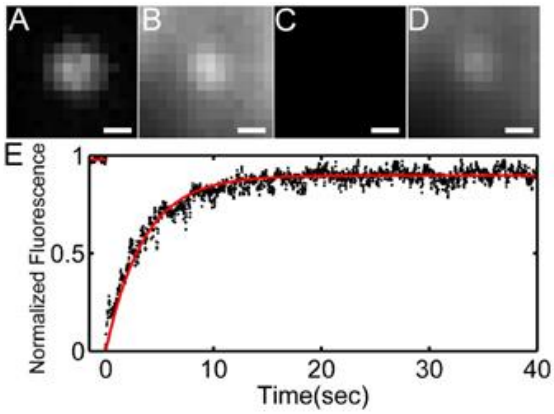

Figure 17. FRAP for SLB over NPs. Membrane draped over the nanoparticle is intact and uniform, upon performing FRAP lipids were observed to diffuse and exchange with unbleached lipids from the surrounding membrane directly on the coverslip. (A) Fluorescence image of the 24 nm radius nanoparticle with λexc = 647 nm. (B-D) Fluorescence image of POPC:DiI membrane with λex = 561 nm (B) before, (C) immediately after, and (D) 40 s after bleaching. (E) FRAP result of a 100

μm^2 of membrane overlaying sporadic nanoparticles demonstrates the bulk 0.3 ± 0.1 $\mu m^2/s$ diffusion coefficient.

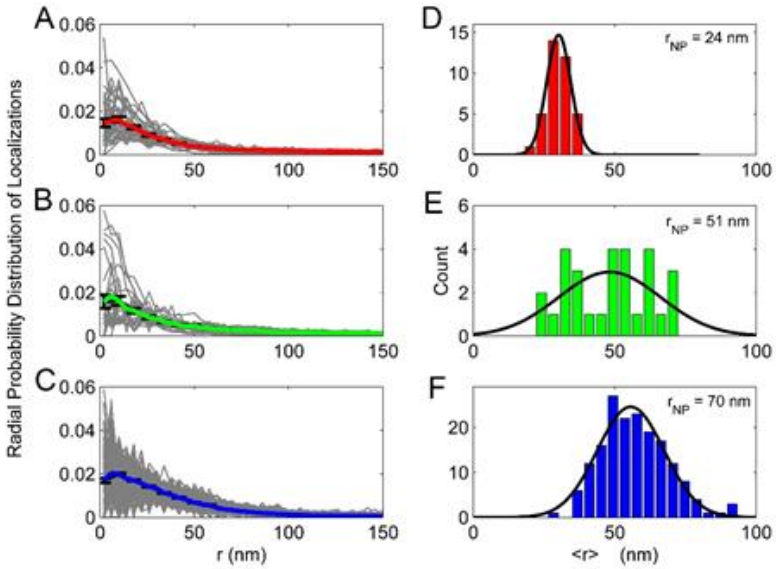

Figure 18. Probability distribution and histogram of sizes of curvature over NPs. (A-C) Radial probability distribution of localizations versus distance from the center of the curved membrane (r) over NPs for rNP = 24, 51, and 70 nm, respectively. Grey lines represent individual events and the colored lines represent the average. Error bars are the standard error of the mean at a given r. (D-F) Histograms of the radius for each curvature event (<r>) over NPs of rNP = 24, 51, and 70 nm, respectively. Black lines represent the Gaussian fits to guide the eye. The mean of the events radii was 32 ± 4, 50 ± 14, 60 ± 13 nm for rNP = 24, 51, and 70 nm, respectively.

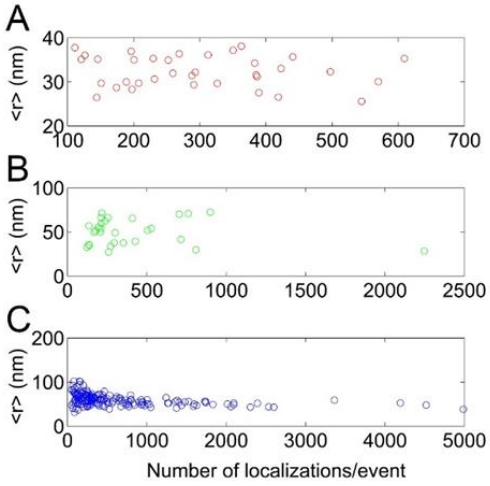

Figure 19. The number of localization obtained per curvature event induced by NPs. The higher the number of localizations/event, the more confidence in <r> is obtained. (A-C) Calculated <r> versus the number of localizations/event for rNP = 24, 51, and 70 nm, respectively.

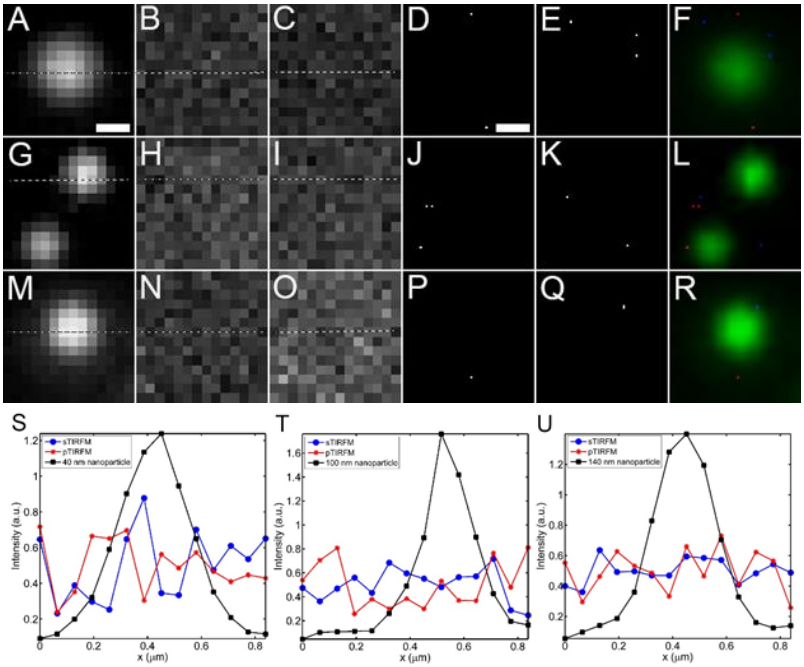

Figure 20. No fluorescent nanoparticles bleed through to membrane channel. As a control experiment, fluorescent nanoparticles on glass in the absence of a DiI were imaged and analysed with the same experimental conditions as typically done for PLM for 24 nm (A-F, S), 51 nm (G-L, T), and 70 nm (M-R, U) radius nanoparticles with primary excitation/emission wavelengths (λexc/λem) of 647nm/680nm, 488nm/508nm, and 405nm/515nm, respectively. No significant localizations were collected at the site of the nanoparticles in the absence of DiI. (A,G,M) Diffraction-limited fluorescence images of the nanoparticles.(B,H,N) Diffraction-limited pTIRFM with λexc/λem = 561nm/600nm. (C, I, O) Diffraction-limited sTIRFM with λexc/λem = 561nm/600nm. (D,J,P) pPLM with λexc/λem = 561nm/600nm. (E, K, Q) sPLM with λexc/λem = 561nm/600nm. (F,L,R) Merge nanoparticles (green), sPLM(blue), pPLM(red). Scale bars represent 200 nm.

Comparisons between the diffraction-limited images of the fluorescent polystyrene NP, the diffraction-limited polarized TIRFM images, and the reconstructed PLM images of the membrane reveals the increased resolution and detection sensitivity provided by PLM over polarized TIRF images (Fig. 12). The diffraction-limited images demonstrated the PSF of the microscope more so than the physical size of the nanoparticle or membrane curvature. The center of the curvature as determined by fitting the high localization density region in pPLM by a 2D Gaussian function according to

$$G(x,y) = A * \exp\left[\frac{-(x-x_0)^2}{2\,\sigma_x^2} + \frac{-(y-y_0)^2}{2\,\sigma_y^2}\right] + c \qquad (Eq.20)$$

where A is the amplitude, (x_0, y_0) represent the coordinates of center of the Gaussian function, σ_x and σ_y are the corresponding with in x and y direction, and c is the background count. The central peak of the Gaussian function revealed the center of the membrane curvature. The radius of each membrane bud ($\langle r \rangle$) was calculated from pPLM images by averaging the distance between each localization and the center of the bud (r). The size of each membrane bud (<r>) was set equal to the mean distance from the bud center of all extra localizations due to the bud. This was calculated by taking into consideration the background from flat SLB localizations of uniform density (ρ), the distance of each localization from the bud center (r_i), and a threshold distance that was significantly greater than <r> (R). Typically, R = 400 nm but the following calculation is independent of the particular R chosen. The number of extra localizations due to the presence of the bud (N_{bud}) is equal to the total number of localizations (N_{all}) within $r_i < R$ subtracted from the number of localizations expected within R if no bud was present (N_{SLB}); $N_{SLB} = \pi R^2 \rho = N_{all} - N_{bud}$.. The mean r_i expected for the flat SLB within R is $2R/3$. By analyzing all collected localizations within R and subtracting the expected localizations from the flat SLB, <r> is calculated according to

$$< r > = \frac{\sum r_i}{N_{bud}} - \frac{2\pi\rho R^3}{3N_{bud}} \qquad \text{(Eq. 21)} .$$

This calculation yielded <r> of 32 ± 4, 50 ± 14, and 60 ± 13 nm for membrane draped over NPs of 24, 51, and 70 nm radii, respectively (Fig. 18). Greater consistency in <r> calculations was provided when more localizations per area were detected (Fig. 19).

The sensitivity of PLM for detecting membrane curvature was especially apparent for the SLBs draped over NPs of 24 nm radii. The faint signal from the membrane curvature in diffraction-limited pTIRFM images could have gone undetected, whereas the increased density of localizations pPLM is readily apparent (Figs. 6 and 13). The increased sensitivity of PLM over

pTIRFM is especially highlighted by the evaluation of signal to noise ratios. Signal-to-noise calculations of diffraction-limited images were performed by taking the ratio of the mean intensity difference at the membrane bud divided by the standard deviation of the intensity of the surrounding planar SLB. Whereas, the signal-to-noise ratio (SNR) for the super-resolution reconstructed images was evaluated through dividing the mean signal, calculated from the number of localizations at the curvature location, by the standard deviation of the number of localizations of the flat bilayer. pPLM provided a 6x increase in the SNR over diffraction-limited p-polarized TIRFM with SNR of 11 ± 9 and 1.9 ± 0.7, respectively, where these uncertainties represent the standard deviation between events.

LUVs of with 0.3 mol% DiI were imaged with PLM. From diffraction-limited images of polarized TIFM excitation, flat SLBs were (1.8 ± 0.3)x brighter with sTIRFM than pTIRFM with the primary variability coming from laser alignment and SLB quality. Unfused LUVs above an SLB yielded (1.8 ± 0.7) more signal from pTIRFM than sTIRFM with the variability coming primarily from the LUV size. The combination of these factors yielded a 3.2 ± 0.8 fold increase in signal for LUV detection via diffraction-limited pTIRFM versus sTIRFM. pPLM yielded a 7.6x increase in localization rate when an LUV was present over an SLB with a (50 ± 20) versus (6.6 ± 0.8) $x10^{-7}$ localizations/nm^2/frame in pPLM versus sPLM. The mean and standard deviation of the LUV radii was <r> = 54 ± 29 and 57 ± 21 nm as measured by pPLM and sPLM, respectively. As a demonstration of the increased sensitivity provided by PLM, 81% of the 122 LUVs that were detected in both sPLM and pPLM were not apparent with diffraction-limited pTIRFM or sTIRFM (Fig. 21). The LUVs only detected by PLM had radii shifted to smaller values of <r> of 62 ± 20 nm while LUVs detected in PLM and TIRF possessed <r> of 72 ± 10 nm.

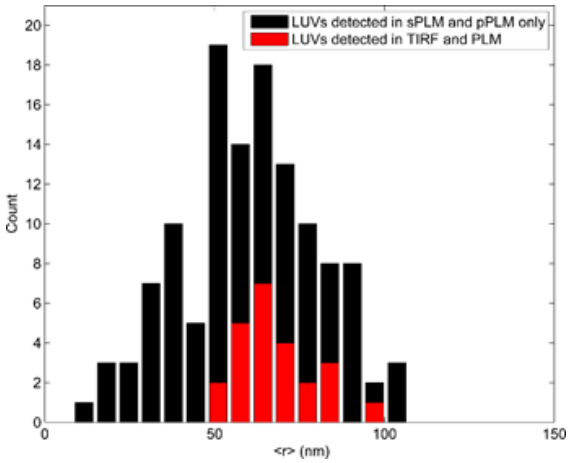

Figure 21. Probability of detecting LUVs in PLM versus TIRF for each LUV size. The increased probability of detecting LUVs in PLM versus TIRF for each LUV size. PLM not only detects and resolves the sizes of LUVs observed in TIRF, it also detects LUVs unseen in TIRF. A histogram of LUV sizes (<r>) for LUVs detected only in sPLM and pPLM but not in TIRF shown in black the mean size is 62 ± 20 nm. The red histogram represents a subset of the LUVs detected in PLM but also observed in p-polarized and s-polarized TIRF, the mean size is shifted to larger values of <r> = 72 ± 10 nm.

3.9.2 PLM temporal resolution

To reveal PLM temporal resolution, an autocorrelation analysis was performed on the PLM data. Correlation analysis measures the correlation between random localizations or variables[92]. A quantitative analysis that outputs the spatial or temporal connection between input variables. Auto correlation analysis measures the correlation within a single sample, for instance, an autocorrelation of a super resolution image reveal the local distance between clusters as well as the size of those clusters. A measurement of significant clustering and partitioning. The auto correlation function, G(***r***), quantifies the distribution of localizations within a single static image. It provides a probability measurement of finding a localization at a distance (r) from a given localization location. The width of the function reports the average cluster size, whereas the magnitude of the function represents the increased probability of clustering compared to a background of random distribution. For a distribution of localizations in two dimensions, each localization is assumed to exist at a position (***r***), with a surface defined density function ρ(***r***), where

the average density is given by $<\rho(\boldsymbol{r})> = \rho$. The autocorrelation function for such a system averaged over all positions $\boldsymbol{R}$ is defined by[93]:

$$G(\boldsymbol{r}) = \frac{<\rho(\boldsymbol{R})\,\rho(\boldsymbol{R}-\boldsymbol{r})>}{\rho^2} \qquad \text{(Eq. 22)}$$

For a random distribution $G(\boldsymbol{r}) = 1$. The correlation function is calculated using a Fast Fourier Transforms and averaged over all angles as it's considered to be rotationally symmetric. For a given reconstructed image, the image is first padded with zeros to a larger distance than the size of the image, the correlation functions are then calculated, converted to polar coordinates, binned by radius, and then plotted as a function of $\boldsymbol{r}$. In Matlab the autocorrelation function is evaluated as follow:

$$G(\boldsymbol{r}) = \frac{FFT^{-1}(|FFT(Image)^2|)}{\rho^2 * FFT^{-1}\,(|FFT(Image=1)^2|)} \qquad \text{(Eq. 23)}$$

Where the first term (G(r=0)) represents the magnitude of the inverse of the density. This is due to the convolution of the correlation function to a delta function at r = 0 position.

The cross correlation function quantifies the distribution of localization between two localization sets. For two reconstructed images I_1 and I_2 respectively, the cross correlation reveal the spatial consistency of two sets of data to match each other according to:

$$G(\boldsymbol{r}) = \frac{FFT^{-1}(FFT(I_1) * conj|FFT(I_2)|)}{\rho_1 * \rho_2 * FFT^{-1}\,(|FFT(Image=1)^2|)} \qquad \text{(Eq. 24)}$$

Autocorrelation analysis was performed on both sPLM and pPLM images with increasing acquisition time interval to find PLM temporal resolution for detecting membrane bending. The increased correlation signal indicates the acquisition time required to detect a significant clustering identified as membrane curvature compared to the surrounding flat bilayer. Data sectioning into various acquisition time intervals is required to reveal PLM temporal resolution in detecting membrane bending. The number of combined movies for reconstructing a super resolution image

for further analysis via autocorrelation function was determined by the acquisition time interval and the camera frame rate. Acquisition intervals of 0.5, 1, 3, 10, and 30 seconds were considered for super resolution image reconstruction in sPLM and pPLM. The magnitude of G(***r***) at r = 0 represent the local density of localizations which also reflects the consistent increase in the density of localizations at the curvature location in pPLM.

Results reveal the increased correlation between localizations due to the curvature detection in pPLM in comparison to the more uniform localization distributions from sPLM. Localization density rate of (1.2 ± 0.1) x 10^{-6} localizations/nm^2/frame, enabled early detection of local membrane bending over the 70 nm NPs within 1 sec in pPLM with p-value of 0.0239; for a 3 sec acquisition interval, the curvature region is detected in pPLM with a p-value of 0.0002 (Fig. 22).

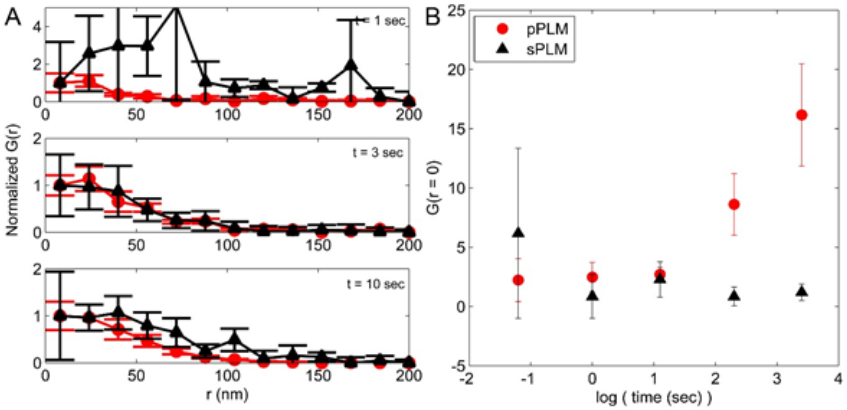

Figure 22. Autocorrelation analysis for sPLM (black) and pPLM (red). (A) Data was normalized to the first G(r) value to show the detection of curvature in pPLM with smaller error bars as time interval increases in comparison to sPLM. (B) Auto-correlation G(r) value at r = 0. The sPLM analysis provides the internal control to show the uniform bilayer analysis. An acquisition time of 1 sec is sufficient to indicate the presence of curvature in pPLM.

3.9.3 Membrane bending affects lipid mobility

The same raw data from PLM that reveals nanoscale membrane bending through image reconstruction also can be interpreted to provide single-lipid trajectories relative to the membrane bending. High-throughput SPT was performed on the raw PLM data by tracking of individual

fluorophores that were localized in sequential frames. Single-molecule DiI diffusion was observed with pPLM and sPLM to reveal the apparent diffusion coefficient in the *xy*-plane (D_{xy}). DiI that were detected in more than one frame were detected in 3.8 sequential frames on average. Analyzing D_{xy} as a function of location on the sample revealed the effects of membrane topology to lipid dynamics. In particular, D_{xy} versus distance from the center of the nanoparticle (r) revealed the curvature-induced slowing of the single lipid diffusion (Fig. 23). SPT of DiI yielded D_{xy} = 0.55 ± 0.1 μm^2/s far from the 70nm radius NP; however, within 50 nm of the center of the NP, D_{xy} = 0.03 ± 0.01 μm^2/s when detected with either p- or s-polarized excitation.

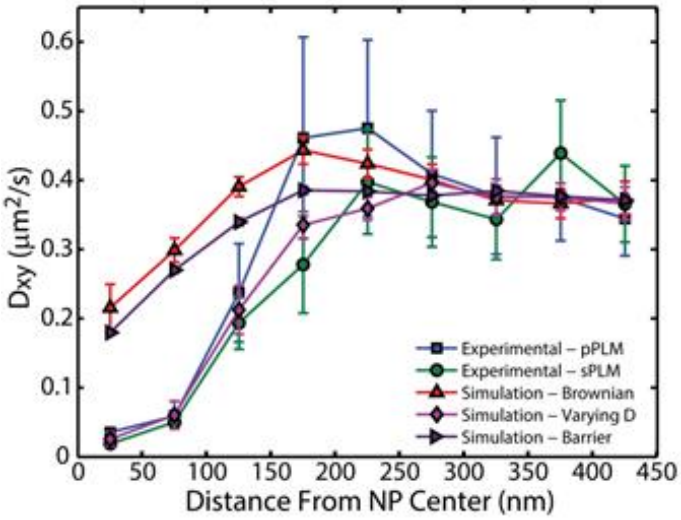

Figure 23. SPT of DiI molecules reveals slowed diffusion at the site of curvature. Slowed DiI diffusion was detected at the site of nanoscale membrane curvature equally while imaged with p- or s-polarized excitation. SLBs were draped over 70 nm radius NPs. Particle locations were projected on the xy-plane and the apparent fluorophore diffusion was affected by both the 3D membrane topology and the influences of membrane curvature on DiI mobility. Few models were used to reproduce the experimental decrease in D at the site of the membrane curvature. The fit of the distribution of step lengths yielded the apparent diffusion coefficient and the 95% confidence range, as indicated by the error bars. Neither a locally Brownian diffusion nor a simulated barrier to free diffusion surrounding the bud reproduced the experimental results. However, upon simulating a decreased local D for curved SLB to 13% of the planar SLB value, the resulting simulated D_{xy} well matched experimentally observed D_{xy}.

The geometrical effects of diffusing on a non-planar membrane can cause the observed diffusion rate through the *xy*-plane to be significantly different from the true, local diffusion rate.

For example, a simple tilt of the membrane can decrease the apparent *Dxy* by up to 50%. With localization imprecision, long imaging frame rates, sample averaging, and increased membrane area per imaging pixel, even greater ratios of D to D_{xy} are possible. By simulating the diffusion of individual DiI on the estimated membrane topography (Fig. 6C) with a constant in-membrane diffusion rate, the simulated non-planar membrane topography was unable to reproduce the experimental results while assuming a locally Brownian diffusion. In order to reproduce our experimental data, an addition mechanism for slowing the lipids at the sites of membrane curvature was needed.

One tested hypothesis was that a barrier to diffusion was preventing the lipids from transitioning between the planar SLB and the membrane bud. However, the incorporation of a diffusion barrier into our simulations that prevented single-lipid trajectories from crossing between the curved membrane bud and surrounding SLB was insufficient to reproduce the experimental data. With a 50 Hz frame rate, a local, a local D_{xy} of 0.55 $\mu m^2/s$, and a r_{NP} = 70 nm, a simulated diffusion barrier yielded only a half of the observed decrease in the observed D_{xy} at the membrane bud. Further, the FRAP results demonstrate the continuity of the membrane between the bud and the SLB (Fig. 17).

Alternatively, the hypothesis was tested that the membrane curvature induced a local change in the effective membrane viscosity. This could be caused by variations in the curvature-induced changes to the lipid packing and/or the lateral membrane tensions. This hypothesis was tested via simulations with a lipid diffusion coefficient that was slower in curved membranes than planar membranes. Simulations of lipids diffusing on a planar membrane (25 ± 5)x faster than their local diffusion on the curved membrane, well reproduced our experimental data from both sPLM and pPLM SPT (Fig. 23).

3.10 Discussion

3.10.1 Engineered membrane curvature

The method of creating SLBs primarily used in these studies incorporated the draping burst GUVs over the glass coverslip and polystyrene NPs. Draping a bilayer over NPs of known radii provided a model of physiologically similar dimensions to clathrin- and caveolin-mediated endocytosis. SLBs created by bursting GUVs were more intact and contained fewer pores than creating a bilayer via LUV fusion. However, such holes within the SLB were still feasible with this GUV-fusion method, especially when GUVs were more violently ruptured via application of GUVs to freshly plasma cleaned glass coverslips or dilution with hypotonic solutions. The continuity of the membrane between the SLB and the curvature over the NP was confirmed FRAP and long single-lipid trajectories. Both FRAP and long trajectories demonstrated that the lipids coating the NP can exchange with the lipids directly on the coverslip (Fig. 17), similar as also shown previously [94]. Examination of the continuity of the bilayer over NPs was performed by assessing the pPLM data where 94% of 290 NPs surrounded by an SLB had curved membrane draping over the NP. NPs without membrane curvature could be due to the NP being on top of the bilayer rather than under it, or the formation of a hole in the SLB directly surrounding the NP. The rare occasions in which membrane curvature did not appear at a nanoparticle gives confidence that the data we interpret as membrane curvature was not an artifact caused inherently by the presence of the nanoparticle (*i.e.*, chromatic bleed through).

An alternative membrane topography examined is that of the LUVs bound to an underlying SLB, which resembles vesicle docking in endocytosis and the later stage of exocytosis that precedes vesicle fission in cells. The variation of LUV sizes obtained by extrusion was demonstrated by PLM (Fig. 20). Other studies of vesicle sizes produced by extrusion through 100

nm pores have found the average diameter of extruded LUVs to be 65 ± 30 nm [95] indicating that the extrusion process produces a variation of LUV sizes with an upper diameter limit comparable to the extruder filter pore size. Taking advantage of PLM sensitivity and resolution, our reported values are in agreement with previous reports of LUVs size distributions imaged via SEM [95].

3.10.2 Membrane topography over NPs

The demonstration of PLM performed here measured nanoscale hemispherical membrane curvature of an SLB draped over NPs ranging in radii from 24 to 70 nm. Prior methods of inducing nanoscale curvature utilized nanoengineered wavy glass substrates [96], microfabricated structures [97,98], membrane tubule pulled from GUVs [17], and SLBs on deformable substrates [99,100]. However, wavy glass substrates, thick polymer structures, and lipid tubules are not compatible with TIRF excitation. The method of draping a membrane over fluorescent NPs of known size, as done here and previously [94,101,102], was effective for engineering nanoscale membrane curvature, testing the capabilities of PLM, and revealing the effects of curvature on lipid mobility.

A comparison between sPLM and pPLM results provided confirmation of numerous aspects of our results. At the location of the NP-induced membrane curvature, a near uniform density of localizations in sPLM was detected whereas >5x increase of localizations in pPLM was observed (Figs. 12 and 6A). This confirms that there was no significant chromatic bleed through from the fluorescence emission of the NP, that the refraction of the excitation light by the NP did not catastrophically alter the excitation light polarization, and that there was no significant Förster resonance energy transfer between DiI and the NP disrupting the polarization dependence of the signal. However, refraction by the NP may have influenced the direction of the DiI emission.

Nanoparticle-induced lensing has the potential to cause a systematic shift in the perceived location of a fluorophore from its actual position, similar to the anisotropic emission effects.

Lensing effects were coarsely estimated by considering the ray trajectories leaving a point source in water that was 5 nm away from the polystyrene nanoparticle and imaged by a thin lens. The changes in index of refraction from the water, the polystyrene, and the coverslip yielded a slight shifting of point spread function such that the nanoparticle lensing shifted the single-fluorophore images towards the center of the nanoparticle on the imaging plane. However, this effect was of lower magnitude than the anisotropic emission, and incorporating of the high index of refraction of the polystyrene nanoparticle in the simulations was not necessary for theoretical reproduction of our experimental results.

Further, the polystyrene nature of the NP and its high index of refraction (1.59) had no effects on the acquired data and curvature detection. Several control experiments have been carried out to confirm that the nature of the NP did not interfere with the presented results. First, a natural control would be to compare the super resolution images collected in sPLM and pPLM. The membrane is expected to exhibit uniform localization density in sPLM and a high localization density at the site of the NP-induced curvature in pPLM. Experimental observations fall in agreement with expected distribution of localizations, and the lack of similarities between sPLM and pPLM confirms that the nanoparticle itself had no effect on the collected data. For instance, for a membrane artifact such as a hole or a tetraspec, the localization density distribution would appear to be similar for both sPLM and pPLM images. Second, curvature generation without the use of NP, such as LUVs, GUVS, and Cholera toin subunit B (CTxB)-induced budding yielded the expected membrane-orientation dependence of PLM localization densities. Third, no chromatic bleed though was detected from the nanoparticles. NPs on glass, with no DiI labelled membrane, exhibited no additional localizations in PLM. Finally, modeled theoretical simulations without the incorporation of the index of refraction of the NP reproduced the presented data. This

indicates that the index of refraction of the NP did not affect the results and is not required to match experimental data. However, if a larger polystyrene nanoparticle was used (radius > 400 nm) the TIRF illumination would have been compromised and the reported results would change.

The membrane topology over the NPs depended on the adhesion between the lipids and the polystyrene NP, the adhesion between the lipids and the glass coverslip, the size of the NP, the membrane bending rigidity, the lateral membrane tension and pressure, and the packing properties of lipids [102,103]. POPC, the dominate lipid in these experiments, has no intrinsic curvature and forcing a POPC bilayer to bend would cause an unfavorable packing of the lipids. For a positive membrane curvature, the lipid tails are crowded while the head groups are stretched over more area. For a negative membrane curvature, the lipid head groups are crowded while the lipid tails are given more volume to occupy. Both of these configurations are unfavorable for POPC and apparently result in slowing the diffusion of a fluorescent lipid through the crowded environments.

We modeled the shape of the membrane over the NPs to be primarily spherical in shape with a smooth 20 nm radii of curvature bend to connect to the planar SLB (Fig. 6C). This consistent radius of curvature for the connection of the SLB on the NP to the SLB on the coverslip resulted in a tent-like transition from the top of the small NPs to the glass substrate and a neck-like feature at the transition from the large NPs to the coverslip. The tent-like membrane structure would have a bigger size than the small NPs; the neck-like membrane structure would have a smaller size than the large NPs (Figs. 18 and 6C) [102]. The tent-like model may represent the initial stages of membrane bending upon the initiation of endocytosis or conclusion of exocytosis; the neck-like model represents the later stage of endocytosis or early stage of exocytosis. The agreement between the experimentally measured and theoretically predicted radial density profiles suggest

the accuracy of both the membrane model and the theoretical analysis of localization probabilities (Fig. 6 and Eq. 9).

3.10.3 Limitations to resolution

The distribution of localizations around the nanoparticle-induced membrane buds was influenced by multiple effects that limit the experimental determination of the membrane topography, including (1) localization imprecision of the individual fluorophores, (2) anisotropic emission from the membrane-confined DiI, (3) finite localization rates, (4) NP-induced emission lensing, (5) the fitting of multiple '*on*' fluorophores as if they were a single fluorophore, and (6) membrane curvature motion within the sample (*i.e.*, NP or LUV drift) (Fig. 19). Each of these contributions has been theoretically tested in attempts to match theoretical predictions to the experimental observations.

Localization imprecision

The localization imprecision was limited primarily by the number of photons collected from each fluorophore in each frame. The localization software, ThunderSTORM, accounted for the camera quantum efficiency and imaging noise to estimate the number of photons and the localization precision for each detected fluorophore. 1200 ± 800 photons/fluorophore/frame were acquired yielding a localization precision of 13 ± 5 nm. For the simulated membrane topography, the experimental localization imprecision of $\sigma_r^2 = 2\sigma_{xy}^2$ was incorporated, and the distribution of random numbers with a standard deviation of σ_{xy} (Σ) was used. The simulated step lengths were then calculated as

$$v(t_S) = \sqrt{(x(t_s) - x(t_s + 6400) + 2\Sigma)^2 + (y(t_s) - y(t_s + 6400) + 2\Sigma)^2} \quad \text{(Eq. 25)}$$

Further information regarding the acquired number of photons/fluorophore and the uncertainty for the different NPs sizes are show in the corresponding figures and table. (Figs. 8,

9). Incorporating the localization imprecision in the simulations, a standard deviation of σ_{xy} (Σ) was added to each (x,y) location of the simulated diffusing lipid, affecting its simulated step lengths as shown in Eq 25.

Anisotropic emission from the membrane-confined DiI

The restriction of DiI within the plane of the membrane provide its unique polarization sensitive characteristic; however, the non-free-tumbling nature of this membrane label give rise to a collected anisotropic emission pattern and a systematic inaccuracies of DiI localization. The emission patter of the fluorophore strictly depends upon its distance from the glass-sample interface, and its orientation (ϕ) within the membrane. This induces a systematic shift in the apparent location of the DiI molecule within the membrane. The anisotropic emission contributed to the single lipids being localized at a location distinct from their true location dependent on the orientation and height of the membrane. The effects of rotationally confined fluorophores can yield lateral localization inaccuracies up to 100 nm upon defocusing by 200 nm [104]. While the DiI is not rigid in one location and can explore all ψ values in addition to a tilt of ß = 69°, some orientation averaging occurs for each single DiI image. Even still, the anisotropic emission results in a systematic shift up to 100 nm of the single fluorophore localizations towards the center of the NP.

Numerical integration yielded the magnitude and direction of the shift in localization position due to the single fluorophore orientation and height above the focal plane following the framework of Agrawal et al. [105]. The expected PSF and lateral shift were estimated as a function of membrane orientation (θ and φ) after considering the expected fluorophore orientations within the membrane (ψ and β). Accordingly, the expected lateral shifts as a function of membrane orientation and height were calculated. This systematic shift was incorporated into our simulated image reconstruction and SPT results, proving to be critical for matching the experimental data.

Since the magnitude of the anisotropic emission effects vary greatly with distance between the single fluorophore in the membrane and the focal plane, and since this distance was difficult to experimentally assess, the magnitude of defocusing and lateral shifting was fit to match experimental and theoretical results. From this, we modified the simulations to include an anisotropic emission effect. In brief, a perceived location was calculated for each lipid actual location at each simulated time.

Finite localization rates

The finite localization rates result in a finite number of localizations per membrane budding event. With greater localizations, greater precision could be gained in detecting the center of the membrane bud, the local membrane orientation, the radial density of localizations, and the spatial mapping of the lipid diffusion rate. The upper limit on localization rates in all SMLM methods is based on the camera frame rate and the length scale of diffraction-limited imaging. Localization rates could be increased above those reported here by increasing density of DiI in the sample, or optimizing the DiI *on*-and *off*-rates with further buffer or incident light optimization. Further, the limited final number of localizations yields uncertainty in analyzing the precise local membrane orientation and the center of the membrane bud.

NP-induced emission lensing

The nanoparticle-induced lensing effect descried previously mainly alter the evanescent field and convert it into a propagating light in all directions independent of polarization.

False fitting

When performing SMLM, such as PLM, a key component of data analysis is the fitting of single-fluorophores that are sufficiently separated for computational fitting (>200 nm apart); however, if multiple fluorophores were in close proximity to each other (<100 nm) and falsely

interpreted as a single fluorophore. When two fluorophores are ‘on’ and treated as a single fluorophore’s image, errors will result in the data analysis and interpretation. Typically, this error is predictable by assuming a uniform time-averaged fluorophore density, estimating the mean separation distance between fluorophores, and calculating the probability of multiple fluorophores being within the diffraction-limited range from each other. However, for pPLM, the assumption of a uniform time-averaged fluorophore density may not be appropriate.

With pPLM, the fluorophores on the membrane that are parallel to the coverslip, which is most of the membrane, are less likely to be excited and less likely to be turned ‘off’ than with s-polarized illumination. Accordingly, it would be expected to have a higher concentration of ‘on’ fluorophores during pPLM than sPLM. This higher concentration of ‘on’ fluorophores coupled with the increased probability of detecting fluorophores when they are on the sub-diffraction-limited membrane bud, would increase the probability that raw pPLM images would be more likely to yield multiple ‘on’ fluorophores simultaneously on the membrane bud than raw sPLM images. If multiple ‘on’ fluorophores were averaged simultaneously, and fitted as a single fluorophore, the resulting fit center would be biased towards the center of the membrane bud.

This effect was simulated by considering a Poissonian distribution of fluorophores simultaneously ‘on’ on the bud. As expected, by increasing the number of simultaneously ‘on’ fluorophores, the distribution of localizations became higher near the bud center. However, this effect proved to be unnecessary to reproduce the experimental data. If mistakenly fitting multiple fluorophores as a single fluorophore lead to a significant shift in the localizations, deviating them toward the center of the bud, and eliminating the possibility of observing a ring-like structure of localizations in pPLM, then confirming fitting a single fluorophore would retrieve the ring-like structure. Toward this aim, further experiments utilizing lower DiI concentrations in the membrane

(0.001%), aimed to have lower localization rate, and thus lower 'on' fluorophores per frame. Even with these experimental conditions, no ring-like distribution of localizations was obtained.

Membrane curvature motion within the sample

Error in localizing the center of the membrane bud (σ_b) result in error determining the lipid behaviors versus distance from the bud center (r). In the simulations, r for a single lipid step was calculated according to

$$r(t) = \frac{1}{2}\sqrt{(x(t_s) + x(t_s + 6400) + \sigma_b)^2 + \big(y(t_s) + y(t_s + 6400)\big)^2} \quad \text{(Eq. 26)}$$

Experimentally, 200 ± 100 localizations per membrane bud were collected, each with a radius of 30 to 60 nm, which resulted in an uncertainty in identifying the bud center by 3 ± 1 nm, by standard error of the mean analysis. Thus σ_b was found equal to 3 ± 1 nm, and this value was put into the simulations of D_{xy} versus r. In some experimental conditions, the membrane bud was observed moving over time and this could be incorporated into the simulation by allowing σ_b to have a time dependence and/or fluctuation in the analysis of the simulation results.

It was found that the single-fluorophore localization imprecision, anisotropic emission effects, and bud center identification proved to be the only error sources needed to theoretically reproduce the experimental data. Matching the experimental data with theoretical estimates required no NP-induced emission lensing nor multiple '*on'* fluorophore misassessements.

3.10.4 Curvature affected lipid diffusion

Analyzing D_{xy} versus distance from the NP center demonstrated how the lipid diffusion slowed at the membrane buds equivalent to as if the membrane bending caused an increase in effective viscosity (r). With greater experimental sampling densities, rates, and precision, a more sophisticated simulation and analysis routine would be warranted [90]. The sequential frame linking

and analysis performed here resulted in the average single-lipid step sampling a distance between 60 and 200 nm, depending on the local diffusion coefficient, which is comparable to the size of the NPs. However, the curvature-dependent single-lipid step length observed here is dramatic and was able to be modeled computationally by incorporating the experimental data conditions, such as frame rate, localization precision, anisotropic inaccuracies, and membrane topography.

The diffusion of DiI apparently slowed when the membrane was curved over the NP. The change in membrane topography from flat to the curved membrane over the NP alters DiI diffusion observed in both s- and p-polarization, resulting in a decrease in the observed diffusion coefficient within the membrane (Fig. 23). Since the diffusion analysis from the sPLM and pPLM data yielded indistinguishable effects of membrane curvature on lipid mobility, the illumination polarization did not apparently affect the observed diffusion coefficients. When a membrane is tilted ($\theta > 0$), a 2D Brownian diffuser apparently moves slower as imaged in the *xy*-plane; however, this geometrical effect alone was not sufficient to reproduce diffusion rates extracted from experimental data. Further, a diffusion barrier between the membrane bud and the surrounding planar SLB was not sufficient in matching the modeled and experimental data. However, combining both the geometrical effects of the tilted membrane and a curvature-dependent effective membrane viscosity yielded a strong agreement between the modeled and experimental SPT results. This analysis supports the hypothesis that DiI diffuses slower on more curved membranes due to change in membrane properties such as effective membrane viscosity or lipid packing, as suggested previously [94].

Neither the experimental data nor the simulated theoretical reproduced data for D_{xy} distinguishes between the two leaflets of the lipid bilayer. The SLBs were symmetrically labeled through the addition of DiI to the lipid mixture before GUV electroformation, and both bilayer

leaflets contributed to the observed DiI diffusion rates. DiI in the outer leaflet would have minimal direct substrate interaction, whereas DiI in the inner leaflet would be in close proximity to the supporting polystyrene NP or glass coverslip. However, our control experiments have failed to find a substrate-induced slowing of the single-lipid diffusion. We have created stacked SLB structure with between 1 and 5 bilayers layered over the coverslip and we have not detected any difference in the distribution of single-lipid step lengths versus number of bilayers present; the cushioning of a SLB by additional SLBs did not apparently affect the single-lipid diffusion. Accordingly, this suggests that the substrate differences between the glass coverslip and the polystyrene nanoparticle are unlikely to affect the single-lipid step lengths reported here. Further, single-lipid diffusion has been observed to be slower when nanoscale membrane buds are formed by cholera toxin subunit B (CTxB) rather than a nanoparticle [106].

Diffusion rates measured by SPT, FRAP, and fluorescence correlation spectroscopy (FCS) show systematic variations in the measured diffusion coefficients depending on the analysis method. Comparisons between these techniques requires accounting for their difference in sensitivity to detecting mobile versus immobile diffusers, length and time scale dependent processes, and subpopulations of diffusers [89,90]. The SPT results presented here are consistent with prior SPT results and, as expected, report a slower diffusion rate than FRAP or FCS measurements [101,107].

3.11 Future improvements to PLM

PLM is able to provide super-resolution detail on membrane orientation with improved sensitivity and resolution from comparable methods. Since PLM requires no manipulation of the fluorescence emission path or the PSF, the incorporation of PLM with SMLM in additional complementary color channels is straightforward. For example, the simultaneous super-resolution

membrane orientation detection via PLM with the curvature-sorting and curvature-induction effects of CTxB is the focus of the next chapter [106].

It is feasible that the local membrane orientation could be evaluated by the direct mapping of acquired localizations per pixel to the PLM theory. In order to perform such analysis, a minimal localization density of 0.05 localizations/nm^2 would be required. PLM has the advantage of observing lipids that diffuse into the region of view from the surrounding membrane to effectively achieve unlimited labeling densities, similar to as has been previously utilized in point accumulation for imaging in nanoscale topography (PAINT) [108]. Analogous to FRAP, if all the fluorescent lipids diffused at a rate of 0.5 μm^2/sec and were all permanently bleached within a 4 μm diameter observation area, then the half time for lipid exchange would be 0.9 seconds, which is significantly shorter than the typical movie acquisition time and membrane curvature dynamics.

Greater sampling statistics would enable finer details of membrane topology to be extracted with more statistically significant comparisons between pPLM and sPLM localization densities. However, detection of the presence and size of membrane curvature, as done here, is sufficient for determining the spontaneous curvature formation by membrane-bound proteins and the curvature-affected molecular diffusion.

3.12 Conclusions

Polarized localization microscopy (PLM) is capable of detecting and resolving nanoscale membrane curvature with super-resolution and correlating this curvature to the single-molecule diffusion and molecular sorting. PLM provides fluorophore orientation with conventional detection optics, minimal adjustment of the excitation optics, and the use of commercial fluorophores. PLM requires no alteration of the emission path from traditional single-molecule fluorescence microscopes and incorporates no inherent sacrifice in the signal or localization

precision for observing the membrane orientation. PLM depends on the use of rotationally confined fluorophores that maintain an orientation relative to the membrane normal [33] and photo switch between fluorescent bright and transient dark states [109,110], such as the indocarbocyanine dye DiI.

Distinct identification between membrane topology of LUVs, GUVs, and curved SLBs over NPs were observed. The nanoparticle-patterned substrate provided a means to engineering nanoscale membrane curvature of physiologically relevant dimensions. Local membrane bending regions with radii of curvature ≥24 nm were detected. PLM detected membrane curvature and resolved membrane topography with 1 sec of acquisition time at (1.2 ± 0.1) x 10^{-6} localizations/nm^2/frame.

Radial line scans of pPLM localizations reveal radii of curvature of 32 ± 4, 50 ± 14, 60 ± 13 nm for membranes over the nanoparticles radii of 24, 51, and 70 nm, respectively. Further, a 6x increase in the SNR is obtained by PLM over traditional TIRFM. The theoretically estimated localization probabilities versus membrane orientation well reproduced experimental data. The unique spatiotemporal resolution of PLM is suited to monitor membrane structure variation with lipid and protein dynamics. We envision that this microscopy technique will provide new information for previously untestable nanoscale processes coupled with a change in membrane topography. This was demonstrated by the observation of time-dependent membrane budding initiation and growth induced by cholera toxin subunit B in quasi-one component lipid bilayers, revealing a possible mechanism of cholera immobilization and cellular internalization described further in the next chapter[106]. Fundamental questions regarding nanoscale cellular processes such as clathrin-independent endocytosis, viral infections, endocytosis/exocytosis, and immunological responses are soon to be addressed with PLM. The feasibility of performing PLM on model

membranes or live cells on time scales suitable for observing cellular processes permits this technique to be adopted and broadly used to probe cellular dynamics.

CHAPTER 4: CHOLERA TOXIN SUBUNIT B INDUCES CURVATURE

4.1 Introduction

Membrane function is governed by the molecular organization, clustering, and interaction of its constituents. In particular, curvature-dependent reorganization has captured a growing interest as a mechanism for creating locally distinct membrane environments [96,111,112]. In this chapter, we focus on the membrane bending effects of cholera toxin subunit B (CTxB) in a quasi-one component model membrane. Cholera toxin is a member of the AB5 toxin family that multivalently binds to GM1 and is most frequently used as the lipid raft marker in biophysical studies [113]. CTxB-GM1 partitions with order-preferring lipids [114,115], induces lipid phase segregation [115–117], and sorts to high curvature regions [96,112]. GM1 plays a vital role in numerous biological functions including endocytosis [118], viral egress [119], Alzheimer disease [120,121], vesicular trafficking [122], and immunological signaling [123].

CTxB and GM1 assumes a sequence of macromolecular complexes from its initial membrane binding, local clustering, and subsequent cellular internalization. Accordingly, numerous observations of multi-modal diffusion and nanoscale confinement of CTxB on living cells [124] and on synthetic bilayers [125,126] have been reported. Even in the absence of coexisting lipid phases, CTxB exhibits multiple populations of diffusion rates and transient confinement in regions as small as 20 nm in radii [125,126]. On living cells, CTxB diffusion is independent of the diffusion of caveolin, clathrin, or glycosylphosphatidylinositol-linked proteins, which suggests the internalization of CTxB is initialized distinctly from conventional endocytotic processes [127–129].

Inward membrane vesiculation and tubulation has been observed in cells and synthetic vesicles upon exposure to Cholera toxin [119,130,131]. CTxB has been observed to sort to membranes of negative curvature for supported lipid bilayers (SLBs) on wavy glass [96], micron-scale

nanoparticles [97], and membrane tethers [112]. The capability of CTxB to bind to membranes in which both of the local principle curvatures are negative (*i.e.*, with a positive Gaussian curvature) is well established with CTxB-induced inward pits in giant unilamellar vesicles (GUVs) [132]. This is supported by molecular dynamics simulations of the structurally similar Shiga toxin [132]. However, the nanoscale details of CTxB intrinsically inducing membrane curvature, as necessary for endocytosis, and the capability of CTxB to bind to membranes with differing signs of principle curvatures remains uncertain.

4.2 PLM detects nanoscale membrane curvature

We hypothesize that CTxB aggregates and internalizes as a result of its inherent physical effects on the membrane topography. Testing this hypothesis requires the use of an examination method that is able to resolve the colocalization of nanoscale membrane bending with CTxB. Polarized localization microscopy (PLM) combines single-molecule localization microscopy (SMLM) with polarized total internal reflection fluorescence microscopy (TIRFM) to detect nanoscale membrane orientation with super-resolution [133]. This technique distinguishes between membranes of varying orientation due to the differential excitation of membrane-confined fluorophores depending on the linear polarization of the incident excitation light. In particular, indocarbocyanine dyes (*e.g.*, DiI) are photo-switchable probes [134] that maintain their fluorescence dipole moment in the plane of the membrane [135,19,40], such that membranes parallel to the coverslip are preferentially excited by incident s-polarized light, and membranes vertical to the coverslip are preferentially excited by incident p-polarized light. The robust identification of nanoscale membrane bending provided by PLM enables the correlation of membrane topography and molecular sorting on physiologically relevant length scales (<50 nm) with numerous technical advantages over other super-resolution techniques [133].

The microscopy setup for PLM permits simultaneous multicolor SMLM and single-particle tracking (SPT) of lipids and proteins. For example, Alexa Fluor dyes are commonly conjugated to proteins with flexible linkers such that the fluorescence excitation of dyes as no observed dependence on the illumination polarization. Such dyes are common probes for imaging via direct stochastic optical reconstruction microscopy (dSTORM) [81]. As demonstrated here, the multi-color, simultaneous combination of PLM and dSTORM enables the determination of membrane organization, molecular sorting, and single-molecule diffusion relative to membrane bending.

In this study, we report the nanoscale organization and dynamics of CTxB relative to membrane bending events on a supported lipid bilayer (SLB) with 99.4% 1-palmitoyl-2-oleoyl-sn-glycero-3-phosphocholine (POPC), 0.3% DiI, and 0.3% GM1. Using PLM, we found that the SLBs initially exhibit a flat uniform topology before the addition of CTxB. Nanoscale membrane bending and bud formation occurred within 30 sec upon the addition of CTxB. The subset of CTxB coincident with membrane budding became clustered and slowed to (19 ± 9)% of the initial CTxB diffusion rate. Similarly, only the DiI coincident with the membrane budding demonstrated diffusion that was slowed to (18 ± 4)% of the diffusion rate of DiI in a planar SLB. At later times after CTxB addition (>20 min), freely diffusing CTxB on planar bilayers, small accumulations of CTxB on nanoscale membrane buds, and rings of CTxB at larger membrane protrusions were simultaneously observed (Fig. 24). Both single event analysis and spatially averaged correlation analysis demonstrated the strong interdependence of membrane structure, single-molecule dynamics, and CTxB accumulation. In sum, these studies represent, to the best of our knowledge, the previously undetected phenomena of nanoscale membrane budding and tubulation by CTxB on SLBs without the apparent need of lipid phase separation. PLM has enabled observing the

effects of CTxB on spontaneous molecular sorting, immobilization, curvature, and tubule formation processes.

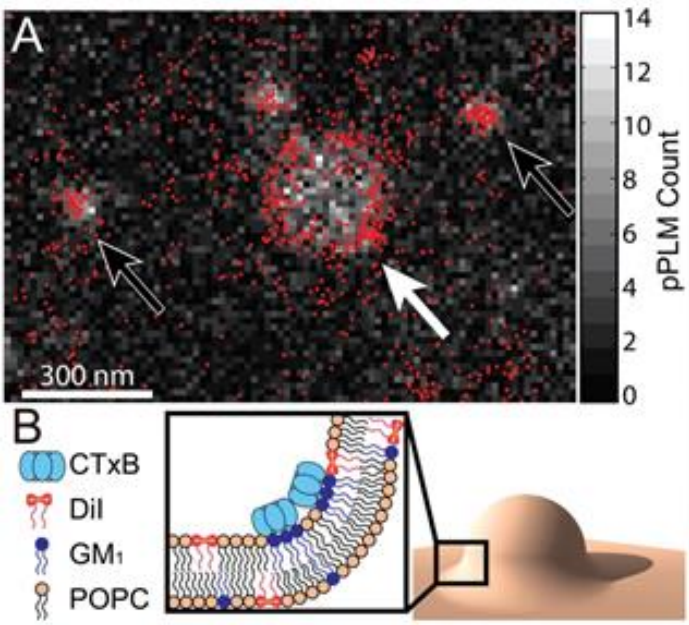

Figure 24. The inherent capability of CTxB to induce membrane curvature. Colocalization of CTxB accumulations and membrane bending on supported lipid bilayers demonstrate the inherent capability of CTxB to induce membrane curvature. (A) The 2D histogram of DiI localizations with p-polarized excitation highlights where the membrane is more perpendicular to the coverslip. This is overlaid with the single-molecule localizations of CTxB that are displayed with red points. The membrane is bending where CTxB is concentrated. Larger membrane buds, as indicated by a white arrow, shows the high concentration of CTxB preferentially at the neck of the bud, where the membrane has a negative Gaussian curvature, as shown schematically in (B). Smaller membrane buds, as indicated by black arrows, display a local accumulation of CTxB, although identification of where on the small buds CTxB is most concentrated is not feasible at this resolution.

4.3 MATERIALS and METHODS

SLB formation

Giant unilamellar vesicles (GUVs) of primarily POPC (Avanti Polar Lipids, Inc.) with 0.3 mol% 1,1'-didodecyl-3,3,3',3'-tetramethylindocarbocyanine perchlorate (DiI, Life Technologies) and 0.3 mol% GM1 Ganglioside (Avanti Polar Lipids, Inc.) were prepared by electro-formation, as described previously [136]. Experiments were also repeated by using diphytanol phosphatidylcholine (DPhyPC, Avanti Polar Lipids, Inc.) instead of POPC and DiO or DiD instead

of DiI with indistinguishable results. This composition yielded 110 nm^2 of bilayer per DiI or GM1 molecule. In brief, GUVs were formed by mixing lipids in chloroform and spreading them uniformly on a conducting indium tin oxide (ITO)-coated slide (Sigma-Aldrich) via spin coating. The resulting lipid films were dried under vacuum for one hour. A second ITO-coated slide and silicon spacer enclosed the dried lipids into an incubation chamber. A hydration buffer of 200 mM sucrose was added to the dried lipid films and the ITO slides were connected to either side of a sine wave function generator. The growth of the GUVs occurred over 3 hours at 55 °C with an alternating field at 10 Hz and 2 V_{rms}. GUVs were stored at 55°C until use or discarded after 2 days. The interaction between the GUVs and plasma cleaned glass coverslips resulted in bursting of the GUVs and the formation of a continuous SLB over the glass.

CTxB addition

CTxB was labeled with Alexa Fluor 647 or Alexa Fluor 488 prior to purchase (Thermo Fisher Scientific, Inc.). CTxB was added to the SLB for a final concentration of 0.25 μg/mL above the SLB to saturate all available GM1. After 0.5 min of incubation, the unbound CTxB was rinsed away. The time (*t*) is said to equal zero before CTxB was added, and otherwise, *t* reports the time since the unbound CTxB was rinsed away. CTxB-Alexa Fluor 647 was used for all data shown below and indistinguishable results were obtained with CTxB-Alexa Fluor 488.

Engineered membrane curvature

For select experiments, membrane curvature was engineered prior to the addition of CTxB, as done previously [133]. 70 nm radius polystyrene nanoparticles (r_{NP}) of λ_{ex} =488 nm (Fluoro-Max, Fisher Scientific) were exposed to a plasma cleaned coverslip of a glass bottom dish for 10 min to achieve a density of 0.02 NPs/μm^2. Glass bottom dishes were placed on a 55 °C hot plate for 5 min to ensure their stability on the coverslips. GUVs were draped over the nanoparticles and

coverslip to create the engineered membrane curvature for greater consistency in membrane bud size when needed. The index of refraction of polystyrene is 1.59 and may have resulted in a nanoscale shifting of the localization of single fluorophores, as discussed below.

Imaging optics

PLM was performed with an inverted IX83 microscope with Zero-Drift Correction and a 100x, 1.49NA objective (Olympus Corp.) on a vibration-isolated optical table. The various optical components such as lasers, dichroic mirrors, liquid crystal wave plate, shutters, and filter wheel are the same for PLM setup described in the previous chapter. Image acquisition was performed with an iXon-897 Ultra EMCCD camera (Andor Technology) proceeded by an OptoSplit IILS (Cairn Research) with emission filters (BrightLine, Semrock, Inc.), a 4-band notch filter (ZET405/488/561/640m, Chroma Corp.), and a 2x magnification lens.

Imaging procedure

The sample was exposed to >80 mW of excitation light with λ_{ex} = 561 (DiI) and λ_{ex} = 647 nm (CTxB-AF647) simultaneously. Exposing the sample to high lasers powers for 3 s resulted in converting most of the fluorophores from their fluorescent state '*on'* to the transient non-fluorescent, dark state *'off'* to provide a steady state of well-separated fluorophore blinking. The '*on'* fluorophores were imaged at a density of less than one '*on'* fluorophore/μm^2/frame. Data was acquired simultaneously for p-polarized total internal reflection (TIR) excitation at λ_{ex} = 561 nm for pPLM, and epifluorescence excitation at λ_{ex} = 647 nm for dSTORM. Between 10,000 and 30,000 frames were acquired for each time point at a frame rate of 50 Hz on a region of interest with 18 ms acquisition per frame (t_{exp}). Reproduced experiments utilized DiO (λ_{ex} = 488 nm) with CTxB-AF647 (λ_{ex} = 647 nm), and DiD (λ_{ex} = 647 nm) with CTxB-AF488 (λ_{ex} = 488 nm) in order to spatially separate the different color channels and minimize any possible bleed through. Further,

this presented an internal control to confirm that the CTxB label Alexa fluorophore or its possible aggregation was not the driving reason for the observed membrane curvature.

Imaging buffer

PLM was performed on samples present in an oxygen-scavenging buffer (150 mM NaCl, 50 mM TRIS, 0.5 mg/mL glucose oxidase, 20 mg/mL glucose, 40 µg/mL catalase, and 1% β-mercaptoethanol (BME) at pH 8). To obtain the optimal number of photons/fluorophore and increase our localization precision for DiI and CTxB-AF647, we explored a range of pH starting from a pH of 7.4 [137] up to a pH of 8 [134]. Using pH of 8 in our system for the localization buffer allowed us to collect a 1200 ± 800 photons/fluorophore/frame yielding a localization precision of 13 ± 5 nm for DiI, and 770 ± 300 photons/fluorophore/frame yielding a localization precision of 15 ± 4 nm for CTxB-AF647.

Buffer proteins were purchased from Sigma-Aldrich and salts were purchased from Fisher Scientific. These conditions maintain a low free oxygen concentration in the buffer to minimize non-reversible fluorophore bleaching and encourage transient fluorophore blinking, as is necessary for SMLM.

Single-molecule localization

The analysis of the raw, diffraction-limited images included low-pass Gaussian filtering, multi-emitter fitting routines, median background subtraction, lateral stage drift correction, and the fitting of each isolated fluorophore images via the ImageJ plug-in ThunderSTORM[86]. ThunderSTORM provided the single fluorophore positions, localization uncertainty, and photon per fluorophores for further analysis. A threshold value 100 photons per fluorophores was used to keep only the bright localizations for further analysis. The separate channel images were overlaid via custom-made MATLAB routine via the alignment of Tetraspec nanoparticles (100 nm

diameter, Life Technologies) that were visible in all channels and maximizing the cross correlation analysis between the two channels.

Bud identification, size evaluation, and single particle tracking

The detection of buds in each color channel was performed via custom-made MATLAB program that applies a mask and detects regions with > 3x the density of the average flat surrounding background bilayer. Each bud was fitted with a 2D Gaussian function for center estimation. The size of each bud (r_{bud}) was set equal to the mean distance of all bud-associated localizations from the bud center as described previously according to Eq 21.

Single particle tracking was performed in each channel based on the criteria described previously in chapter 3, Eq 15. In brief, the analyzed single step diffusion rates were then radially averaged as a function of distance from induced membrane bud in each time point. For the 30 seconds time point, where the buds were not yet detected in pPLM, the diffusion rates were radially averaged from the expected location of the buds. In particular, based on the following time points, the expected locations of the membrane buds were mapped out and identified.

4.4 Results

4.4.1 CTxB induces membrane budding in SLBs

The reconstructed time-lapse dSTORM and pPLM images of CTxB and DiI revealed the initial protein accumulation and membrane budding processes, respectively. Within the first minute of CTxB addition to the membrane, some CTxB exhibited confinement on the flat bilayer, as demonstrated by a detectable accumulation of CTxB localizations without a significant increase in the local density of DiI localizations from pPLM (Fig. 25). After 1 min, the clusters of CTxB became co-localized with higher densities of DiI localizations as detected with pPLM. A local increase in DiI localizations obtained by pPLM represents areas in which the membrane would be

more perpendicular to the microscopy coverslip, as would be expected for membrane bud. Membrane buds formed at the locations that CTxB accumulated, demonstrating the capability of CTxB to initiate and induce nanoscale membrane bending. PLM of DiI revealed both a continued growth in the size of the buds and the formation of new buds with continued CTxB exposure.

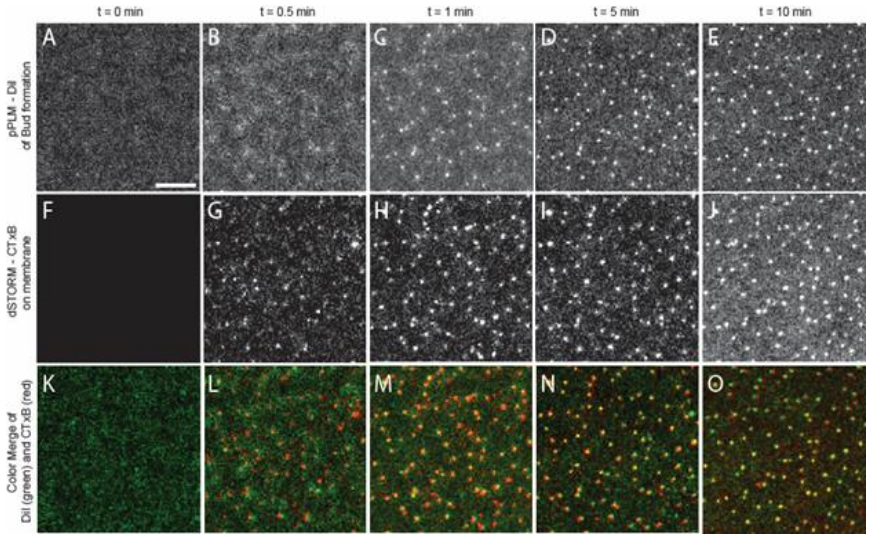

Figure 25. CTxB-induced membrane bending. Simultaneous observation of (A-E) membrane bending detected via pPLM and (F-J) CTxB clustering on the SLB detected via dSTORM reveals the CTxB-induced membrane bending. Before CTxB is added, (A) the DiI localizations by pPLM are uniform and (F) no CTxB localizations were found. Within the first 30 sec of CTxB on the SLB, (B) slight variations in the DiI localizations were present and (G) CTxB clusters formed. At later times, (C-E) the membrane buds become increasingly apparent and (H-J) CTxB became increasingly concentrated at the buds.(K-O) Color merge for the membrane (A-E) in green with CTxB (F-J) in red. Scale bar represents 200 nm.

PLM allowed earlier visualization of membrane bending initiated by CTxB than was detectable by epifluorescence microscopy. Epifluorescence microscopy revealed a laterally uniform brightness of the DiI and CTxB on the SLB for the first 20 min of CTxB incubation. The formation of CTxB accumulations and lateral DiI variations became evident with epifluorescence microscopy after 20 min in some regions of the sample. Our interpretation of the lateral variations across SLBs and variations between SLBs created by differing methods is discussed below.

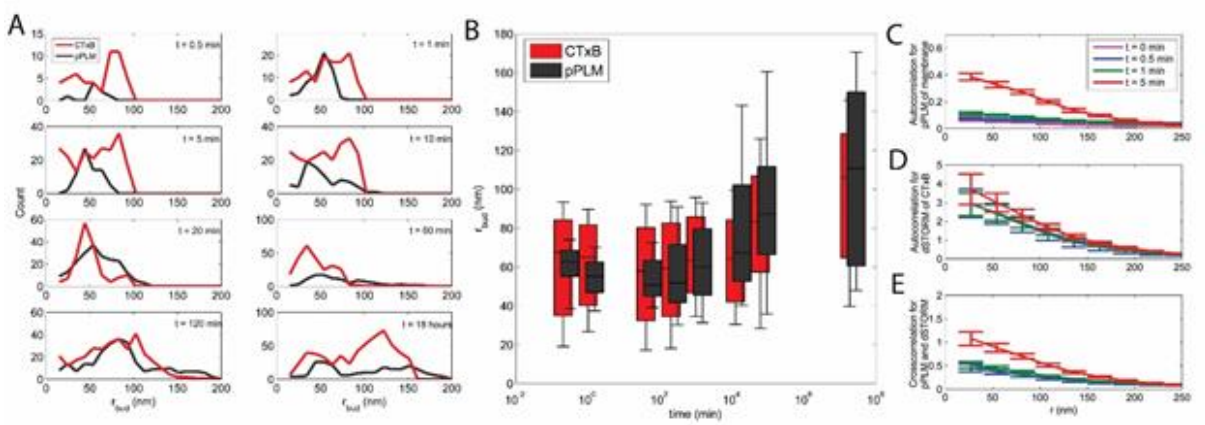

Figure 26. PLM and dSTORM reveal membrane bud size (rbud).The super-resolution capabilities of PLM and dSTORM reveal membrane bud size (rbud) versus CTxB incubation time. As some buds grow to a larger diameter or into tubules (Fig. 4), new small buds (rbud < 50 nm) continue to form and the distribution of rbud widens over time. (A) The number and size of the induced buds increase as the CTxB incubation time with the membrane increases. (B) Whisker plot for the sizes of the nanoscale buds detected in PLM and dSTORM for the membrane and CTxB, respectively. (C,D) Autocorrelation analysis of DiI and CTxB as a function of incubation time, respectively. (E) Cross-correlation analysis of DiI and CTxB as a function of time.

Regions of clustered localizations, observed in both DiI and CTxB channels, with localization density >3x that of the flat membrane were identified as membrane buds. Histograms of bud sizes versus time from the pPLM of DiI and dSTORM of CTxB show buds increasing in number and size over time (Fig. 26 A, B). Additionally, this analysis further shows that CTxB accumulations precede membrane bending since the CTxB accumulations are larger and more numerous than the DiI accumulations, as is qualitatively shown in Fig. 25. There was no clear separation of the buds into distinct stages of growth into larger structures (*i.e.*, buds vs. tubules). Some buds formed and maintained their structure, however, grew in size. While other buds quickly grew into longer membrane tubules as shown in Fig 27 (D).

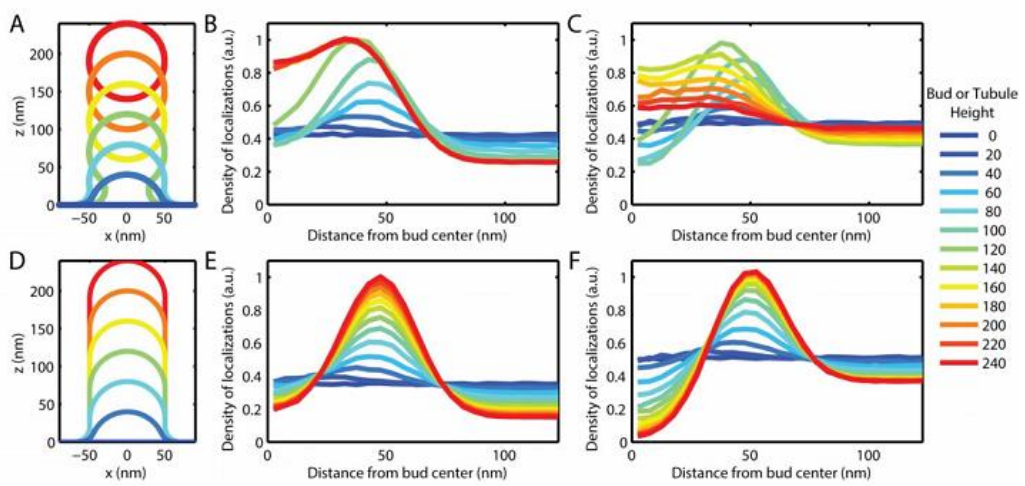

Figure 27. The simulated normalized density of localizations. The simulated normalized density of localizations versus distance from bud center for (A-C) vesiculation or (D-F) tubulation with varying heights given a bud or tubule diameter of 50 nm. Here, a uniform density of polarization-insensitive membrane-bound probes was simulated across the membrane (i.e., CTxB). The radial densities of localizations with (B, E) epifluorescence illumination or (C, F) TIRF illumination show the illumination conditions and bud height at which the ring-like structure would be observed. (C, F) The observation probability included a characteristic exponential decay length of 124 nm in TIRF illumination which increased the probability of observing a ring in the resulting reconstructed images. A ring-like density of localizations would be observed for vesiculation only when fission is near. A tubule structure would provide a ring-like structure when the bud top is >60 nm above the coverslip. Note, this simulation includes localization uncertainty (σ = 15 nm), but does not incorporate anisotropic emission, as would be the case for polarization-sensitive fluorophores (i.e., DiI).

To test whether the bud formed within a certain consistent distance from each other, auto correlation analysis was performed on the reconstructed images in each time point. The locations of the buds were extracted and a new reconstructed image of ones and zeros was created depicting only the locations of the buds centers. Auto correlation analysis was performed on such a mask with varying results. Distances between growing buds seemed to be random and there existed no apparent characteristic separation distances between the buds or tubules. Even though the separation distances varied, but the majority of the evaluated distances between buds are less than the diffraction limit (<200 nm), which also explains why such nanoscale structures haven't been detected previously. Autocorrelation analysis of bud clusters in the membrane channel and CTxB channel were plotted separately. The increased autocorrelation between membrane buds with time

is clearly shown in Fig. 26C, where membrane buds are increasing in number with time. While, in the CTxB channel a high autocorrelation between CTxB localizations exists at earlier times (t = 0.5 min), indicating the presence of CTxB clusters before the formation of membrane buds (Fig. 26D). Mapping between clustered localizations observed in CTxB and membrane channel was examined with cross correlation analysis. The increasing cross correlation analysis as function of incubation time indicates the tight mapping between clusters observed in both channels. This indicated the strong relation between buds observed in pPLM and CTxB accumulations at bud locations observed via dSTORM (Fig. 26E).

4.4.2 Some membrane buds grew into tubules

A wide distribution of bud sizes was observed with increasing bud sizes present after longer CTxB incubation times (Fig. 26 A, B). The smallest buds displayed an apparently uniform distribution of CTxB across the bud where the specific distribution of CTxB on the bud was limited by the resolution of dSTORM (*i.e.*, Fig. 24A, *black arrows*). Intermediate size buds were observed in which the DiI localizations suggest a hemispherical membrane shape greater than 100 nm radius and CTxB preferentially localized at the bud neck (Fig. 24A, *white arrow*). These large hemispherical buds showed a radially decreasing density of DiI localizations rather than a ring of DiI localizations. This effect is due to the anisotropic emission of the orientationally confined DiI within the membrane which shifts DiI apparent location toward the center of the feature [104,133]. The largest membrane bending events observed were membrane tubules with the membrane protruding away from the glass coverslip by >3 μm (Fig.28). In these membrane tubules, the ring of DiI localizations and the ring of CTxB localizations were both apparent. Such flexible CTxB rich tubules, were also apparent in epifluorescent and diffraction limited TIRF imaging.

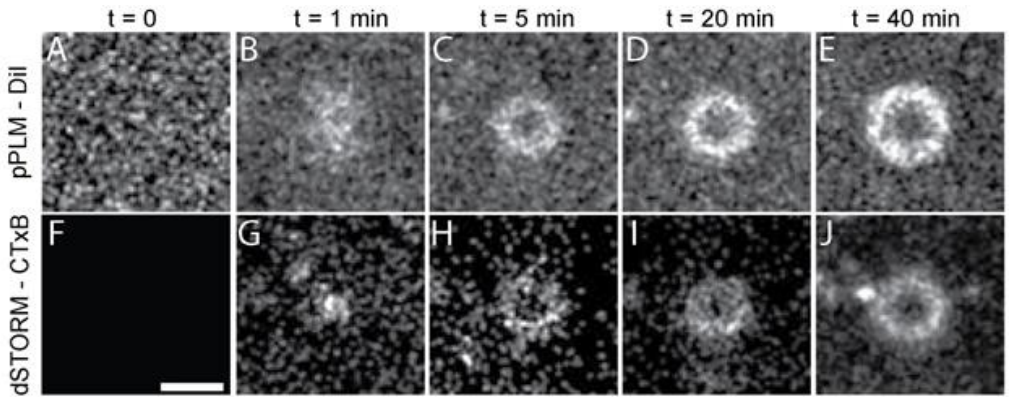

Figure 28. Some membrane buds grow into tubules. These tubules extended away from the glass coverslip. These features start with (B) a membrane bud and (G) small clusters of CTxB (rbud < 100 nm). Over time, (C) a ring of DiI localizations forms as the bud top extends farther from the coverslip and (D, E) the ring widens with an increasing tubule diameter. This membrane bending is driven by (H-J) the colocalization of CTxB at the base of the tubule where the negative Gaussian membrane curvature is present.

4.4.3 Buds vanish upon CTxB depletion

CTxB concentration is a key factor in this membrane budding and tubule formation. Typically, the concentration of CTxB on the SLB was determined by saturating the 0.3% GM1 within the membrane, and the CTxB concentration was apparently constant within 2 min of CTxB addition. However, in select experiments, the glass coverslip surrounding the patch of SLB was prepared as to encourage CTxB binding directly to the glass. In the first minutes following CTxB addition to the flat SLB, nanoscale membrane clusters were detected, as seen in all other experiments. However, the CTxB concentration was not constant over long times in this experiment. As CTxB laterally diffused on the membrane, it eventually came into close proximity with the perimeter of the SLB and the surrounding glass. Only in this experiment was CTxB observed to stick and accumulate on the glass surface (Fig. 29). This binding of CTxB to the glass caused a 93% decrease in CTxB concentration from 0.029 to 0.0018 localizations/nm^2 on the SLB. In contrast, the rate of DiI localizations showed no significant change over time. Meanwhile, the localization density of CTxB on the glass increased to 0.014 localizations/nm^2 at t = 120 min, an 8.5x increase from the density of 0.0017 localizations/nm^2 at early times (t = 10 min). As a result

of the decreasing CTxB concentration on the SLB, the number and size of the nanoscale buds decreased, as shown in both CTxB and DiI localizations (Fig. 29A, B). The buds and tubules disappeared from the membrane and the SLB returned to its original flat topography upon decreasing CTxB concentration. This phenomenon demonstrated the reversibility and the CTxB dependence of the induced membrane curvature.

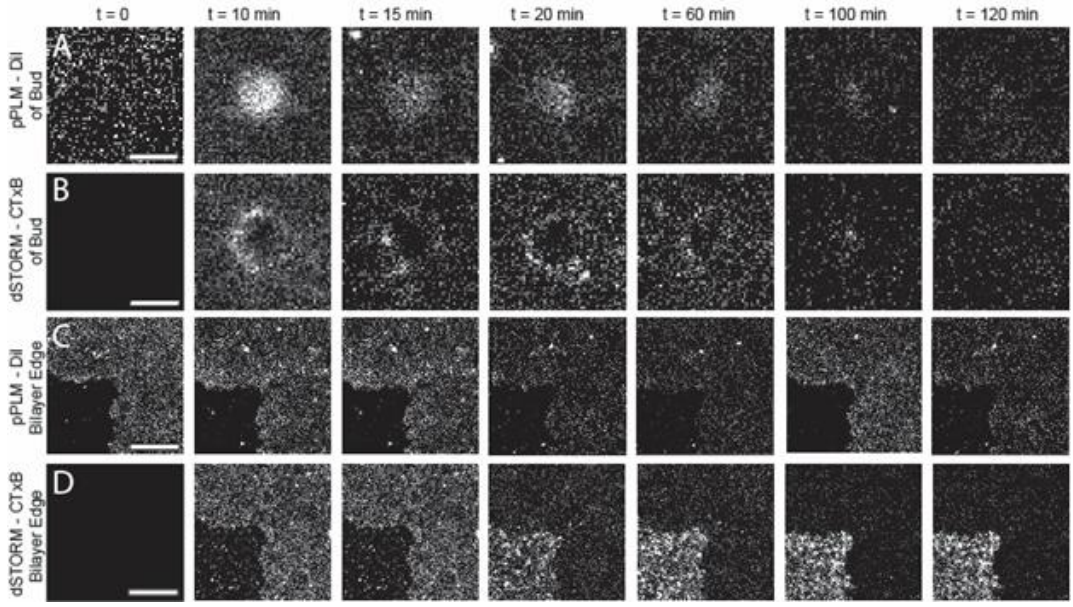

Figure 29. Budding is reversible and dependent on [CTxB]. CTxB depletion from the membrane showed that the budding process is dependent on CTxB and reversible. In this experiment, the surrounding glass coverslip was prepared as to encourage CTxB absorption and removal from the SLB. (A) The pPLM images show the membrane buds decreasing in height and diameter. (B) The dSTORM images of CTxB show a decrease of CTxB on the SLB and a uniform concentration across where the bud had been. (C) represents the time-lapse of the membrane edge surrounded by the treated glass. With time, the bilayer showed no change except for bud disappearance. (D) However, [CTxB] on the bilayer dramatically decreases at t = 15 min, while [CTxB] on glass increases. This is due to the sticking of the diffusing CTxB to the glass after close proximity. Scale bars in (A,B) represents 100 nm and in (C,D) 1 μm.

4.4.4 Single-molecule mobility varies with budding

SPT was performed on both the DiI and CTxB as a function of location within the membrane buds. Single-fluorophores that stayed '*on*' for sequential frames in the raw data collection were individually localized and linked to reveal the single-molecule mobility. The diffusive rate of DiI and CTxB on the planar SLB were measured to be (0.55 ± 0.05) $\mu m^2/s$ and

(0.14 ± 0.03) $\mu m^2/s$, respectively, with correcting for localization uncertainty in this single-step length analysis and camera blur, as described above. These diffusion rates did not vary with the duration of CTxB incubation. However, the diffusion rate did vary with distance from the center of the membrane bud (Fig. 30). Both the diffusion of DiI and CTxB demonstrated slowed diffusion rates through the *xy*-plane by (82 ± 4)% and (81 ± 9)% at the center of the membrane bud relative to the surrounding planar SLB. While a significant component of this perceived slowing of the single-molecule diffusion could be attributed to the membrane tilt, localization uncertainty (σ = 20 nm), and frame rate (50 Hz) limit, these conditions affect at most a 60% slowing on nanoscale buds, as discussed below and in the previous chapter [133]. The diffusion coefficients of DiI and CTxB were independent of the presence of buds for distances greater than 200 nm from buds centers where the membrane is flat.

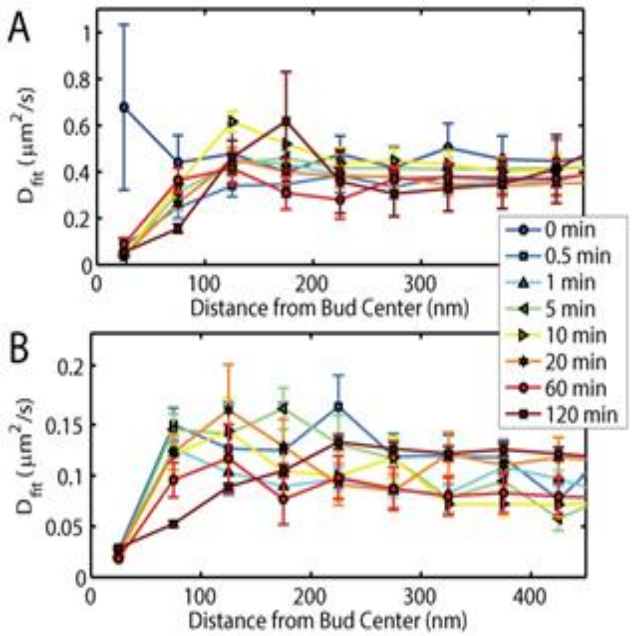

Figure 30. SPT reveal DiI and CTxB diffusion as function of distance from bud. SPT was performed on both (A) DiI and (B) CTxB as a function of position within a membrane bud. Before the CTxB is added (t = 0 min), no CTxB was located on the SLB, no membrane buds were present, and random locations were chosen for the pPLM analysis to confirm our analysis routines demonstrated no significant variation in Dfit versus distance away from the randomly chosen locations. At all later times, a significant slowing of both the DiI and CTxB diffusion is observed within 50 nm of the bud center. The error bars represent at a 95% confidence interval of the fitting

to the histograms of step lengths that were binned based on the distance from the bud center of the mean of the two linked localizations.

4.4.5 Budding occurs with varying lipid types

All budding experiments were repeated with DPhyPC replacing POPC as the primary membrane component to confirm that the particular lipids used here were not dominating this budding observation. DPhyPC and POPC are both liquid crystalline at room temperature, yet with a highly different molecular structure of their acyl chains. Indistinguishable curvature induction by CTxB was observed on SLBs formed with 99.4% DPhyPC, 0.3% DiI, and 0.3% GM1 as with 99.4% POPC, 0.3% DiI and 0.3% GM1. Further, experiments were also performed with varying membrane labels to ensure that probable lipid degradation or traces of imperfections were not the cause for such an observation. Membranes of 99.4% POPC, 0.3% GM1 and 0.3% DiO, DiI, or DiD were created and CTxB-AF647 or CTxB-AF488 was added to the bilayers. CTxB induced similar membrane budding in all cases of varying lipids, lipid dyes and CTxB labels.

4.4.6 Quantifying CTxB sorting

The buds formed by CTxB addition to planar SLBs were of sizes that varied from each other and varied with time (Fig. 26 A, B). To measure the partition coefficient of CTxB versus membrane curvature, a relatively static membrane curvature was engineered and the local CTxB concentration was observed. Only in this experiment, membrane buds were engineered by draping SLBs over nanoparticles of known sizes prior to the addition of CTxB. The ability to measure the CTxB distribution on multiple engineered buds of roughly similar known sizes, enabled averaging between buds. This data averaging provided lower noise in the experimental data and the fitting of the CTxB distribution to a predicted model of the membrane topography (Figs. 31 and 32) [133]. The radial density of CTxB observed on 25 separate nanoparticle-created membrane buds provides the experimental data (Fig. 31A). A modeled CTxB distribution on a simulated membrane topography

was *z*-projected onto the *xy*-plane, the projection was used to fit the partition coefficients for CTxB versus membrane curvature (Fig. 31B). Fitting the model to the experimental results required incorporating the single-fluorophore localization imprecision, nanoparticle-induced inaccuracy, imprecision in identifying the center of the nanoparticle, and the curvature-dependent CTxB concentration. The curvature-dependent CTxB sorting was simplified to consider just three concentrations: on the SLB ($[CTxB]_{SLB}$), over the top of the nanoparticle of r_{NP} = 70 nm ($[CTxB]_{Top}$), and on the membrane neck with one principal radius of curvature of 20 nm ($[CTxB]_{Neck}$). Many combinations of these fitting parameters yielded similar quality fit to the experimental data. The mean and standard deviation of adequate fits to the experimental data yielded $[CTxB]_{Top}/[CTxB]_{SLB} = (12 \pm 4)$ and $[CTxB]_{Neck}/[CTxB]_{SLB} = (26 \pm 11)$ (Fig. 31C).

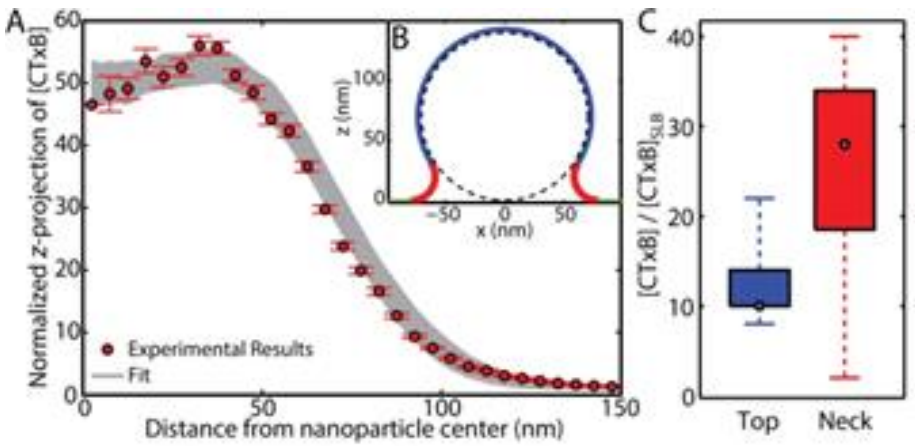

Figure 31. CTxB sorting to negative curved membrane over 70 nm. (A) Many combinations of the fitting parameters yielded quality fitting to the experimental data. (B) The membrane topography over the nanoparticle could be approximated to connect the concentration of CTxB per membrane area to the acquired z-projected data. The distribution of adequate model fits to the experimental data yielded a mean and standard deviation of CTxB concentration on the membrane top and neck relative to the planar SLB was (12 ± 4) and (26 ± 11), respectively, with the median, quartiles, and range of CTxB concentrations are shown in (C).

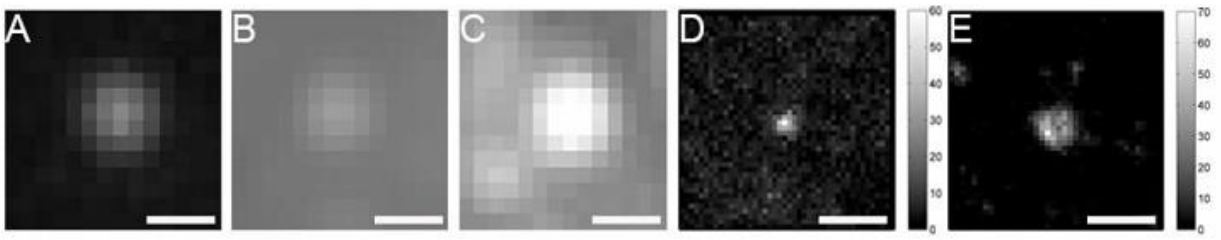

Figure 32. Images for CTxB sorting to negative curved membrane over 70 nm NPs. CTxB preferentially partitions at negative curvature located at the membrane collar over a 70 nm nanoparticle in radius. Diffraction-limited images of the (A) 70 nm radius nanoparticle imaged with λex = 488 nm, (B) pTIRF microscopy image of the membrane, the increase in brightness indicates the presence of curved membrane, and (C) CTxB-AF647 imaged with λex = 647 nm showing an increase in brightness at the curved membrane location. (D) 2D histogram plot of localizations from pPLM present increased density of localizations at membrane curvature. (E) 2D histogram plot of localizations obtained from dSTORM results for CTxB demonstrate a clustered localizations around the neck of the curved membrane with a ringlike structure. Scale bars represent (A-C) 0.5 μm and (D,E) 250 nm.

4.4.7 Membrane curvature is generated in unsupported bilayers

CTxB-induced budding was reproduced on unfused GUVs. CTxB was introduced to POPC/GM1/DiI GUVs placed on a 0.75% agarose film spin coated on a glass coverslip to prevent their rupture. Within 2 min of CTxB addition, the suspended membranes bent and formed inward tubules and vesicles. Most commonly, small vesicular invaginations coated with CTxB were observed, similar to features reported previously [119,130]. Bending away from the leaflet exposed to CTxB was observed when possible; however, bending in this analogous direction were not possible for SLBs due to the close proximity (~2 nm) of the bilayer to the glass. When unable to bend away from the CTxB, the membrane buds and tubules grew outward, toward the CTxB, demonstrating a preference for CTxB to bind to curved membranes more than planar membranes.

4.5 Discussion

PLM is a novel microscopy technique that enables imaging membrane dynamics, organization, and topography simultaneously [133]. Since PLM requires no modification to the fluorescence emission path, it is trivially coupled to other super-resolution techniques, such as

multi-color STORM and PALM. Membrane buds were detected by PLM with higher signal-to-noise than any other comparable diffraction-limited or super-resolution optical technique [133].

In this manuscript, PLM was used to reveal nanoscale membrane curvature induced by membrane-bound CTxB. PLM provided direct, super-resolution time-lapse imaging of bud initiation and growth. Each step in the progression from (1) binding of CTxB to the GM1 in a planar, quasi-one component SLB, (2) clustering of CTxB in the planar membrane, (3) inducing nanoscale membrane buds, and (4) the formation nanoscale membrane tubules protruding away from the coverslip were each detected. PLM has enabled this detection of nanoscale bud formation and the inherent membrane bending capability of CTxB that has previously gone unnoticed.

Super-resolution images of the smallest CTxB-induced membrane buds (<100 nm diameter) reveal Gaussian-like distributions of CTxB in the imaging *xy*-plane. These small membrane buds of radius (r_{bud}) equal 50 ± 9 nm displayed CTxB apparently bound upon the whole curved membrane of the bud, although the distribution of CTxB on the small bud was limited by the resolution of dSTORM. As the size of the buds increased, CTxB became most concentrated at the neck of the bud and yielded a "ring-like" structure of CTxB localizations when r_{bud} > 100 nm (Figs. 24, 31, and 32).

4.5.1 PLM distinguishes between buds and tubules

Reconstructed pPLM images were able to distinguish between membrane buds and membrane tubules by the distribution of the DiI localizations; a heterogeneous population of bud sizes was calculated at each time point (Fig. 26 A, B). The confinement of the DiI within the lipid bilayers prevents free tumbling of the fluorophore, which is critical for PLM polarization sensitivity. However, it also yields an anisotropic emission from the DiI, a systematic shift of the single-fluorophore image that is dependent on the membrane orientation and height [104]. In

particular, when the membrane is tilted 45° relative to the coverslip and 100 nm out of focus, the single-fluorophore image can be shifted by up to 50 nm. On membrane buds, the anisotropic emission effects on single DiI images systematically shifts the localizations towards the center of the bud, and reduces any ring-like distribution of DiI localizations (Figs. 24 and 25) [133].

A membrane that is tilted 0° or 90° relative to the coverslip results in no anisotropic emission effects of the DiI, i.e. no contribution to a systematic shift of the localizations of DiI. These are the dominant membrane orientations for a membrane tubule topology. Accordingly, the pPLM images of membrane tubules displayed a clear ring-like distribution (Fig. 28). Similarly, the expected localizations of CTxB bound to the outer leaflet of a tubule, should exhibit no detected localizations in the center of the tubule since CTxB cannot penetrate the membrane. Scarce localizations in the center of the tubule were presumably due to the undulating motion of the tubule, which resulted in the *z*-projection of DiI molecules within it, yielding localizations across the *xy*-plane (Fig. 33).

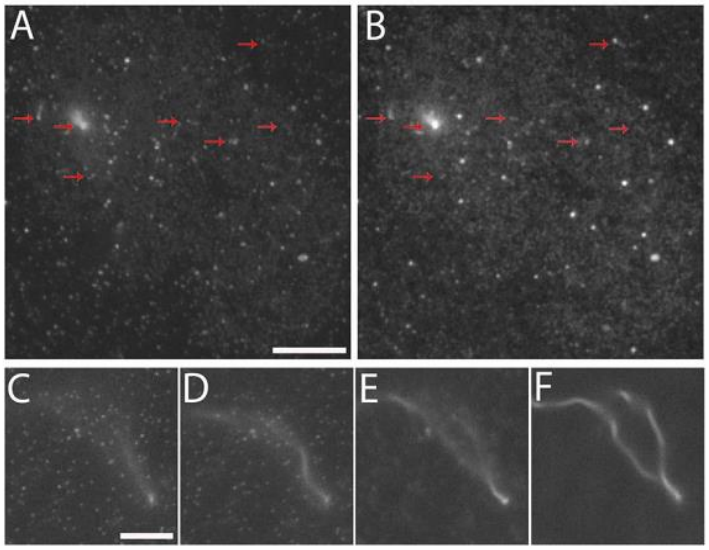

Figure 33. CTxB induces budding and tubulation on SLBs of (POPC/GM1/DiI). (A) Bilayer imaged with epifluorescence after 24 hours of incubation with CTxB. Small membrane buds indicated by regions of spots of increased brightness and long tubules indicated by red arrows appear in the membrane and (B) the CTxB channel. Some tubules extend in length to micron size as observed in (C-F). (C-F) Z-stack image of the

membrane tubule protruding from the flat supported bilayer at z = 0, 0.2, 1, and 2 μm, respectively. Scale bars represent 5μm.

Further, the probability of exciting a fluorophore with TIR illumination decreases exponentially with distance from the coverslip, which enhances the ring-like structure of acquired localizations. Brief calculations were performed to demonstrate when a ring-like structure would be observed due to the effects of an increase in membrane area and TIR illumination. The simulation incorporated these effects for both cases of membrane buds and membrane tubules of varying heights (Fig. 34). However, the dominant component in DiI localization densities is the coupling between the orientation of the fluorophore within the membrane, and the polarization of the electric field, as demonstrated previously [133].

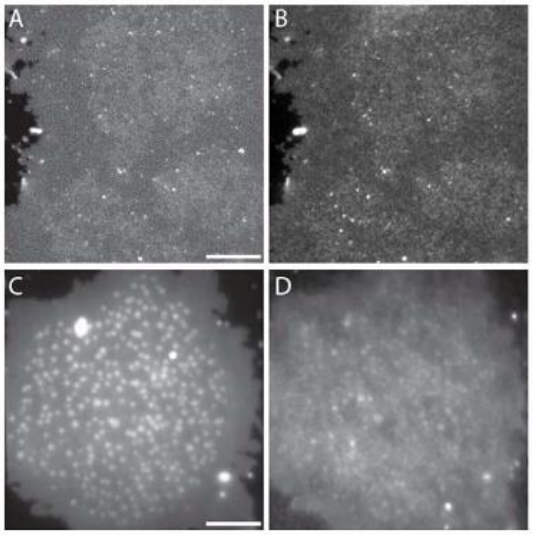

Figure 34. Diffraction-limited images of the membrane and bound CTxB. (A, C) a POPC/GM1/DiI membrane with nanoscale membrane budding sites imaged in epifluorescence and p-polarized TIRF, respectively. The buds are detected as a variation of brightness across the bilayer, however more prominent in p-polarized TIRF. (B, D) CTxB-AF647 imaged in epifluorescence for the membranes shown in (A) and (C), respectively. Scale bars represent 5μm.

4.5.2 Membrane tension affects bud formation

CTxB-induced membrane buds initially formed at the central part of the SLB patches (Fig. 35). With increasing CTxB incubation time, more buds formed at increasing distances from the

SLB patch center. The bud-forming region of the SLB typically extended >10 μm away from the center of the SLB batch, and the perimeter of the patch without bud formation was commonly 5 ± 4 μm wide. We hypothesize this observation stems from varying membrane tension across the SLB patch imparted by the GUV fusion process.

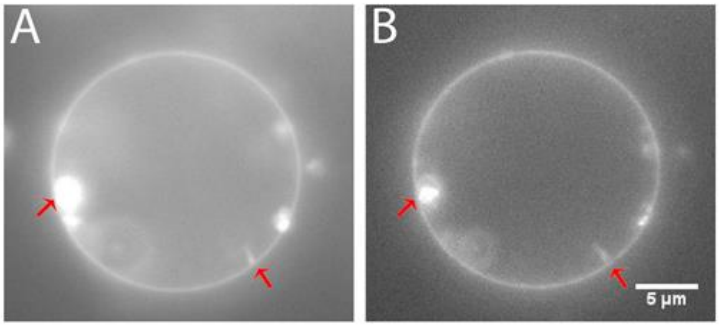

Figure 35. CTxB induces vesiculation and inward tubulation in GUVs. (A) Giant unilamellar vesicle of 99.6% POPC,0.3% GM1, and 0.3% DiI imaged with λex = 561 nm. (B) CTxB channel imaged with λex = 647 nm. Red arrows indicate regions of induced curvature and inward invaginations by CTxB.

At the location of GUV fusion to the coverslip and near the center of the SLB patch, there was initially a high concentration of excess membrane from a portion of the GUV or nested GUVs that did not fully fuse to the glass coverslip. These unfused vesicles were removed with vigorous washing to yield an apparently uniform SLB. Membrane buds were most likely to form in the center of the SLB patch, close where the unfused vesicles were, rather than close to the edge of the SLB and the exposed glass coverslip (Fig. 5).

Variations in SLB tension could occur during two distinct stages of SLB creation by GUV fusion. The first stage would consist of the initial GUV-glass contact, before or immediately after the GUV has ruptured. The rupture of the GUV may have exposed a loose or floppy bilayer to the glass coverslip, and initiated a membrane-glass contact that trapped nanoscale undulations and decreased lateral tension in the SLB. Over time, the bilayer would spread across the glass with Marangoni flow, as encouraged by the membrane-glass adhesion, and yielded higher lateral

membrane tension, similar to as seen previously [138]. Accordingly, the center of each SLB patch would have a lower membrane tension and encourage bud and tubule formation, as compared to the perimeter of the patch, consistent with our observations.

The rate of GUV fusion was controlled by the duration of the plasma cleaning and the occasional presence of a coverslip cushion. When no GUV fusion was wanted, a thin film of agarose was used to minimize the membrane-substrate adhesion (Fig. 35). In the absence of membrane cushion, and under long exposures of plasma cleaning (>2 min), the membrane-substrate adhesion was too strong for the creation of a continuous SLB patch. In this scenario, the GUVs rupture was too vigorous. Diffraction-limited holes in the SLB were observed, and a slower fluorescence recovery times were measured via fluorescence recovery after photobleaching (FRAP). In these cases, when the membrane-substrate adhesion was too strong, no curvature induction by CTxB was observed.

4.5.3 Utilizing a supported lipid bilayer to visualize membrane budding events

Conventional biologically relevant and mimicking systems are giant plasma membrane vesicle (GPMV) directly extracted from cells, or synthetic giant unilamellar vesicles (GUVs). We have demonstrated the inward budding observed on GUVs similar to previously reported phenomena detected on cells. Membrane bending usually occurs toward the direction of the medium with lower CTxB concentration. As also observed for suspended membranes independent of the substrate[139]. However, the choice of using a supported lipid bilayer rather than such substrate-independent systems emerges from the challenges posed by the free-floating bilayer systems. First, it would be challenging to image the suspended membranes in TIRF due to their existence beyond the TIRF range. This might be overcome by utilizing multiple bilayer system, where the membrane cushion is basically a non-fluorescent bilayer where the bilayer of interest

exists within the TIRF range (few or tens of nanometers from the glass coverslip). On the other hand, a symmetric toxin binding to the membrane might occur. The toxin will be able to leak under the free standing bilayer and bind to both leaflets, losing the asymmetric binding state of CTxB on SLBs, and reducing the possibility of inducing membrane curvature. Further, suspended bilayers provide faster dynamics of large membrane structures. The absent membrane substrate interaction may cause the bud structures, if formed, to diffuse freely, reducing their visibility with PLM or any SMLM techniques. Dynamic curvature in unsupported bilayer present an imaging challenge in PLM and super resolution studies.

Although the limitations posed by SLBs are considerable, their widespread use for diverse biophysical experiments is a testament to their value (*e.g.*, see Ref. [140] and the >1700 papers that cite it). Synthetic SLBs in this case enabled testing the effects of CTxB on the membrane without the complexity of the cell. While the interaction between CTxB and SLBs is different than the interaction between CTxB and cell membranes in some key ways, the CTxB -SLB interaction is important in several aspects. The studies CTxB-SLB interaction is important for the understanding of diverse biophysical applications of SLBs. Further, this interaction demonstrate the inherent membrane bending effects of CTxB that contribute to its physiological behavior, in yet-to-be-revealed ways. For example, curvature induction by CTxB on SLB may explain the previously reported phenomena of molecular-scale pinning sites, confined diffusion, lipid-phase sorting, and clustering of CTxB on SLBs [141–145]. In complex cells membranes, CTxB is a traditional marker of ordered, cholesterol and sphingomyelin-rich membrane regions, often without consideration of the inherent membrane bending capabilities of CTxB [146–149]. In both synthetic and living systems, it is necessary to consider the capabilities of CTxB to cause membrane curvature, as shown in this study, without lipid phase separation and independent of caveolin for accurate data interpretation.

4.5.4 Membrane budding slows CTxB and DiI diffusion

The diffusion of CTxB on membranes has been reported with widely varying rates, including rates that range from 0.04 to 2.44 $\mu m^2/s$ within a single cell, and spatially confined in regions that are 100 to 1800 nm diameter [150,151]. Even in the absence of coexisting lipid phases such as > 99% DOPC model membranes, CTxB exhibited multiple diffusion populations, with one population of $D = (0.18 \pm 0.04)\ \mu m^2/s$ and the second population of $D = (0.06 \pm 0.02)\ \mu m^2/s$ with transient confinement in regions as small as 20 nm radii [125,126]. These prior measurements had no means of detecting changes to membrane topography or correlating topography with mobility, which is the focus of this study. The diffusion measurements reported here are consistent with both the previously reported diffusion rates and confinement sizes. In this study, the diffusion rates are presented while demonstrating local membrane curvature as a mechanism for varying CTxB behavior in a single membrane. This curvature-dependent analysis of CTxB diffusion and accumulation has the potential to explain prior measurements of both distinct populations of CTxB diffusion rates (Fig. 30) and the inter-membrane molecular sorting that is independent of lipid phase.

The mechanisms by which membrane bending slows CTxB and DiI diffusion are most likely to be the result of molecular crowding, local phase separation, and/or a curvature-dependent membrane viscosity. If CTxB becomes dense enough in a local region of the bilayer, it would be expected that this crowding would slow the diffusion of CTxB and/or lipids (*i.e.*, DiI) within the membrane. Additionally, it is feasible that the local concentration of GM1 was increased sufficiently as to drive the local lipid environment into a more ordered state, and cause an increase in the effective membrane viscosity, as would be expected for more ordered lipid environment [152–154]. It is not likely that the 99.4 mol% POPC bilayer would have significant phase separation, but

CTxB-encouraged GM1 accumulations are possible. Further, a change in the lipid head groups dynamics and orientation in the vicinity of the toxin may also contribute to changes of the lipids diffusion rates [155].

Finally, it is feasible that the membrane bending itself affects the local effective lipid viscosity and the free diffusion of lipids and proteins through the membrane buds. This effect was observed when membrane curvature was engineered by draping SLBs over nanoparticles and the lipid diffusion was measured with SPT [101,133] but not when measured with FRAP [156], as expected [90]. If the effective membrane viscosity changes upon membrane bending, then the diffusion of the DiI molecules in both leaflets could be affected, regardless of the supporting substrate or local CTxB concentrations.

4.5.5 Bud formation didn't require lipid phase separation

SLBs of >99% POPC or DPhyPC were used for these studies due to their strongly disordered acyl tails and the minimal possibility of phase separation with 0.3% GM1 and 0.3% DiI included. The liquid-to-gel transition temperatures for POPC and DPhyPC are -2°C and <-120°C, respectively. To minimize the possibility of a spontaneous GM1 clustering in the bilayers, a low GM1 concentration was used here (0.3 mol%); however, GM1-rich gel phases has been observed in otherwise fluid bilayers[157]. For a binary system of POPC and GM1, a GM1 rich gel phase is expected to form at low temperatures and high GM1 concentrations (> 1% GM1). Prior studies that reported sorting of CTxB to the neck of membrane buds required a ternary mixture of cholesterol, sphingomyelin, and POPC to observe CTxB sorting[97]. CTxB sorting in that case might have been driven by nanoscale lipid phase separation, or by the pre-existing membrane curvature. However, curvature in these prior studies was of a significantly larger radius of curvature (μm scale) such that the curvature-dependent sorting was presumably weaker than that observed here

(nm scale). Even though lipid phase separation is not likely in these experiments, it is feasible that nanodomains of GM1 were formed and were stabilized by the multivalent CTxB binding, as further discussed below.

4.5.6 Bud formation is energetically feasible

The spontaneous bud nucleation and tubulation are controlled by the membrane bending rigidity, density of CTxB, and the adhesion of the SLB with the substrate. For bud formation to be spontaneous, the energy released by CTxB-GM1 binding must be greater than the energy put into bending the membrane and separating the membrane from the glass. The total energetic cost of bending the membrane (E_{Bend}) was estimated via Helfrich energy model[158] for at 50 nm top radius of curvature hemispherical bud with a 20 nm radius of curvature collar smoothly connecting the bud to the surrounding planar SLB (Fig. 24B), such that

$$E_{Bend} = \int (\kappa(H - H_0)^2 + \bar{\kappa}K)dA \qquad \text{(Eq. 27)}$$

This incorporates the membrane bending rigidity (κ), membrane Gaussian curvature modulus ($\bar{\kappa}$), the mean local membrane curvature (H), the local Gaussian curvature (K), the intrinsic membrane curvature ($H_0 \approx 0$), and the area of the bud (A). The bending rigidity of a POPC membrane in TRIS buffer at T = 22°C is $\kappa = (12.9 \pm 0.4) \times 10^{-20}$ J $\approx \bar{\kappa}$ [159,160]. The energy required to bend the membrane into the presumed configuration was calculated analytically $E_{Bend} = (5 \pm 1) \times 10^{-18}$ J.

The adhesion energy of the bilayer to the glass substrate is given by $w = 10^{-8}$ J/m^2 [161]. A bottom radius of 67 nm yields 1.4×10^4 nm^2 of the SLB to be separated from the substrate, the energy cost of lifting the membrane off the substrate ($E_{Adhesion}$) equals $(1.4 \pm 1) \times 10^{-22}$ J, which happens to be smaller than $k_BT = 4 \times 10^{-21}$ J.

The intrinsic free energy released per CTxB binding to the GM1 in the SLB is equal to -67 ± 2 kJ/mol [162]. The area of the CTxB pentamer is equal to 106 nm^2 and there would be space for 120 CTxB to bind to just the neck region of this membrane bud [119,132]. Accordingly, the energy change upon CTxB accumulating around the neck of this nanoscale bud (E_{Bind}) is (-1.3 ± 0.5) x 10^{-17} J.

In comparing these three energetic components, we found $| E_{Bind} | > | E_{Bend} + E_{Adhesion} |$. In conclusion, there is ample energy from CTxB binding to drive nanoscale bud formation spontaneously. However, further discussion is warranted to consider how much of this energy of CTxB binding is expected to drive membrane bending and the preferred radius of curvature for a membrane under CTxB.

4.5.7 The forces that drive budding

A complex interplay of factors could contribute to the budding process such as CTxB steric crowding [80]; CTxB insertion into the membrane [163]; CTxB-GM1 cross-linking; the positive intrinsic curvature of GM1 [164]; GM1 clustering via lipid phase separation [165]; the extended long acyl chain of GM1 causing wedging in the opposing bilayer leaflet [125], and the asymmetric GM1 concentrations in the bilayer leaflets. The steric pressure between the crowded CTxB within a nanoscale area could inherently encourage membrane bending if there was an attractive force between the GM1 to counter the steric repulsion between CTxB and provide a local membrane torque [80]. An attraction between GM1 is plausible considering the strong liquid-ordered phase preference of GM1 in ternary lipid mixtures, the affinity of GM1 to self-cluster [157,163,165], and the possibility of GM1 unbound to CTxB further accumulating around the clusters of CTxB-GM1. A leaflet asymmetry in GM1-GM1 clustering and CTxB binding could encourage a mismatch of composition between the leaflets and encourage curvature.

Further, the molecular shape of CTxB itself is likely to encourage a negative membrane curvature. The molecular shape of CTxB and Shiga toxin both have glycolipid binding pockets that are elevated above from the bottom of the folded protein, the toxin-lipid binding encourages a penetration of the protein into the bilayer and/or a local wrapping of the membrane around the protein, as has been most explicitly shown for Shiga toxin [163]. Thus, as the membrane is pulled to wrap around the toxin, a bending force is created by the toxin with its peripheral GM1 binding pockets. A wrapping of the membrane around the toxin would encourage a negative membrane curvature. In a suspended membrane or a plasma membrane, this typically manifests as the formation of a membrane invagination, where CTxB is located on the inner leaflet with both principal planes being negative curved. On a SLB, where vesiculation of the CTxB is inhibited by the substrate, the local wrapping of the membrane around the toxin was sufficiently preferable to drive the membrane to bud away from the coverslip. In this case, CTxB primarily partitioned on the bud neck with one principal plane of negative curvature. While this budding towards the CTxB is not observed on plasma membranes, these experiments demonstrate the nanoscale effects of CTxB on SLBs, and the curvature induction capabilities of CTxB, broadly. The importance of the spontaneous curvature generation by CTxB is likely essential for its trafficking through the cell. Similarly, the complex curvature-dependent sorting profile of CTxB is likely impactful in complex organelle membrane topographies.

Finally, the multivalent binding of CTxB may be critical for the preference of CTxB to bind to negatively curved membranes, such as regions of negative Gaussian curvature over planar membranes. CTxB is typically saturated by binding to five GM1 molecules simultaneously; however, the number of bound GM1 molecules directly affects the orientation of CTxB on the membrane [155,166]; CTxB is parallel to the membrane when bound to five GM1 but tilted when

bound to only 3 GM1 [155]. The rotational asymmetry of the occupied GM1 binding pockets on the CTxB may result in a shifted CTxB preference to bind to one dimension of negative curvature and have a minimal preference for the membrane curvature in the other principal curvature dimension. Accordingly, if introduced upon a negatively curved membrane (*i.e.*, inside of a vesicle), a CTxB bound to 3 GM1 would be stable at any rotation. However, if introduced upon a negative Gaussian curvature membrane (*i.e.*, bud neck), the CTxB bound to 3 GM1s would require it to be rotated. This rotation allows the GM1s to be spaced along the dimension of negative curvature, limiting the degrees of freedom for CTxB orientation while maintaining membrane wrapping around toxin [153,155,166]. The number of GM1 bound to the CTxB might not only affect its curvature preference, but also its diffusion rate. This might be the reason for the observed variation in the diffusion rates reported here on the flat membrane, and the importance of valency in lipid phase separation [167]. Unfortunately, these explanations for the curvature induction mechanisms by CTxB are highly speculative at this time. Further experimentation to clarify the mechanisms of CTxB-induced membrane curvature and CTxB valency are warranted.

4.5.8 Membrane curvature induced CTxB sorting

Studies regarding CTxB location at certain membrane curvature gradients have shown that CTxB preferentially localizes at negatively curved membrane regions[96] and at the neck of micron-scale engineered membrane buds[97]. Here, CTxB were observed to initially cluster and spontaneously form small membrane buds (Fig. 24A, *black arrows*). As the buds grew in size, the accumulation of CTxB around the perimeter of larger membrane protrusions became increasingly apparent (Fig. 24A, *white arrow*). CTxB also localized at similar membrane geometry on bilayer draped over a 70 nm radius nanoparticle (Figs. 31 and 32). Thus, the ring-like shape of localizations obtained for CTxB demonstrates the preferential location of CTxB at the neck of the

curvature. This observation falls in agreement with previous reports that observed the accumulation of CTxB at the neck of lithographically patterned spherical membrane protrusions with 25 μm diameter that was dependent on coexisting liquid lipid phases[97]. By observing 20x smaller curvatures here, the curvature-based sorting forces were presumably larger and not requiring assistance by lipid phase separation for CTxB sorting to occur.

In some cases CTxB induced membrane ridges in which CTxB preferentially localize at the negative curvature regions (Fig. 36).

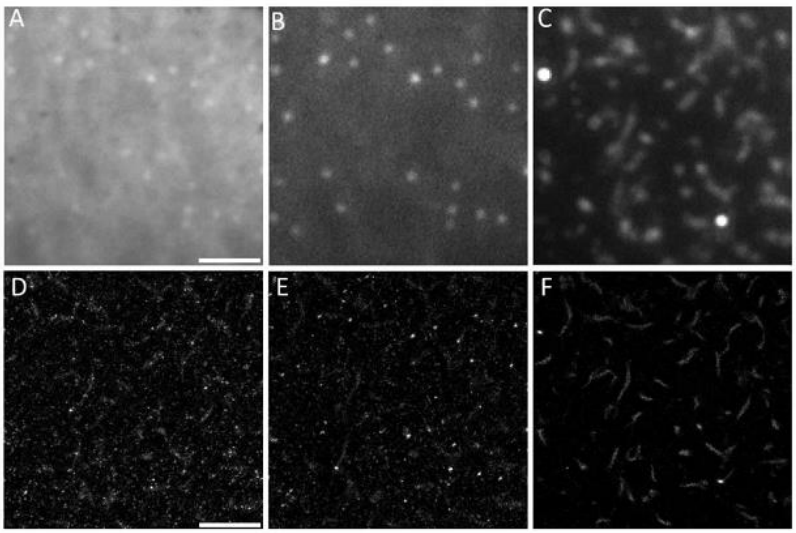

Figure 36. CTxB induces membrane ridges. CTxB preferentially partitioned at these nanoscale membrane structures. (A-C) Diffraction-limited images of the membrane in sTIRFM, pTIRFM, and the bound CTxB in CTxB channel, respectively. (D, E) Super-resolution reconstructed images plotted as 2D histograms of localizations of the membrane obtained in sPLM, and pPLM, respectively. (F) dSTORM reconstructed image of CTxB-AF647 shows high localization density of CTxB at the induced membrane ridge. The nanoscale size of such membrane structures prohibited their observations in diffracted limited imaging; however, clearly detected in super resolution. Further, CTxB preferentially partitioned to one dimension negative curvature regions observed in these ridges and on wavy glass substrates (11). Only ~4% of 48 samples exhibited nanoscale ridges-induced by CTxB in addition to nanoscale membrane budding. Scale bars in (A-C), and (D-E) represent 4 and 2 μm, respectively.

4.6 Conclusions

PLM has enabled the direct observation of CTxB and membrane dynamics to reveal CTxB-induced membrane budding on SLBs. In this manuscript, PLM was used to reveal simultaneous

multicolor super-resolution images of CTxB and the induced bud growth on a supported, quasi-one component lipid bilayers. Our data provide context to prior studies with CTxB that observed time-dependent diffusion rates and diverse internalization mechanisms. We demonstrated that the molecular mobility of CTxB and DiI are affected by the nanoscale membrane structures induced by CTxB. On planar SLBs, the diffusion rates of DiI and CTxB are in agreement with previous reports on cells and synthetic membranes. However, the diffusion coefficients at the center of the induced buds are (82 ± 4)% and (81 ± 9)% less than that on the planar membranes for DiI and CTxB, respectively. DiI and CTxB underwent transient confinement in regions that later appeared to be nanoscale protrusions as small as 30 nm radius. Our studies demonstrated the budding process was reversible and dependent on CTxB concentration. PLM will aid in providing new information for previously untestable nanoscale processes coupled with changes in membrane topography. We propose a mechanism of CTxB trafficking in cells dependent on the spontaneous membrane curvature-induction and curvature-based sorting by CTxB. In this case, CTxB prefer negative Gaussian curvature over planar membranes. We will explore the effects of changing the GM1 structure and membrane composition on the budding process, as well as using mutant, monovalent CTxB that binds to one GM1[167]. Biological functions of the cell are dictated by the sorting, mobility, and organization of its constituents that affect the structure of the cell membrane facilitate diverse essential membrane processes.

CHAPTER 5 CROSS LINKING EFFECTS ON MEMBRANE GEOMETRY

5.1 Introduction

Certain cell functions and biological components are affected by cross-linking of its constituents. For instance, crosslinking collagen based films affects the modes of interaction with the residing myoblasts[168]. In this case crosslinking affects the physical and surface propertied of the material and eventually cell function. In other cases, crosslinking is required to determine the modes of function of a certain toxin[167]. As previously mentioned, CTxB binds to five GM1 molecules, the crosslinking of CTxB with its membrane anchor determines the phase preference of the complex and subsequently affects the internalization process of the toxin. In addition, large micron scale stabilization of lipid phases is aided by crosslinking which also affects the miscibility temperature of the membrane. Lipid phase separation can be induced by temperature change or even by membrane components crosslinking[116]. Crosslinking is an indispensable mechanism adopted in various cellular processes[168–170]. Clustering of membrane components or oligomerization also drive changes in membrane topology as demonstrated in chapter 3 in which CTxB clustering induced nanoscale membrane budding[106,171]. In other cases, clustering is required for an immunological response[172,173] or allergic reaction[93]. A nanoscale crosslinking or clustering could lead to a micron scale reorganization of lipids, lipid phases, or modification in membrane structure such as budding and tubulation. For instance, crosslinking and oligomerization of calcium−phosphatidylinositol phosphate 2 (PIP_2) initiate signaling, and leads to a cascade of events for cell response[174]. Yet, the relation between membrane components crosslinking and the membrane structural alteration and organization is an ongoing investigation. Aided with PLM and the ability to detect nanoscale membrane curvature, we investigated the effects of crosslinking biotinylated lipids with streptavidin and study its effects on the membrane topology.

5.2 Biotin-Streptavidin binding effects on SLBs

To test whether inducing nanoscale membrane curvature is dependent on CTxB structure and valency, we substituted CTxB-GM1 system by a streptavidin-biotinylated lipids system which will be the focus of this chapter. The effects of crosslinking five biotinylated lipids with streptavidin on the membrane was then imaged with PLM. Streptavidin is a pentameric molecule that binds to five biotinylated lipids in the membrane. The high dissociation constant of the streptavidin-biotin complex K_D of 10^{-13}-10^{-15} M represent the low probability of detachment once bound together[175]. Nanoscale crosslinking induces changes in membrane structure and/or phase separation which also depends on the number of crosslinked lipids. Toward this aim, we simultaneously measured changes in membrane topology with the addition of fluorescently labeled streptavidin via super resolution microscopy. We report the observation of membrane phase induction in the studied bilayers with fluorescently labelled streptavidin. The detected micron scale induced lipid phase excluded DiI dye which is a L_d marker while being enriched with streptavidin. However, no structural reorganization was detected in the case of non-fluorescent streptavidin. In sum, these studies represent a key component for nanoscale membrane curvature induction. Crosslinking might not be the only factor that drove membrane bending in the case of CTxB-induced membrane budding due to the absence of induced curvature in the case of biotin-streptavidin binding. In that case, budding also occurred due to the inherent shape of CTxB which possess an intrinsic curvature within its structure.

5.3 Materials and Methods

Chemicals utilized

Giant unilamellar vesicles (GUVs) of primarily POPC with 0.3 mol% 1,2-dioleoyl-*sn*-glycero-3-phosphoethanolamine-N-(cap biotinyl) (sodium salt) (Avanti Polar Lipids, Inc.), and 0.3

mol% 1,1'-didodecyl-3,3,3',3'-tetramethylindocarbocyanine perchlorate (DiI, Life Technologies). Streptavidin, Alexa Fluor™ 647 conjugate (Invitrogen).

Sample preparation and imaging procedure

Imaging optics, imaging procedure, imaging buffer, and single molecule localization are similar to the ones listed in chapter 2.

5.4 Results

5.4.1 Fluorescently labelled streptavidin induced phase separation

The acquired time-lapse images of streptavidin-AF647 and DiI revealed the initial streptavidin clustering and phase induction process, respectively. Within the first 5 minutes, streptavidin accumulation on the membrane was observed as increased signal brightness within nanoscale regions that quickly grew into micron scale regions. Shortly after the streptavidin clustering, micron sized islands of DiI depletion appeared as regions of lower DiI brightness that coincide in location and size with streptavidin clusters (Fig. 37).

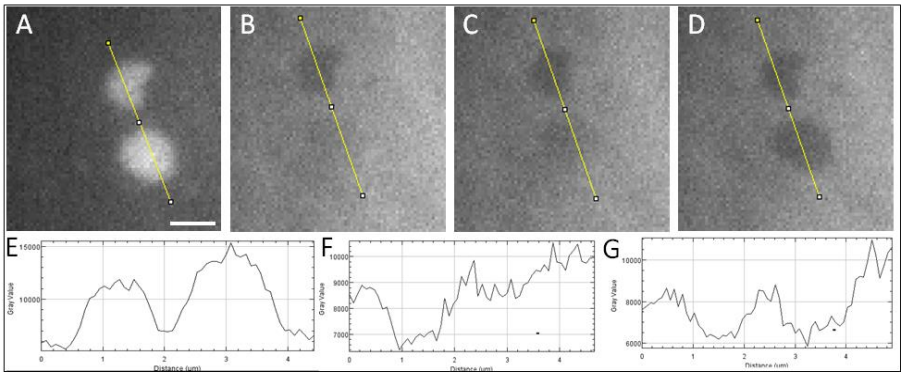

Figure 37. Time lapse of phase induction on a POPC/DiI/biotin-DPPE SLB. Enrichment of streptavidin-AF647 (A) onto a region on the membrane occur prior to DiI depletion. (B-D) time lapse of the membrane showing region of decreasing DiI brightness at the same location of streptavidin enrichment. (E,F,G) Brightness histogram of pixels within the yellow lines indicated in (A,B,D). Scale bar represents 4 μm.

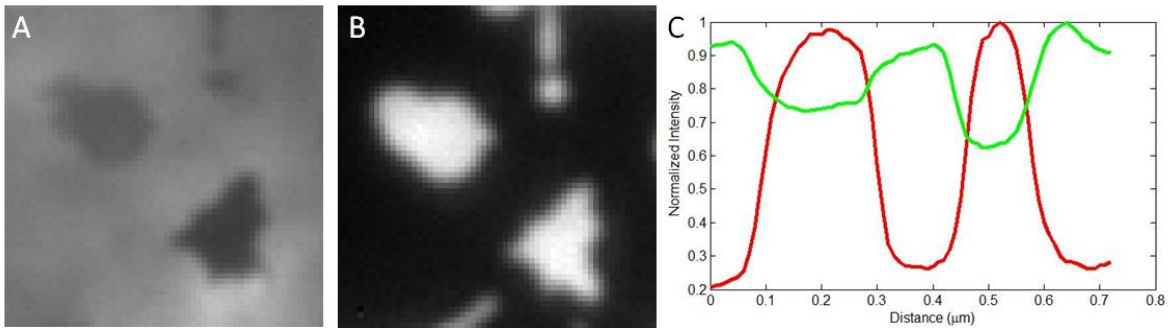

Figure 38. Phase coexistence induced by streptavidin-AF647 addition. Regions of co-existing phases indicated by variation of DiI brightness in pTIRF image of the membrane observed in (A). (B) streptavidin-AF647 imaged in 647 nm channel. (C) Normalized histograms of brightnesses of the same region in the membrane (green line) and streptavidin (red) channel.

5.4.2 Biotin-streptavidin binding did not affect membrane structure

Repeating the experiments while utilizing a non-fluorescent streptavidin resulted in a uniform distribution of DiI localizations and no phase induction. The brightness of the DiI labelled bilayer before the addition of streptavidin was similar in uniformity as after addition up to an hour of observation time. Similar results were observed with biotin concentrations of 0.3, 0.6, 1, 3, and 10% (Fig. 39).

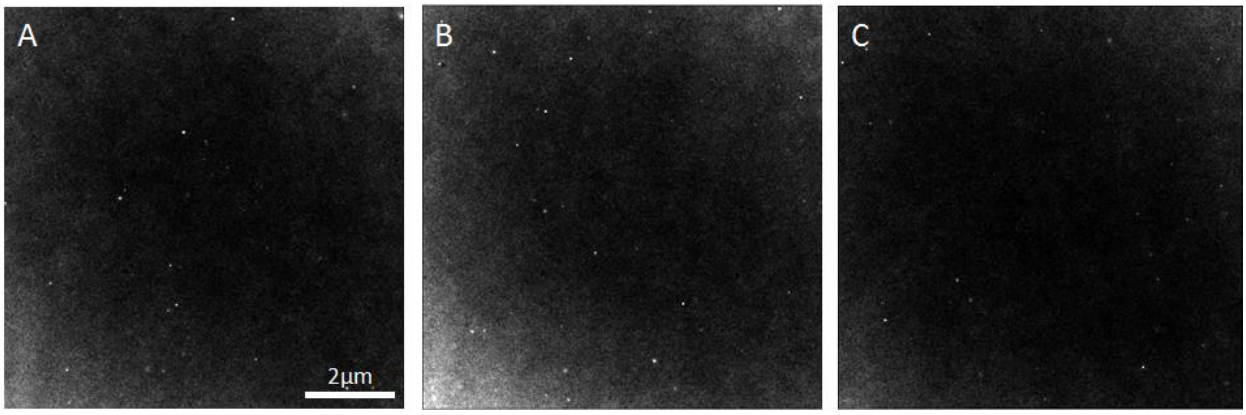

Figure 39. Addition of non-fluorescent streptavidin didn't induce curvature. Even with increasing biotin concentration to 3%, no membrane topology change was detected. Super resolution pPLM images of a POPC/DiI membrane with varying biotin concentration of (A) 0.3, (B) 1, and (C) 3% acquired after 90 minutes of streptavidin addition of 0.25 ug/mL.The uniform localization density indicated flat membrane structure with no induced curvature.

5.5 Discussion

5.5.1 Crosslinking effects on phase dynamics

DiI depletion from streptavidin rich regions occurred only in the case of a fluorescently labelled streptavidin, while in the case of a non-fluorescent streptavidin no such phase induction was observed. Previous reports have detected biotin-streptavidin complex preferential partitioning and sorting onto L_o phase in a phase separated GUV with a ternary mixture of lipids[176–178]. Further, nanoscale compositional change induced by crosslinking could trigger large scale phase separation[116,179]. Previous reports have also showed that biotin-streptavidin complexes induce perturbation and drove lipid phase separation upon crosslinking[180]. This might explain the shift in the phase dynamics observed here where biotin-streptavidin binding have induced local phase separation (L_o and L_d phases), where regions with DiI depletion (which is a L_d marker) exhibit enrichment with streptavidin. Further, in the reported study we have utilized quasi-single component bilayers (> 99% POPC lipid) which decreases the possibility of detecting lipid phases. However, it has been shown that traces of membrane additives might induce subtle perturbations and aid in phase separation processes[181]. Presented experiments have also been reproduced by replacing POPC with DOPC or DPhyPC, and replacing DiI with DiO to confirm that the detected observation is independent on the lipid or dye used.

Variation of DiI brightness was recorded where some regions demonstrated curved phases in pTIRFM while darker regions demonstrated no curvature. Only Lo regions were curved while the gel phase regions showed no increased brightness at the rim in pTIRFM (Fig. 40).

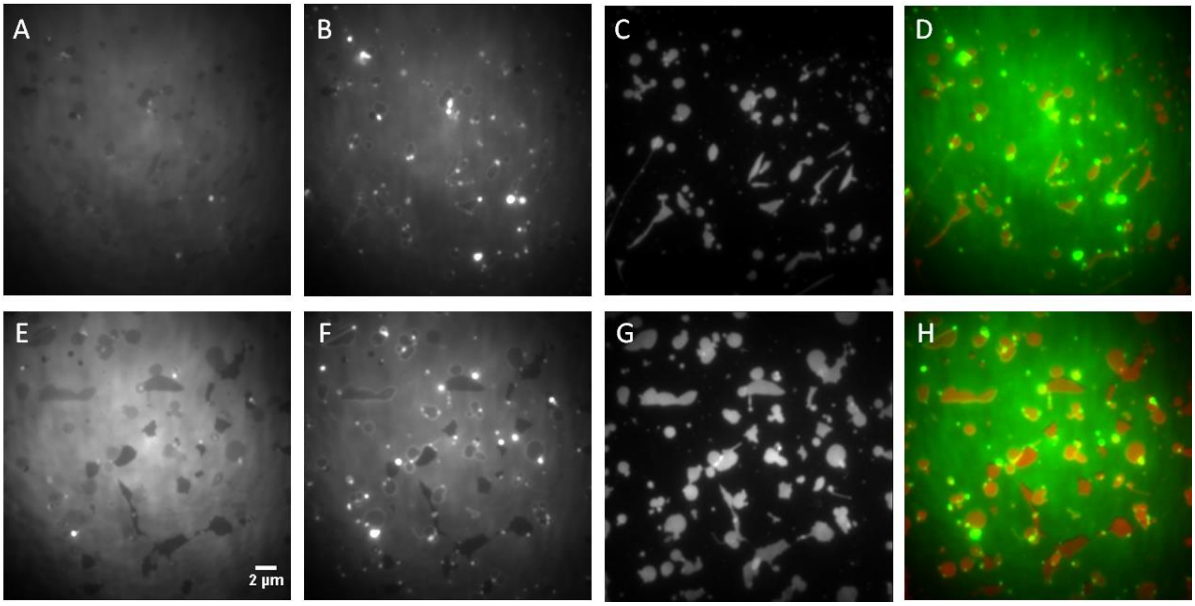

Figure 40. Curved coexisting phases induced by streptavidin-AF647 addition. Regions of co-existing phases of Ld (light grey), Lo (dark grey), and gel (darkest grey) phases observed in sPLM imaging of the membrane (A,E). The increased brightness around the induced Lo phase, detected by pTIRF in (B, F) indicates curvature. (C, G) Regions of enrichment of streptavidin-AF647. (D, H) Color merge of the membrane (green) and streptavidin-AF647 (red).

5.5.2 Fluorophore clusters effect on the membrane

The detected phenomena of phase induction might be strictly dependent on the fluorescent label. Alexa fluorophores are knows to aggregate and cluster together, which modifies its interaction with the membrane[182,183]. Several techniques such as bath sonication are often used to break down aggregates; however, this might also lead to a misleading analysis. Fluorescent signal detected might indicate the location of the streptavidin labelled molecule, or it might indicate the location of the water soluble Alexa fluorophore unbound to streptavidin. Further, Alexa fluorophore tendency to aggregate might lead to the formation of a larger cluster of multiple bound streptavidin molecules, which covers a larger area upon interacting with the membrane and binds to more biotin molecules. This large scale crosslinking cluster might drive lipid phase separation and alter the effect of streptavidin-biotin binding on the membrane. The size and number of

crosslinked molecules are critical for certain processes. As mentioned previously, for instance, mutant monovalent CTxB have a different phase partitioning than a pentamer CTxB[167].

5.5.3 Streptavidin crystals alter lipid phase lying underneath

Moreover, streptavidin is known to self-associate and form 2D crystals on GUV surfaces and Langmuir films[177,178,184]. The clustering and crystallization of streptavidin might create a larger cluster that, upon binding to the biotin within the membrane, alters the membrane dynamics and phase behavior. In such cases, recovery after photobleaching was not observed for labelled streptavidin. Further, such crystallization might dictate the lipid phase underneath, induce surface crowding, and inhibit mobility and domain coalescence within the membrane.

Three populations of DiI brightness have been detected on the membrane shortly after the addition of streptavidin (~10 minutes after streptavidin addition). In such cases the portioning coefficient of DiI varied within three regions. A uniform bright DiI rich region (L_d phase), a grey scale brightness (L_o phase), and a black DiI depleted region (gel phase). The L_o and L_d phases exhibited DiI and streptavidin recovery after photobleaching, whereas the gel phase exhibited no streptavidin recovery which falls in agreement of having streptavidin crystals bound to the surface of the bilayer. As incubation time of streptavidin with the membrane increases, streptavidin crystallization rate increases, and the L_o phases transitioned to gel phases where only two distinct areas of brightness of DiI were observed.

The membrane structure varied with the lipid phase present. Areas of L_o phase within a L_d background exhibit curvature when images by pTIRFM. Bulging of the L_o phase was detected as an increased brightness at its boundary in pTIRFM, decreasing the line tension between the co-existing phases[185]. In this case, biotin-streptavidin crosslinking altered the phase dynamics, induced domains formation, which lead to membrane structure change. The budding of the L_o

phase retracted back to a flat membrane topology when the L_o phase transitioned to a gel phase as incubation time increased (Fig. 40).

Circular and irregular L_o phase boundaries were observed within the time window before they transitioned to gel phases. The shape of the boundary depends on the lipid phases present[6,186,187], the physical state of the streptavidin (e.g. crystal)[184], and the interaction with the substrate. On free-floating bilayers (i.e. GUVs) circular co-existing L_o and L_d phases are observed upon streptavidin binding[6,180]. However, in our system, the lipid bilayer has formed directly on glass which have not only influenced the shape of the phase boundaries observed, but have also restricted the diffusion of the micron scale phases.

5.5.4 Symmetric binding inhibited phase separation

In order to decrease the membrane-substrate interaction, we have created multi-bilayer systems where a bilayer act as a cushion to separate the top bilayer under study from the glass substrate. The experiments with labelled and unlabeled streptavidin were then carried out, and the fluorescent signals of DiI and streptavidin were recorded in TIRFM. Regions of DiI depletion and streptavidin enrichment, depicted as phase separated regions, were observed only on the bilayer adherent to the glass substrate, while the free-floating bilayer patches exhibited uniform DiI and streptavidin brightness's. The labelled streptavidin was able to leak under the free-floating bilayer and bind to its bottom leaflet as well as to the top leaflet. This symmetric streptavidin binding inhibited the formation of phase separated regions as observed in the case of asymmetric binding. Leaflet binding mismatch and streptavidin crowding are critical for domain formation (Fig. 41).

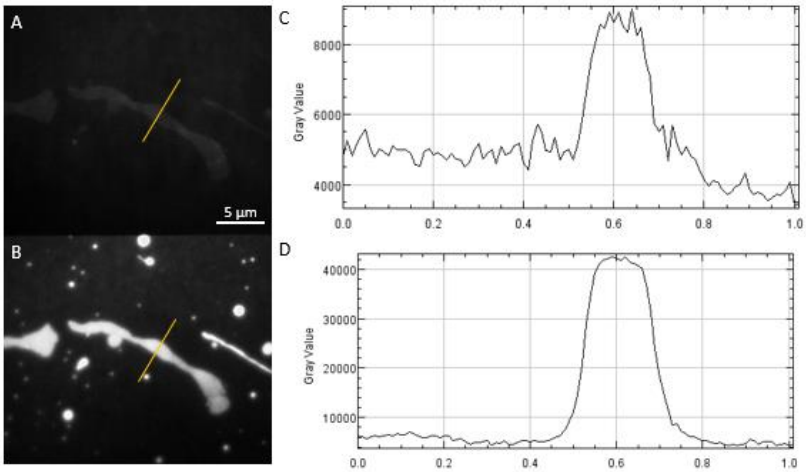

Figure 41. Symmetric addition of streptavidin-AF647 inhibited phase induction. (A) TIRF image of a POPC/DiI/Biotin membrane with two bilayers represented by brighter regions of DiI. (B) Streptavidin-AF647 enrichment on the membrane with 3x more streptavidin is observed on the 2 bilayers than the single flat bilayer region. (C,D) Histogram plot of brightness of the yellow line shown in (A,B) for the membrane and streptavidin channel, respectively.

5.5.5 Membrane curvature induction factors

In this study, we investigated the effects of clustering on membrane behavior and structural change. A consistency in the results was observed with varying biotinylated lipid concentrations within the membrane. No membrane structure or composition alteration was detected in the case of unlabeled streptavidin binding in contrast to the case of CTxB addition to the membrane reported in chapter 4. Membrane curvature detected in the case of the addition of fluorescently labelled streptavidin occurred as a result of the line tension between co-existing micron scale lipid phases. No direct nanoscale curvature induction by labelled streptavidin was detected as observed in CTxB-induced budding. CTxB crosslinking with five GM1 resulted in nanoscale membrane buds which was not observed in the case of streptavidin crosslinking to five biotinylated lipid. The variation in the results indicates another key factor in inducing membrane structure change: protein shape. Streptavidin is often referred to as a flat molecule with five biotin binding pockets, while CTxB molecular structure possess an intrinsic curvature where the five GM1 binding pockets reside at the edge of the molecule and slightly elevated from its center[163,188]. This allows the

membrane to wrap around CTxB upon binding. The difference in the molecular shape between CTxB and streptavidin is critical for the ability of these molecules to drive membrane bending.

5.6 Conclusions

Crosslinking membrane components is critical for certain cell response mechanisms. Crosslinking CTxB with its GM1 ganglioside on a quasi-one component bilayer has induced nanoscale membrane budding. In this study, crosslinking fluorescently labelled streptavidin with its lipid anchor biotin have induced lipid phase separation upon asymmetric binding to the bilayer. L_o/L_d and gel phases were observed to exist simultaneously shortly after the addition of streptavidin-AF647 to the membrane. The number and properties of the phases present depend on the streptavidin-AF647 incubation time. Surface crowding and line tension between the co-existing L_o/L_d phases drove membrane structure deformation and distinctly bulged out the L_o phase releasing the membrane from the glass substrate. After 40 minutes of streptavidin-AF647 addition, only two distinct phases are observed estimated to be L_d and gel phases depending on the DiI partitioning coefficient within each phase. Nanoscale budding is a unique property of CTxB due to its intrinsic molecular structure, a behavior that was not recorded in the case of biotin-streptavidin binding. Future studies might focus on the effects of varying the biotin-tagged lipids and exploring the effects of utilizing monovalent streptavidin upon crosslinking.

CHAPTER 6 CTXB VALENCY DRIVE MEMBRANE BENDING

6.1 Background

Membrane structure alteration by CTxB is critical for toxin internalization and cell toxicity. In order to understand the driving factors and the mechanism of membrane budding by CTxB, experiments have been carried out to determine if membrane curvature induction was due to CTxB structure and its valency or due to a local nanoscale membrane phase. To achieve this, we investigated the effects of varying [CTxB], GM1 concentration within the membrane, GM1 ceramide tail, and membrane composition[14,111,185]. Manipulating [CTxB] or [GM1] affects the number of crosslinked GM1 per CTxB molecule, while altering the GM1 ceramide tails or the membrane composition affects the nanoscale membrane phases if present. Further, replacing the pentamer CTxB by its mutant with a single functional GM1 binding site enabled investigating the effects of crosslinking on membrane structure manipulation[167].

Biological mechanisms at the cell surface is mainly affected by the kinetics properties and thermodynamics of ligand-receptor binding. Some reactions require a tetrameric binding such as the allergic reaction triggered by the high affinity binding of FcεRI to its immunoglobulin (IgE) receptor[189], others require a covalent binding such as peptide binding. The binding constant, association/dissociation constants, the number of available binding sites, and the number of crosslinked receptors dictate the mechanism of such an interaction and eventually affects the cell response. A multivalent ligand undergo a multi-step binding to its receptor within the membrane, such process affects the cellular response as detected in the case of immunological responses and cancer cells targeting by nanoparticles[190]. The interaction between a ligand and its receptor depends on several factors such as the: 1) diffusion-limited transport of the ligand to the surface hosting the receptor; 2) the number of binding sites; 3) concentrations of the ligand and the

receptor; 4) binding constant; 5) and the dissociation rate. High rate constants, such as that for biotin-streptavidin binding $k = 7x10^{7}\ M^{-1}\ sec^{-1}$ [191], indicate the mechanism of interaction between a single biotin and streptavidin molecules. For instance, the rate-limiting factor of this binding interaction is due to the diffusion of biotin to the streptavidin binding site.

For the case of cholera toxin binding to a membrane hosting GM1 molecules, the binding rate is $1.7x10^{5}\ M^{-1}\ sec^{-1}$ given by flow cytometry[192]. The kinetic measurement took into account the transport of CTxB to the membrane, the high binding affinity of CTxB to GM1, the cooperative binding of GM1 to CTxB[193], the different binding configurations, and the concentrations of CTxB and GM1 in solution and in the membrane. Investigating the effects of changing CTxB concentrations onto a bilayer hosting GM1 molecules is the main focus of this section. The number of crosslinked GM1 molecules by CTxB is important in dictating the toxin behavior, for instance mutant monovalent CTxB bound to a single GM1 molecule altered the toxin phase behavior as reported previously[167]. We have demonstrated that with a CTxB concentration of 0.25μg/mL and 0.3% GM1, nanoscale membrane budding and tubules were induced by the CTxB-GM1 binding. We hypothesize that this membrane structure alteration is dependent on both concentrations of CTxB and GM1. In this chapter, we present the effects of changing CTxB and GM1 concentrations on a POPC/GM1/DiI membrane imaged with PLM.

6.2 Materials and Methods

Mutant CTxB (mCTxB) was generously provided from Dr. Anne Kenworthy lab. The synthetic lipids (GM1 C16:1 and GM1 C18:0) were provided by Dr. Wayne Lencer.

6.3 Changing [CTxB] affects bud sizes

CTxB binds to the membrane in a multi-step process[192,193], which results in a variation of CTxB-GM1 configurations on the membrane[155], and number of bound GM1s[166]. Initially CTxB in

solution undergo 3D diffusion transport to the membrane, once it's in close proximity to a carbohydrate moiety of a GM1 molecule, CTxB binds to the GM1 with an effective association rate constant (~ 10^{-9}M). The probability of dissociation or binding to another GM1 molecule depends on the concentration and diffusion rate of GM1 within the membrane. For instance, in a highly concentrated GM1 hosting membrane, once a CTxB is bound to a single GM1, and a secondary GM1 molecule falls within close proximity of that CTxB molecule, theoretically binding will occur with equal binding rate as the initial encounter; however, the probability of association is higher 2-4x the initial binding rate due to the cooperative interaction and intrinsic attraction of neighboring GM1s[157,165,193]. This increased probability of binding to more than a single GM1 molecule depends on the relative concentrations of membrane bound CTxB to GM1 molecules. Receptor crosslinking occurs at a slow rate, therefore to increase the probability of binding to another GM1 before dissociation from the first bound GM1 occurs, the ratio of CTxB concentration to GM1 concentration must be very low. In this case, by keeping the GM1 concentration fixed and changing CTxB concentrations exposed to the membrane, we can control the number of crosslinked GM1 to a CTxB molecule, and predict the dominant population configuration of CTxB-GM1 structures.

The area of the CTxB pentamer is equal to 106 nm^2, for a 0.3% GM1 concentration within the membrane, 110 nm^2 of bilayer exists per GM1 molecule, thus a threshold CTxB concentration of 0.25 μg/mL would be sufficient to saturate all the CTxB binding sites. We explored a range of CTxB concentrations of 0.01, 0.1, 0.25, and 0.5 μg/mL to observe the effects of varying binding kinetics on membrane dynamics and structure.

Supported lipid bilayers were prepared, as described previously in chapter 2, with a 99.6% POPC, 0.3% GM1 and 0.3% DiI concentrations. CTxB was then introduced to the membranes.

Dual channel super resolution imaging was performed via an Optosplit where the membrane was images in PLM with λ_{exc} of 561 nm and dSTORM was performed for the CTxB-AF647 with a λ_{exc} of 647 nm. Time lapses were acquired up to 90 min of incubation time of CTxB with the membrane for all CTxB concentrations.

Upon the reconstruction of the super resolution images for both channels, we have detected varying behavior for the different CTxB concentrations. Nanoscale membrane deformation was detected for [CTxB] = 0.01, 0.1 and 0.25 µg/mL presented as areas of increased localization densities and ring-like structures detected by pPLM and dSTORM. However, uniform distribution of localizations was detected in pPLM indicating no change to membrane structure or dynamics for the case of high CTxB concentration (Fig. 42).

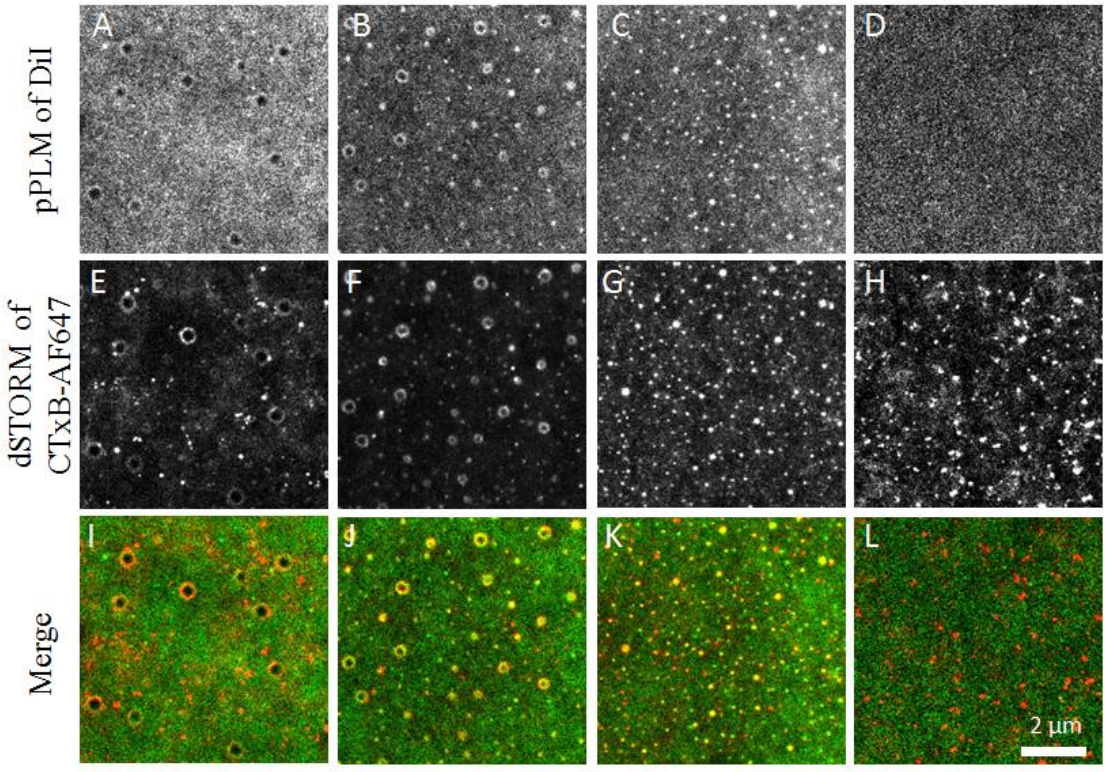

Figure 42. Nanoscale buds vary in size and density as function of [CTxB]. (A-D) pPLM reconstructed super resolution images of the membrane imaged in (lambda exc = 488), (E-H) reconstructed STORM images of CTxB localizations, and (I-L) color merge of the super resolution images of the membrane (green) and CTxB (red) at [CTxB] of 0.01,0.1,0.25, and 0.5 µg/ml for (A,E,I),(B,F,J),(C,G,K), and (D,H,L) respectively.

The density of buds within a given area increased with increasing CTxB concentration while the sizes of the detected buds decreased. 0.72, 1.41, and 7.5 buds/μm^2 were detected in pPLM for [CTxB] of 0.01, 0.1, and 0.25 μg/mL, respectively. The density of CTxB clusters also increased with increasing [CTxB] as expected. 4, 4.3, and 10.8 cluster/μm^2 was detected in dSTORM of CTxB-AF647 for [CTxB] = 0.01, 0.1 and 0.25 μg/mL, respectively. The detected buds were fewer but larger in the case of lower concentrations of CTxB, bud sizes detected in pPLM were 285 ± 66, 107 ± 41, and 54 ± 21 nm for [CTxB] of 0.01, 0.1 and 0.25 mg/mL, respectively (Fig. 43).

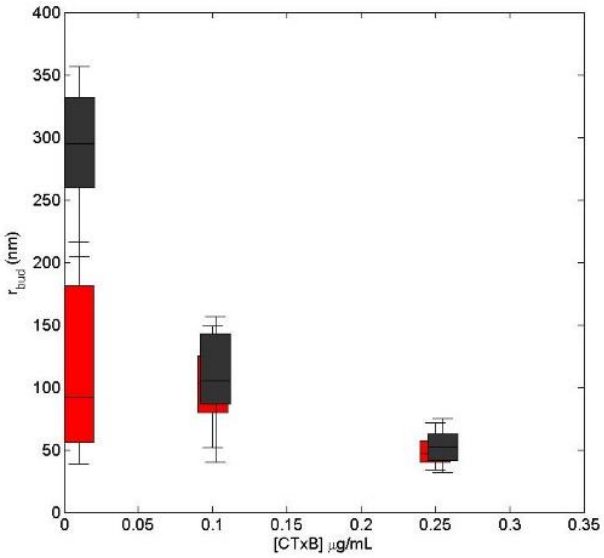

Figure 43 . Whisker plot for the sizes of the induced buds with varying [CTxB]. PLM and dSTORM size measurement for membrane buds (grey) and CTxB (red) at varying CTxB concentrations within the membrane, respectively.

6.4 CTxB binding kinetics

The change in number and size of induced membrane budding is solely dependent on the number crosslinked GM1 by CTxB. For varying CTxB or GM1 concentrations, the shape of the membrane around the toxin varied depending on the number of crosslinked GM1, and the extent of wrapping the membrane up around the toxin close to the GM1 binding pockets. In the case of low CTxB concentration ([CTxB] = 0.01 μg/mL) or high GM concentration (e.g. 1%), we expect

crosslinking of more than 1 GM1 bound per CTxB. This is due to the low relative concentration of CTxB to GM1 molecules; this is the case of an abundant GM1 molecules within the membrane, where a CTxB molecule is more likely to bind to a secondary and ternary GM1 as it diffuses within the membrane. A pentavalent binding might occur with a high binding affinity and low probability of dissociation. This cluster or unit of crosslinked GM1s by the CTxB exhibit a decreased mobility, and induced a local membrane bending upon crowding with other CTxB-GM1 units. The number of induced buds depends on the number of CTxB-GM1 units present to crowd and induce budding, while the size of the bud depends on the size and orientation of the units. For instance, a CTxB molecule bound to 3 GM1 molecules within the membrane exhibit a tilt with respect to the membrane plane[155,166]. This tilt allows the cluster to explore certain membrane orientations and preferentially partition at specific curvature regions (such as ridges). The limited number of present CTxB and GM1 clusters resulted in a lower density of induced buds but with a larger size where the CTxB preferentially partitioned at the bud necks.

As the concentration of CTxB increases on the membrane or as the GM1 concentration decreases within the membrane, the number of available secondary GM1s and the probability of binding to it decreases. An interplay between the diffusion-limited and concentration-dependent time for CTxB to reach the membrane, and the concentration-dependent time for a secondary GM1 to bind to a membrane-bound CTxB, determines the number of bound GM1s per CTxB molecule. In this case, the lateral diffusion coefficient of GM1 in a POPC membrane D_{GM1} is considered to be similar to the diffusion of membrane lipids $D_{GM1} \sim 10^{-8}$ cm^2/sec, as given in chapter 2. The rate constant of crosslinking to a secondary GM1 depends on GM1 concentration and diffusion within the membrane. In this case, k_2 is calculated according to[192]

$$k_2 = \frac{-8\pi D_{GM1}}{\ln(4A+0.46)} \qquad \text{(Eq. 28)}$$

Where A is the fraction of GM1 within the membrane. Thus the diffusion-limited concertation-dependent crosslinking rate is evaluated to $k_2 = 6.3x10^{-8}$ cm^2/sec. For a 0.3% GM1 i.e. ~ $9x10^{11}$ GM1 molecules/cm^2 bilayer area, the rate of crosslinking between a membrane bound CTxB to a secondary GM1 and crosslink is smaller than the rate of an unbound diffusing CTxB to bind to the membrane.

The brightness of CTxB-AF647 on the membrane was recorded during the addition of CTxB keeping constant experimental conditions while only varying [CTxB] added. The corresponding intensity profiles were plotted and the time constants were calculated by fitting the graph with a functional form of

$$I(t) = A\left(1 - \exp\left(-\frac{t}{\tau}\right)\right) + ct \qquad \text{(Eq. 29)}$$

Where A represents the maximum intensity, τ is the time constant, and the term (ct) is added to account for signal bleaching. Steeper graphs are recorded for higher [CTxB]s indicating faster saturation of CTxB on the membrane. The recorded time constants decreased from 9.6 ± 0.06 to 1.3 ± 0.01 for [CTxB] of 0.01 and 0.5 μg/mL, respectively. This reflects the multivalent binding property of CTxB, where in lower concentrations CTxB molecules were more likely to bind to multiple GM1 as they diffuse on the membrane where the crosslinking rate is relatively slow. While in the case of high CTxB concentration, the transport of CTxB to the membrane was relatively faster than the crosslinking rate, resulting in a popular monovalent binding where the available GM1 receptors were saturated 8x faster.

6.5 Nanoscale membrane buds depend on [GM1] within the membrane

Similar results were observed upon varying the GM1 concentration within the membrane. Membranes of 99.6, 99.4, 98.7 % POPC and 0.1, 0.3, and 1% GM1, respectively, were created. The selection of GM1 concentrations was based on conserving the ratios of CTxB to GM1 on the

membrane similar to the cases of changing the [CTxB]. 0.25 µg/mL of CTxB was added to the membranes of varying GM1 concentrations. Membranes were imaged for 90 min via PLM while STORM imaging revealed CTxB distribution on the membrane. The density and sizes of induced curvature regions varied with GM1 concentrations. Nanoscale buds were detected in membranes with [GM1] > 0.3%, while no curvature regions were detected for lower [GM1] (Fig. 44).

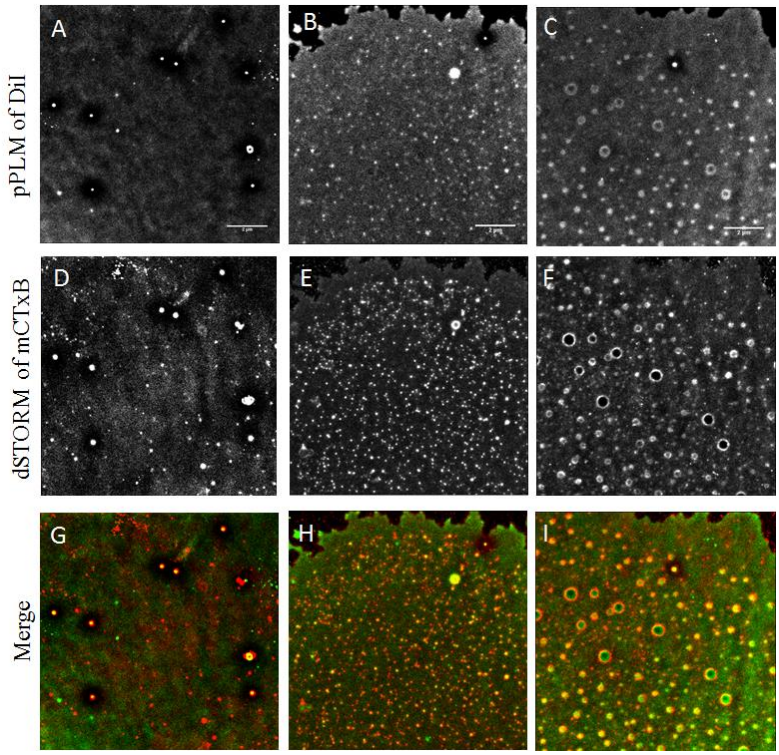

Figure 44. Nanoscale buds vary in size depending on [GM1] within the membrane. (A,B,C) pPLM images of the membrane, (D,E,F) STORM reconstructed images of CTxB-AF647, and (G,H,I) color merge for varying GM1 concentration of (A,D,G) 0.1, (B,E,H) 0.3, and (C,E,I) 1%, respectively.

The bud sizes increased from 54 ± 21 to 119 ± 50 nm and from 50 ± 14 to 132 ± 70 nm in the membrane and CTxB channels, as GM1 concentration within the membrane increased from 0.3 to 1%. On the other hand, the number of buds decreases from 0.69 ± 0.03 to 1.62 ± 0.1 buds/μm^2 as [GM1] increases from 0.3 to 1%. (Fig. 45)

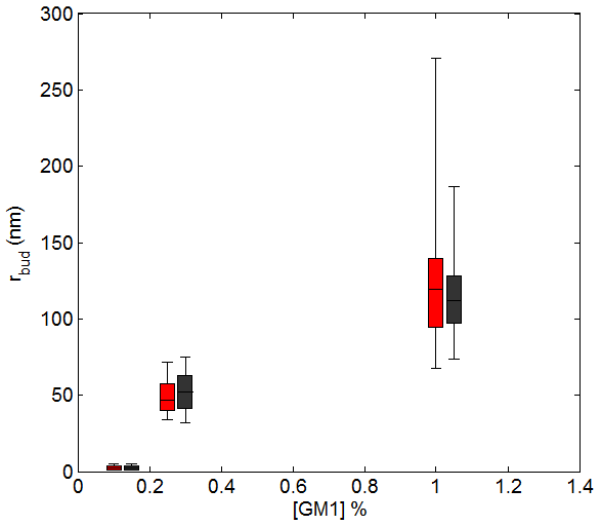

Figure 45. Whisker plot for the sizes of the induced buds with varying [GM1]. Size estimation of buds from PLM and dSTORM data for the induced membrane buds (grey) and CTxB (red) at varying GM1 concentrations within the membrane, respectively.

6.6 mCTxB inhibits nanoscale membrane bending

To determine whether the induced nanoscale membrane curvature depends on the multivalency of CTxB, and to confirm that binding to a single GM1 prohibit the toxin from altering the membrane structure as in the case of high [CTxB] and low [GM1], mutant CTxB was used. Fluorescently labelled mCTxB with a single active binding site was added to a 99.4% POPC/0.3% GM1/0.3% DiI at varying concentrations of 0.1, 0.25 and 0.5 µg/mL. Membranes were imaged via PLM for 90 min after mCTxB addition, and uniform density of DiI localizations was obtained in all [mCTxB] cases. This indicates that no change in membrane topology was recorded in all cases. Further, these results were confirmed after 24 hours of mCTxB addition. On the other hand, STORM data of mCTxB revealed uniform localization density across the membrane with areas of increased density. However, clustering of mCTxB did not correspond to regions of curvature in the membrane channel (Fig. 46). This was further confirmed by adding mCTxB to free floating bilayers where no invaginations were detected (Fig. 47).

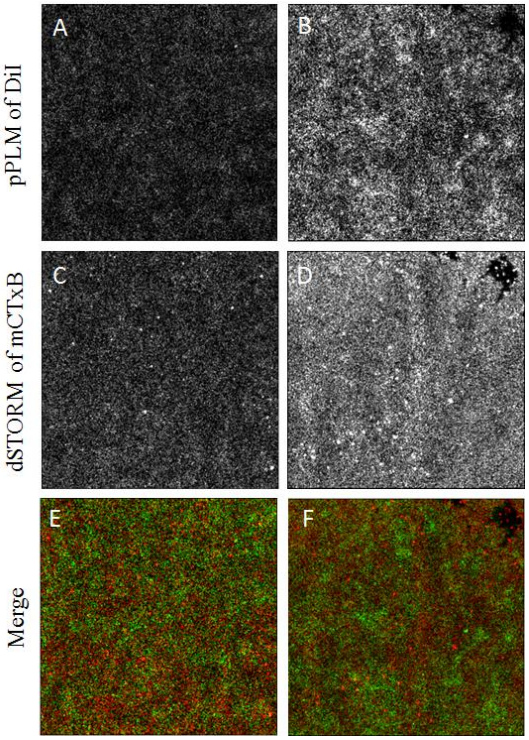

Figure 46. No membrane budding was detected in the case of mCTxB. Varying mCTxB concentration 0.1 (A,C,E) and 0.5 (B,D,F) µg/ml did not induce membrane budding. (A,B) pPLM reconstructed images of the membrane show no curvature, (C,D) reconstructed STORM images of mCTxB, and (E,F) color merge of the membrane (green) and CTxB (red).

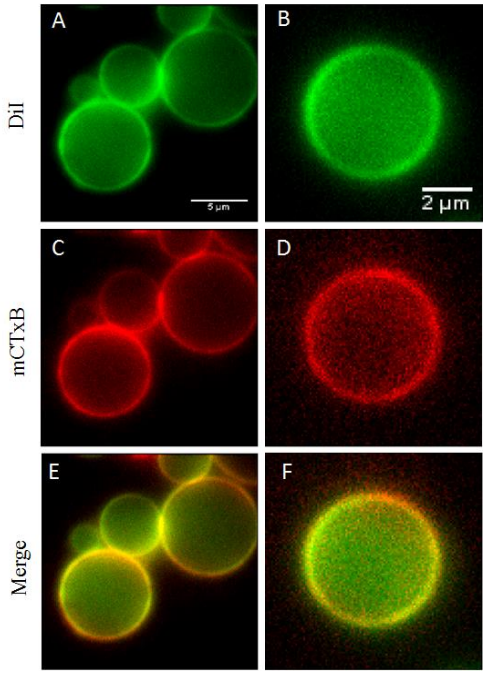

Figure 47. No inward budding was detected in the case of mCTxB added to GUVs. mCTxB was added to GUVs imaged in (lambda exc = 561 nm) (A,B), (C,D) uniform brightness of mCTxB distribution on the membrane, and (E,F) color merge of the membrane (green) and mCTxB (red).

Crosslinking the mCTxB with a primary anti-CTxB antibody created clusters of the mCTxB and its bound GM1s. Initially, 0.5 µg/mL mCTxB was added to a 99.4% POPC/ 0.3%GM1/ 0.3%DiI membrane and imaged for 90 minutes. No curvature induction was recorded. Then, antibodies were added to the membrane every 90 minutes at concentrations of 1:10,000, 1:1000, 1:500, and 1:100 .pPLM images of the membrane show uniform density of DiI localizations indicating a flat membrane surface with no induced curvature regions (Ffig. 48). Further, STORM results demonstrate an increased density of mCTxB clusters of localizations. However, these clusters did not correspond to similar regions in the membrane channel indicating an assembly of mCTxB by antibodies that did not induce an alteration on membrane structure.

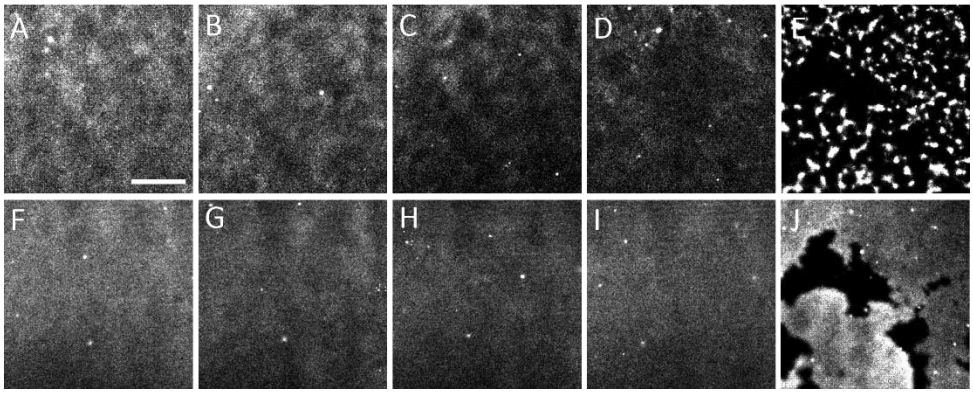

Figure 48. No curvature induction was recorded for mCTxB even upon clustering. Anti-CTxB addition to crosslink the monomer CTxB did not induce membrane topology change. (A-E) STORM images of the mCTxB-AF647, (F-J) pPLM images of the DiI membrane for the cases of increasing antibodies of 1:10,000, 1:1000, 1:500, and 1:100, respectively. Scale bar represents 2µm.

High throughput single particle tracking was performed on the DiI and mCTxB localizations to understand the corresponding lipid and protein dynamics as function of antibody concentration. The effect of crosslinking of mCTxB by antibodies was exhibited as change in toxin dynamics and diffusion rates. Remarkable decrease in the mCTxB diffusion was recorded as D decreased from 1.07 ± 0.15 to 0.35 ± 0.033 $\mu m^2/sec$ as the antibody concentration on the membrane increased from 0 to 1:500, respectively (Fig. 49, 50). However, a smaller shift in lipid dynamics

was recorded. Lipid diffusion did not show major variation in its diffusion rate where D = 1.057 ± 0.1 and 0.640 ± 0.15 μm^2/sec for the antibody concentration cases of 0 to 1:500 (Fig. 49, 51). Single step analysis revealed subpopulations of diffusers representing the clusters of crosslinked mCTxB by the antibodies and the varying numbers of mCTxB within. Two populations of diffusers was detected for mCTxB for all antibody concentrations, however, a detectable increase in the slow diffusers populations was observed as the concentration of anti-CTxB antibodies increased.

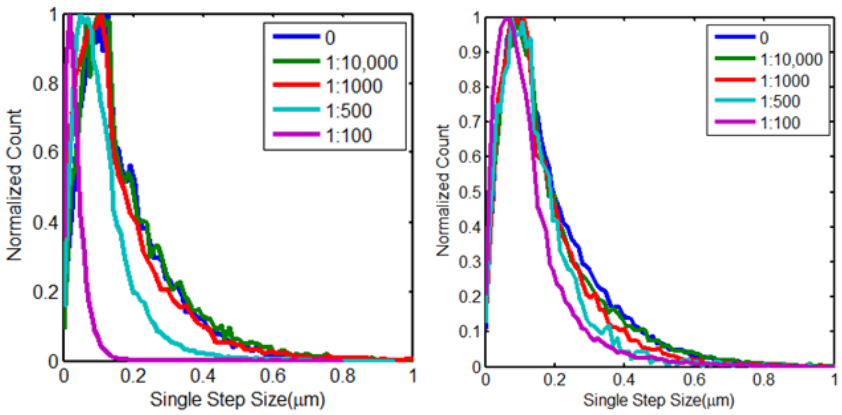

Figure 49. Histogram plot of single step of mCTxB (A) and DiI (B). Upon varying anti-CTxB antibody concentrations, single step mCTxB and DiI are shifted to lower values indicating smaller diffusion rates.

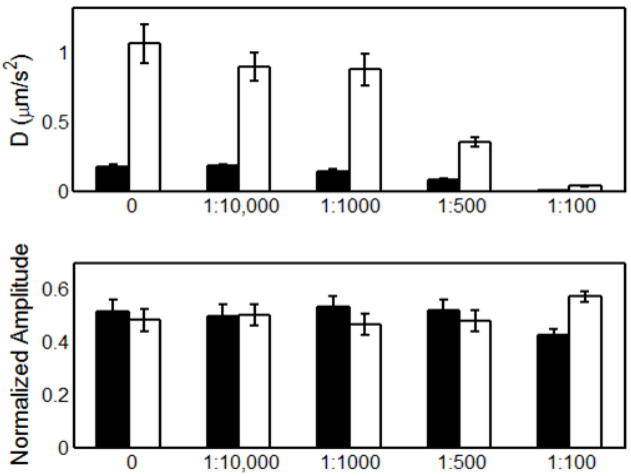

Figure 50. Bar plot of mCTxB diffusion rates and normalized amplitudes. At varying anti-CTxB antibody concentrations of 0, 1:10,000, 1:1000, 1:500, and 1:100, slower mCTxB diffusion is detected.

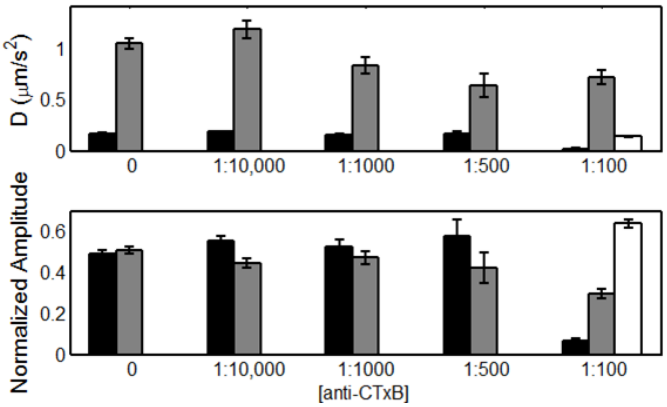

Figure 51. Bar plot of DiI diffusion rates and normalized amplitudes. At varying anti-CTxB antibody concentrations of 0, 1:10,000, 1:1000, 1:500, and 1:100, slower DiI diffusion is detected.

The agreement between the diffusion rate of mCTxB and WT CTxB in the case of high concentration indicates similar conformation of GM1 binding. In the case of high WT CTxB concentration (0.5 μg/mL), most CTxB molecules possess a single bound GM1, similar to the case of mCTxB where a single GM1 active binding site is present. The dynamics of both systems on the membrane is in agreement with a single diffuser population of D = 1.07 ± 0.15 and D = 0.87 ± 0.11 μm^2/sec for mCTxB and WT CTxB, respectively (Fig. 52,53).

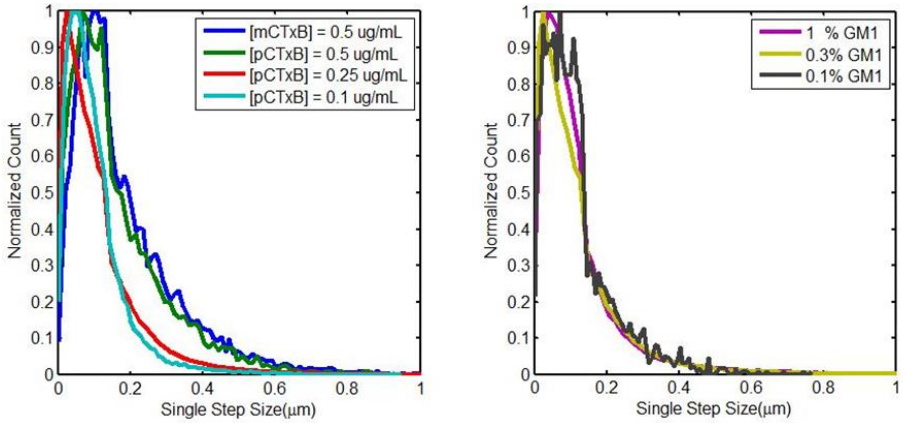

Figure 52. Histogram plot of single step of CTxB for varying [CTxB] and [GM1]. CTxB single step analysis in case of varying concentration (A) and [GM1] (B) reflects slower CTxB diffusion.

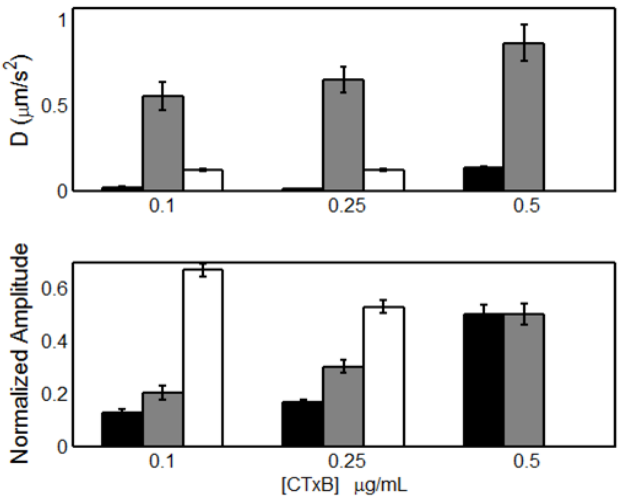

Figure 53. Bar plot of CTxB diffusion rates and amplitudes at varying [CTxB].

To ensure that the obtained results solely depended on the crosslinked mCTxB by the antibodies and that the observation is not due to a nonspecific binding of the antibody to the membrane, anti-CTxB antibodies were added to a 99.4% POPC/0.3%GM1/0.3%DiI without prior addition of CTxB to the membrane. No change in membrane structure or dynamic was recorded.

6.7 SPT reveals subpopulations of CTxB diffusers

Single particle tracking analysis was performed on localizations obtained in the CTxB channel to determine the dynamics of CTxB as function of membrane curvature. Single molecule CTxB diffusion was obtained for the different cases of varying [CTxB] concentrations. Subpopulations of diffusers were determined by fitting the histograms of CTxB single steps with Maxwell Boltzmann equations. Such analysis enables obtaining further information regarding CTxB dynamics on the membrane which might be blurred out upon analyzing full CTxB trajectories[194].

Three populations of diffusers exist for the case of WT CTxB where the slow diffuser population decreases as the [CTxB] increases indicating a faster CTxB dynamic on the membrane which agrees with having less bound GM1s.

6.8 Utilizing synthetic GM1s to test budding dependence on lipid structure

The protein-dependent nanoscale curvature induction have been examined. Its results implicate a major dependence of membrane structure alteration on the ratio of CTxB to GM1 within the membrane. To elucidate how nanoscale lipid phases and the membrane composition plays a role in curvature generation, GM1s with varying length and saturation level of their ceramide tails have been employed and incorporated into the membrane. Previous reports have demonstrated lipid sorting dependence on the ceramide structure of GM1 for CTxB trafficking in cells[118]. In this study, we have utilized synthesized non-fluorescent GM1 species with similar oligosaccharide head groups but with varying ceramide domains. GM1s of C16:1, C18:0, and C18:1 were incorporated into the lipid mixture before GUVs were created. The difference in the ceramide tails translate into a difference in the lipid phase and curvature preference of the molecule. GM1 species with kinked unsaturated ceramide chains preferentially partition into curved membrane regions and liquid disordered phase, while species with long straight saturated chains preferentially partition onto flat membrane areas and liquid ordered phase regions. The different sorting of GM1s enables testing the hypothesis of whether curvature generation depends on the lipid structure.

Fluorescently labeled WT CTxB was added to membranes of 99.4% POPC/ 0.3%DiI and 0.3%GM1 C16:1, GM1 C18:1, GM1 C18:0 independently. Membranes were images with PLM prior to CTxB addition and the uniform density of localizations obtained indicated the surface topology of the membrane. No curvature existed prior to the addition of CTxB to the membrane. Reconstructed super resolution images of the membranes exhibited regions with increased DiI localizations indicating nanoscale membrane curvature regions coinciding with increased density

of CTxB localizations for all cases of GM1 ceramide tails. This indicates that varying the GM1 tail structure did not prevent curvature generation (Fig. 54)

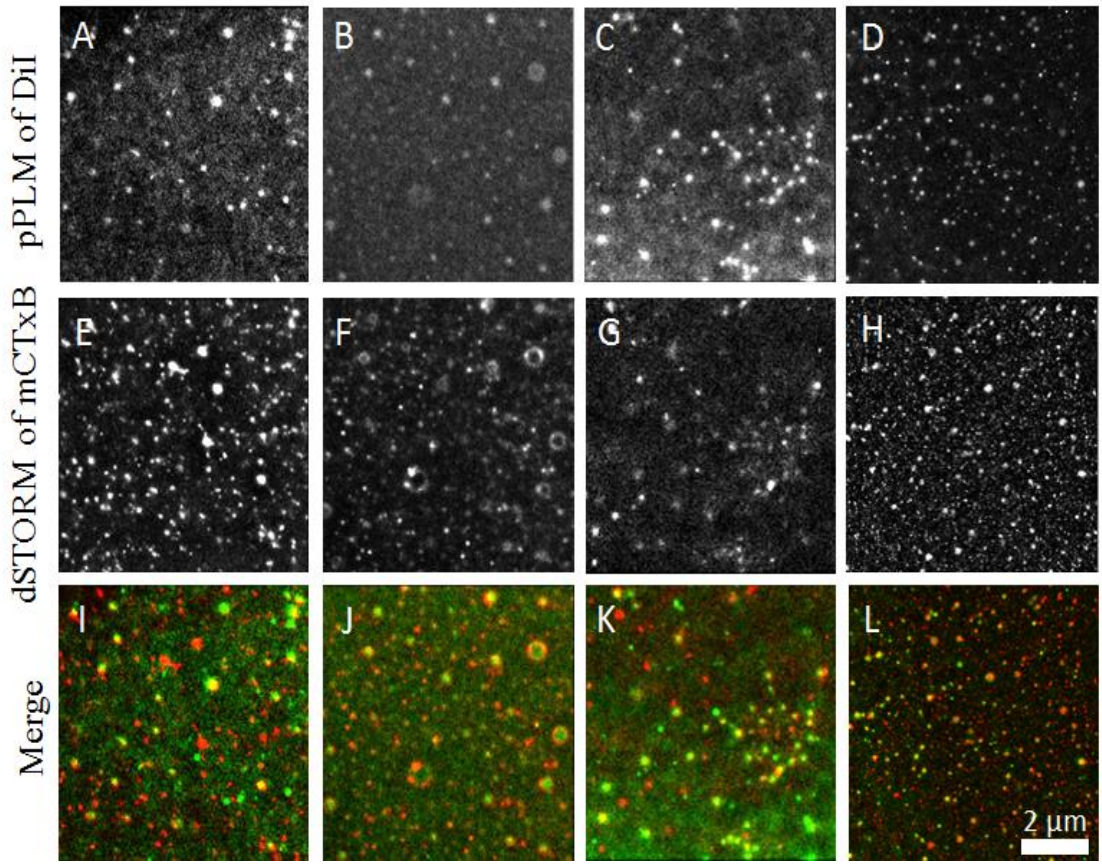

Figure 54. Nanoscale buds detected with varying membrane lipid composition. (A-D) pPLM images of DiI, (E-H) reconstructed images of CTxB, and (I-L) color merge of the membrane (green) and CTxB (red) channels. Nanoscale buds appeared in the case of GM1 C16:1, GM1 C18:1, GM1 C18:0, and cholesterol for (A,E,I), (B,F,J), (C,G,K), and (D,H,L) respectively.

However, variation in size and density of induced curvature was detected (Fig. 55, 56). Higher number of buds was observed in the case of GM1 18:0 with smaller radii where r_{bud} is reported to be 105 ± 45 and 95 ± 40 nm in CTxB and pPLM channels, respectively. Larger buds were observed in the cases of GM1 C18:1 and GM1 C 16:1 with r_{bud} in CTxB was 144 ± 37 and 118 ± 57 nm, and in pPLM 147 ± 42 and 115 ± 39 nm, respectively. This indicates that the saturation level of the GM1 tail affects the bud formation process and initiate the intracellular signaling pathway through budding of the toxin rich membrane[118].

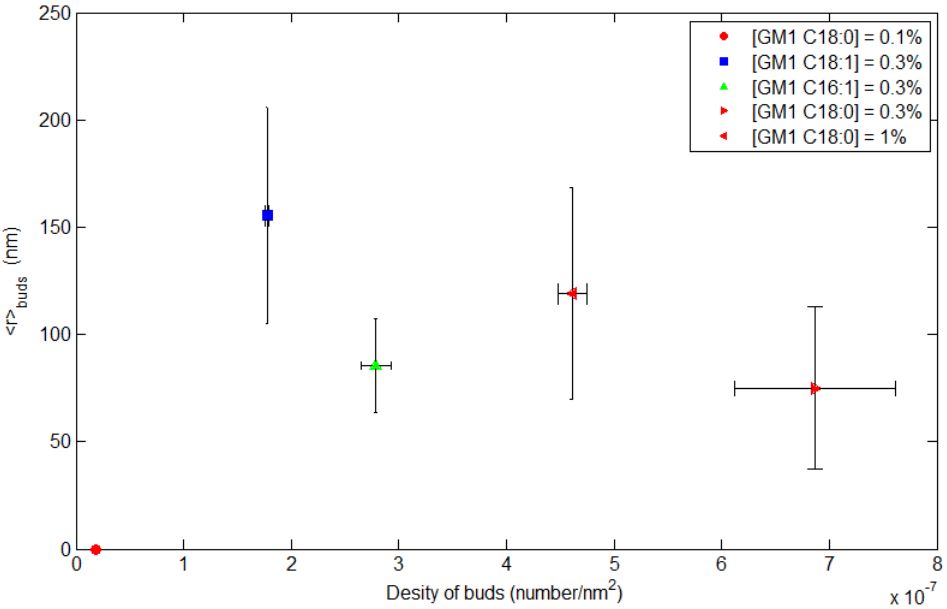

Figure 55. <r> and density plot of buds detected in pPLM for varying GM1 tail.

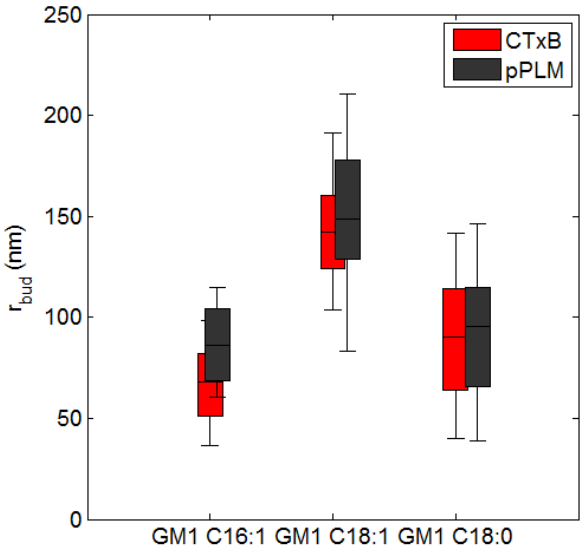

Figure 56. Whisker plot for the sizes of the buds for varying GM1 tails. Bud sizes vary with GM1 tail variation as shown in PLM (red) and dSTORM (gray) data.

6.8.1 BSA affect super resolution data

Stock samples of GM1s (C16:1 and C18:0) were synthesized with 1mg/mL BSA. The presence of BSA within the stock presented a challenge to super resolution imaging and DiI diffusion into and out of the curvature regions. To confirm that BSA have prohibited PLM from detecting curved regions observed in pTIRF microscopy, membranes of 99.4% POPC/ 0.3%DiI

and 0.3% GM1 C18:1 with and without added BSA was created and imaged for 90 minutes after CTxB addition. Decreased correlation between structure in the membrane channel and CTxB channel was obtained, confirming the hypothesis that BSA affects the quality of super resolution images. BSA restricted the DiI diffusion limiting the ability to detect some curvature regions in super resolution. Decreasing the laser power and acquiring super resolution movies of blinking fluorophores with 30 seconds intervals overcame the challenge, enabled the detection of the curvature regions, and facilitated the reconstruction of super resolution images with high correlation between the membrane and CTxB channels.

6.9 Cholesterol addition did not prevent membrane buds formation

We then examined whether changing membrane composition, mainly adding cholesterol to the membrane to dissociate any nanoscale liquid ordered phases or GM1 rich phase, affects the CTxB ability to induce curvature. Membranes of 69.4% POPC/ 30% Cholesterol/ 0.3% GM1 and 0.3% DiI were prepared. No curvature existed prior to CTxB addition. However, imaging the membrane for a length of 90 minutes after CTxB addition displayed a coincided increased density of localizations in DiI and CTxB channels. This indicated nanoscale curvature formation in the membrane channel enriched with CTxB. (Fig 54) The addition of cholesterol to the membranes did not prohibit the process of nanoscale budding driven by CTxB.

6.10 Conclusions

The mechanism of curvature induction by CTxB was examined to determine whether curvature generation depend upon the valency of CTxB or the membrane lipid composition. First, to test the hypothesis that curvature generation depends on the valency of CTxB; i.e. the number of crosslinked GM1s per CTxB molecule; different measure were taken including varying [CTxB], [GM1], and utilizing mCTxB. The interaction between the pentamer CTxB and its ganglioside

GM1 was studied, and a kinetics based multi-step binding of CTxB to GM1 was investigated on planar quasi-one component bilayers via PLM. In sum, crosslinking induced nanoscale membrane bending depicted as clustering of localizations obtained in the membrane and CTxB channels by pPLM and dSTORM, respectively. Ring-like structures were observed in both channels for lower CTxB or high GM1 concentrations, in which CTxB preferentially partitioned at the neck region, was bound to more than a single GM1 molecule, and induced nanoscale vesiculation that grew in size > 200 nm. We demonstrated that the number of crosslinked GM1 decreases as the concentration of CTxB on the membrane increases, altering the toxin's effect on the membrane. Membrane buds decreased in size while increasing in number as the CTxB concentration increased. Beyond a critical CTxB concentration of 0.25 μg/mL and lower than GM1 concentration of 0.3%, no membrane deformation was detected. Subpopulations of diffusers was recorded for the different cases of varying the [CTxB] and [GM1]. Mainly, slower diffusion of CTxB was recorded upon decreasing the [CTxB] added or upon increasing the [GM1]. The diffuser subpopulations corresponds to the CTxB molecules with different number of crosslinked GM1s per molecule. In sum, these studies uncover the modes of interactions of CTxB with GM1, and its effect on the membrane structure. Further, manipulating the membrane composition via the addition of Cholesterol and the alteration of the lipid structure with synthetic GM1s of varying ceramide tails, did not prevent the formation of membrane buds, but it did affect the sizes and density of induced buds.

Understanding the mechanisms of multivalent binding and its effect on the membrane is crucial to apprehend the chain of events that occur during a viral infection, immunological response, allergic reaction, and further cellular functions. This will enable the engineering of a more thoughtful, selective sophisticated routines and drugs in multivalent ligand studies.

CHAPTER 7 SUMMARY AND OUTLOOK

The curvature of biological membranes at the nanometer scale is critically important for vesicle trafficking, organelle morphology, and disease propagation. The initiation of membrane bending occurs at a length scale that is irresolvable by most super-resolution optical microscopy methods. This study reports the development of polarized localization microscopy (PLM), a pointillist optical imaging technique for the detection of nanoscale membrane curvature in correlation with single-molecule dynamics and molecular sorting. PLM combines polarized total internal reflection fluorescence microscopy (TIRFM) and single-molecule localization microscopy to reveal membrane orientation with sub-diffraction-limited resolution without reducing localization precision by point spread function (PSF) manipulation. Membrane curvature detection with PLM requires fewer localization events to detect curvature than 3D single-molecule localization microscopy (*e.g.*, PALM or STORM), which enables curvature detection 10x faster via PLM. With rotationally confined lipophilic fluorophores and the polarized incident fluorescence excitation, membrane-bending events are revealed with super-resolution. Engineered hemispherical membrane curvature with a radii $\geq$ 24 nm was detected with PLM and individual fluorophore localization precision was 13 ± 5 nm. PLM detected membrane curvature and resolved membrane topography with 1 sec of acquisition time at (1.2 ± 0.1) x 10^{-6} localizations/nm^2/frame.

Further, deciphering molecular mobility as a function of membrane topology was enabled. The diffusion coefficient of individual DiI molecules was faster in planar supported lipid bilayers than within nanoscale membrane curvature. The change in the lipid diffusion coefficient at the curvature locations did not solely depend on the geometry of the membrane. It also reflected the change in the membrane viscosity as the lipid packing mechanism varies between flat and curved membrane.

Radial line scans of pPLM localizations reveal radii of curvature of 32 ± 4, 50 ± 14, 60 ± 13 nm for membranes over the nanoparticles radii of 24, 51, and 70 nm, respectively. Further, a 6x increase in the SNR is obtained by PLM over traditional TIRFM. The theoretically estimated localization probabilities versus membrane orientation well reproduced experimental data. The unique spatiotemporal resolution of PLM is suited to monitor membrane structure variation with lipid and protein dynamics. Through the theoretical foundation and experimental demonstration provided here, PLM is poised to become a powerful technique for revealing the underlying biophysical mechanisms of membrane bending at physiological length scales.

PLM enabled deciphering the molecular mechanisms of toxin-membrane interactions that has been limited by available experimental techniques. Multi-colored fluorescence co-localization of lipids and proteins to the membrane curvature was performed. Membrane buds were first detected with <50 nm radius, grew to >200 nm radius, and extended into longer tubules with dependence on the membrane tension and CTxB concentration. Compared to the concentration of the planar supported lipid bilayers, CTxB was (12 ± 4)x more concentrated on the positive curvature top and (26 ± 11)x more concentrated on the negative Gaussian curvature neck of the nanoscale membrane buds. CTxB is frequently used as a marker for liquid-ordered lipid phases; however, the coupling between CTxB and membrane bending provides an alternate understanding of CTxB-induced membrane reorganization. These findings allow for the reinterpretation of prior observations by correlating CTxB clustering and diffusion to CTxB-induced membrane bending. Single-particle tracking was performed on single-lipids and CTxB to reveal the correlations between single-molecule diffusion, CTxB accumulation, and membrane topography. Slowed lipid and CTxB diffusion was observed at the nanoscale buds locations, suggesting a local increase in the effective membrane viscosity or molecular crowding upon membrane bending. These results

suggest inherent CTxB-induced membrane bending as a mechanism for initiating CTxB internalization in cells that could be independent of clathrin, caveolin, actin, and lipid phase separation.

Crosslinking of membrane associated lipid and proteins is essential for various cellular functions. In this study we recorded the changes in membrane structure and composition due to two systems: biotin-streptavidin, and CTxB-GM1 binding. Upon clustering on a quasi-one component bilayer, micron scale regions enriched with streptavidin were detected followed by a rapid depletion of DiI within those regions. The variation of DiI partition coefficients within those regions indicated the presence of distinct lipid phases. Curved L_o phases were observed to bulge out of the L_d lipid phase background bilayer. Alteration to membrane composition and structure was driven by biotin-streptavidin complex, and mainly dependent on streptavidin state. Streptavidin crystallization affected the lipid phase it's bound to resulting in a phase transition from a L_o phase to a gel phase. This was further verified by the lack of DiI and streptavidin signal recovery after photobleaching. The molecular structure of streptavidin dictated its effect on the membrane, lacking an intrinsic curvature within its structure as CTxB, streptavidin binding did not induce nanoscale membrane curvature.

On the other hand, in theCTxB-GM1 binding system, induced membrane structure alteration was observed. Nanoscale membrane buds were detected upon crosslinking CTxB with its ganglioside receptor GM1. We proposed two hypothesis to determine the mechanism that governs curvature generation by CTxB: Valency or lipid structure. The crosslinking ability and multivalency of CTxB was tested by varying [CTxB], [GM1], and introducing mCTxB to artificial supported lipid bilayer. Moreover, changing the membrane composition by the addition of cholesterol and utilizing synthetic GM1s of varying ceramide tails aimed to examine whether lipid

structure and composition played a role in driving curvature generation. We reported a change in membrane bud size and density upon changing the number of bound GM1s per CTxB molecule and GM1 tail structure. Adjusting the lipid composition and GM1 structure had no effect and did not prevent curvature induction as expected. Based on our findings we determine that crosslinking receptors is the mechanism of toxin internalization, and we propose that molecules adopt this mechanism in clathrin-independent endocytosis events. Crosslinking membrane receptors triggers a cascade of events for cell signaling or initiate a cell response each dependent on the crosslinked molecules.

APPENDIX A POROSOMES PREFERENTIAL PARTITIONING

Porosomes are lipoprotein structures that reside at the cell membrane and play an important role in secretion[195]. Partial vesicle docking, fusion, and content release occurs at the porosomes sites that represent a portal for regulating cargo transfer. This protein complex measures 180 nm in pancreatic insulin secreting cells, and composed of 30 to 40 core proteins[196]. In previous studies, SEM imaging and TIRF microscopy have been utilized to determine the properties of porosomes and the function of its proteins. In the current study, super resolution imaging is employed to determine the curvature preference of this complex.

Isolated fluorescently labelled porosomes from insulin secreting Min6 cells were incorporated into artificial lipid bilayers draped upon 140 nm and 500 nm nanoparticles. TIRF imaging was then performed to determine the distribution of porosomes as function of curvature. Super resolution imaging provided nanoscale information regarding preferential portioning of the complex as function of membrane curvature.

Porosomes partition onto curvature regions

Distinct imaging channels were required as the bilayer (99.7% POPC and 0.3% DiI) was excited at $\lambda_{exc} = 561$ nm, nanoparticles (140 nm) excited at $\lambda_{exc} = 488$ nm, and the porosomes excited at $\lambda_{exc} = 647$ nm. TIRF images revealed increased porosomes brightness at sites of curved membrane at the nanoparticle sites (Fig. 57). To confirm the integrity of the bilayer and the porosomes reconstitution into the artificial bilayer, control experiments were carried. To confirm that the complex was fully incorporated into the bilayer, and that the increased porosomes partitioning is due to membrane curvature rather than sticking to the nanoparticle itself, porosomes were added to nanoparticles on glass without a lipid bilayer. No increased porosomes brightness was detected on the nanoparticles in comparison to the surrounding glass, this indicates that the

porosomes did not stick to the nanoparticles and they preferentially partitioned on the curved membrane above the nanoparticle. Next, porosomes brightness on the flat membrane was compared to brightness on sites of membrane curvature. 20x more porosomes existed on sites of membrane curvature in comparison to flat regions.

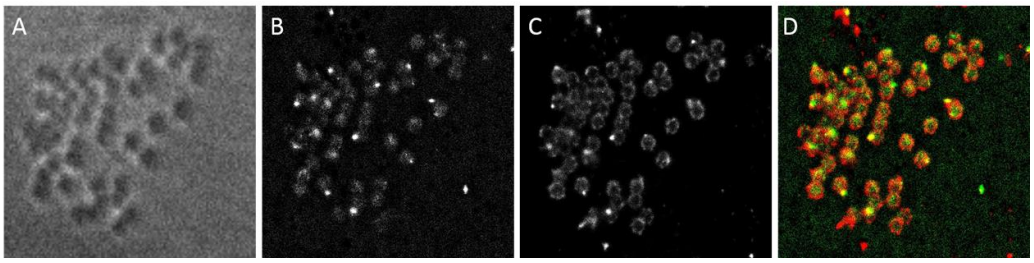

Figure 57. Porosome complex preferentially partition at regions of curvature. (A) 500 nm non-fluorescent polystyrene nanoparticles are images in bright field. (B) STORM reconstructed image of the POPC/DiI membrane in (lambda exc = 561 nm) draped upon the nanoparticles. The increased density of localizations indicated regions of membrane curvature corresponding to the membrane created on top of the nanoparticles. (C) Reconstructed STORM images of fluorescently labelled porosomes by (lambda exc = 647 nm). The ring-like shape of the localizations indicates the location of the porosomes around the neck of the created curvature. (D) Color merge of the membrane (green) and the porosome complex (red).

Super resolution STORM imaging was then performed to obtain nanoscale information regarding porosomes location and dynamic. An increased density of localizations was detected in the porosomes and the membrane channel at the 500 nm nanoparticle locations (Fig. 57).

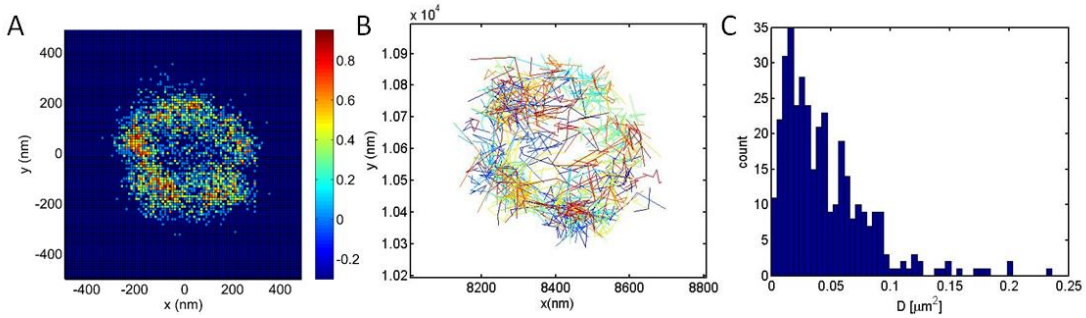

Figure 58. Porosomes dynamics on curved membrane over 500 nm NP. (A) 2D histogram plot of porosomes localizations. (B) Linked trajectories of porosomes localizations. (C) Extracted diffusion rates of SPT data.

The high density of localizations in the membrane channel corresponds to the increased membrane per pixel at the curved membrane locations. 0.1 ± 0.01 porosomes/ μm^2 were detected

at flat bilayer regions while 4.6 ± 0.1 porosomes/ μm^2 were detected on curved membrane, a 40x increase in density indicating the preferential partitioning of porosomes at curvature regions. Further, SPT revealed decreased porosomes diffusion on curved membrane D = 0.052 ± 0.01 $\mu m^2/sec$ in comparison to flat membrane regions where D = 0.16 ± 0.1 $\mu m^2/sec$. (Fig. 58)

Radial line scans of the localizations of DiI reveals decreased DiI density at the neck region of the curvature created by the 500 nm NPs beneath the lipid bilayer. Further experiments were carried out to examine the DiI distribution on curved membranes in the absence of porosomes. This study revealed increased DiI localizations at the curved membrane, in particular at r = 250 nm, in contrast to the case of DiI distribution in the presence of porosomes. The decreased localization density of DiI at the neck region of the curvature reveals important information regarding the distribution of porosomes and its effects on the membrane lipids. The protein complex preferentially partitioned at the curvature region leading to lipid reorganization perceived as DiI depletion (Fig. 59).

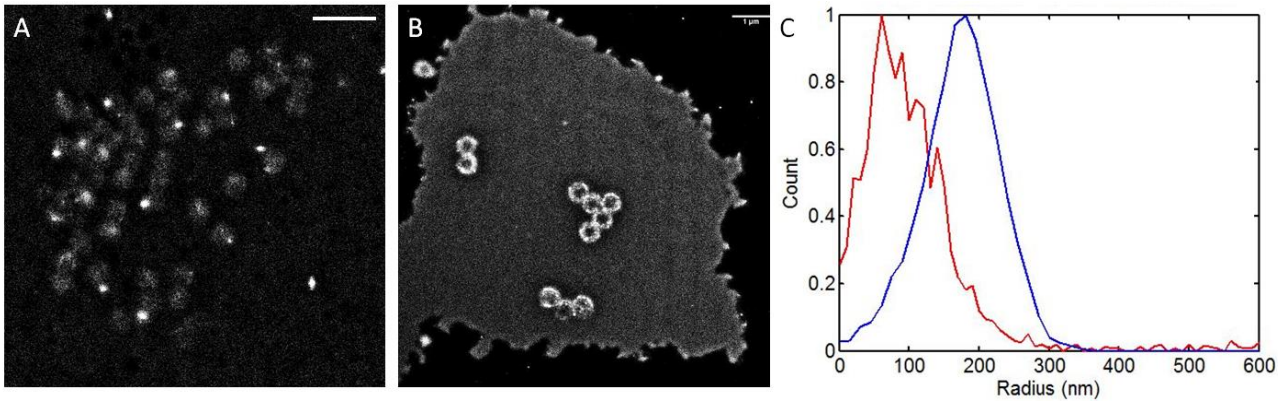

Figure 59. DiI distribution varies in the presence of porosomes. STORM reconstructed images of DiI localizations in a 99.7% POPC/0.3% DiI over 500 nm NPs (A) with and (B) without porosomes addition. (C) Radial line scan of DiI localizations over 500 nm NPs with (red line) and without (blue line) porosomes. The shift in the peak of the line scan from r = 170 nm for the blue line to r = 50 nm for the red line indicates a decrease of DiI localizations at the neck of the curvature. This shift corresponds to DiI depletion from the neck region for porosome incorporation and preferential partitioning at the curvature. This shows the variation in DiI distribution in the presence of porosomes incorporated within the membrane.

Phase preference of the protein complex

To determine the distribution of porosomes as function of membrane lipid phase. Synthetic supported lipid bilayers were prepared of 1:1:1 DOPC/DPPC/Cholesterol with 0.3% DiI and 0.3% DiO. This composition enabled the observation of two distinct liquid phases at 30 C. However, upon the addition and incorporation of porosomes into the membrane, membrane structure alteration was detected. Ridges and curvature was created and extended out of the membrane spanning a range of hundreds of nanometers, such regions were enriched with porosomes and liquid disordered phase. These structures were not created in bilayers of POPC/DiI and did not occur in ternary bilayers prior to porosomes addition. (Fig. 60, 61). The intrinsic cup-shape curved structure of the porosome along with possessing Syntaxin and SNARE proteins which preferentially partition onto L_d phase might explain the porosome lipid phase preference[197].

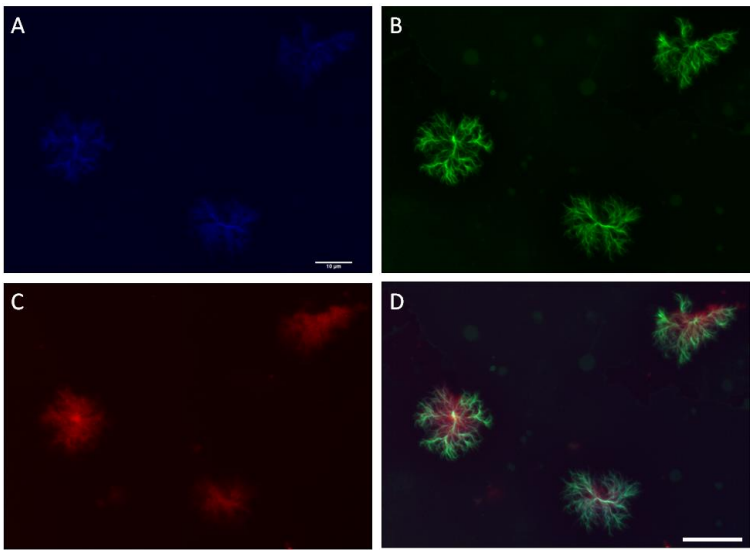

Figure 60. Membrane structure alteration after addition of porosomes. TIRF images of the (A) membrane in 488 nm, (B) 561 nm, (C) the porosomes in the 647 channel, and (D) their color merge. Scale bar represents 5 µm.

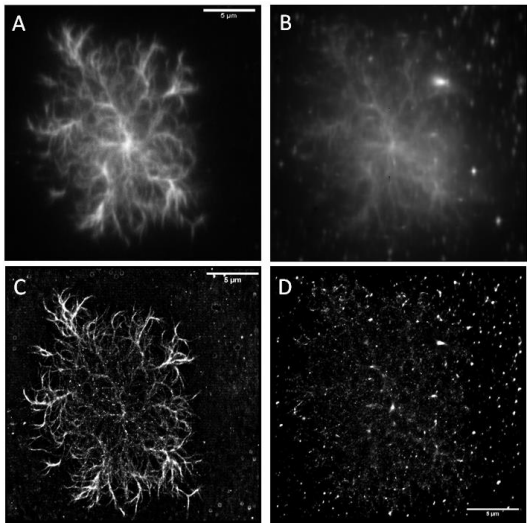

Figure 61. Super resolution images of the induced membrane structure. TIRF images of (A) DiI in 561 nm, and (B) the porosomes in the 647 channel. (C, D) Super resolution STORM images of (A, B), respectively. Scale bar represents 5 µm.

Conclusions

To better understand the structure, function, and location of the protein complex, TIRF and super resolution imaging were employed to detect its distribution as function of nanoengineered curvature on synthetic bilayers. Porosomes preferentially partitioned at curvature locations created by draping a bilayer on 500 nm nanoparticles. 40x more localizations were detected in the porosomes channel on curved regions in comparison to flat membrane areas. Further, slowed porosomes diffusion was recorded on curved regions. The protein complex preferentially partitioned at the L_d phase regions driving membrane structure alteration in ternary mixture of lipids.

APPENDIX B ANALYSIS PROCEDURE

Super resolution images were reconstructed from thousands of movies of blinking fluorophores using the ImageJ plugin: ThunderSTORM. Macros were recorded and used in batch processing analysis. To find the location of single blinking fluorophores through ThunderSTORM, we first applied a wavelet filter (B-spline) with scale and order of 3. Then, each fluorophore point spread function was fitted with a Gaussian function of radius of 3 and sigma of 1.6 as input parameters within the plugin. Super resolution reconstructed images were then plotted as 2D histogram of localizations. Further, tetraspecs locations were cropped, fitted, and corrected for drift. The drift correction file was then saved and applied to the full data set. Further analysis such as locating membrane buds, evaluating their sizes, plotting radial and density line scans; were conducted via routines and codes written in MATLAB.

Bud Identification Routine

Nanoscale membrane buds induced by CTxB was detected in the membrane channel as increased clustering of localizations accompanied with an increased density of localizations in the CTxB channel. Such regions were identified via home written MATLAB code that locate regions of high localization density based on a user input threshold. Locations with > 3x density of the background flat membrane was detected and saved as buds locations. Moreover, only locations with increased localization density detected in both channels were considered nanoscale buds.

Single-molecule dynamics analysis

A written MATLAB code that utilized utrack , a tracking algorithm, was used for linking trajectories of single fluorophores within 500 nm in subsequent frames for single step size and diffusion analyses. For subpopulations analysis, a histogram of fluorophores single step sizes was plotted then fitted with a Maxwell-Boltzmann distribution to extract the diffusion rates.

To determine the average diffusion coefficient of a single trajectory, average MSDs as function of the time interval (Δt) were plotted and fitted linearly to extract the diffusion rate through the fourth time point.

Dual-channel imaging and alignment

Merging and overlapping the different imaging color channels required a transform code that allowed shifting and rotating the super resolution data to map both channels to same location and overcome any physical imperfections in the optosplit alignment. Tform, transformPointsForward, and transformPointsInverse are matlab functions utilized to transform the channels for perfect overlay.

SCIENTIFIC CONTRIBUTIONS

1. Kabbani, A.M., and C.V. Kelly. 2017. Nanoscale Membrane Budding Induced by CTxB and Detected via Polarized Localization Microscopy. Biophys. J. 113: 1795–1806.

2. Rajagopal, A., S. Kulkarni, K.T. Lewis, X. Chen, A. Maarouf, C.V. Kelly, D.J. Taatjes, and B.P. Jena. 2015. Proteome of the insulin-secreting Min6 cell porosome complex: involvement of Hsp90 in its assembly and function. J. Proteomics. 114: 83–92.

3. Kabbani, A.M., X. Woodward, and C.V. Kelly. 2017. Revealing the Effects of Nanoscale Membrane Curvature on Lipid Mobility. Membranes. 7.

4. Kabbani, A.M., and C.V. Kelly. 2017. The Detection of Nanoscale Membrane Bending with Polarized Localization Microscopy. Biophys. J. 113: 1782–1794.

REFERENCES

1. al, W. D., et. Determination of plasma membrane lipid mass and composition in cultured Chinese hamster ovary cells using high gradient magnetic affinity chromatog... - PubMed - NCBI. Available at: https://www.ncbi.nlm.nih.gov/pubmed/8387513. (Accessed: 8th December 2017)
2. Lingwood, D. & Simons, K. Lipid Rafts As a Membrane-Organizing Principle. *Science* **327,** 46–50 (2010).
3. Brown, D. A. & London, and E. Functions of Lipid Rafts in Biological Membranes. *Annu. Rev. Cell Dev. Biol.* **14,** 111–136 (1998).
4. Schmidt, M. L. & Davis, J. H. Liquid Disordered-Liquid Ordered Phase Coexistence in Lipid/Cholesterol Mixtures: A Deuterium 2D NMR Exchange Study. *Langmuir ACS J. Surf. Colloids* **33,** 1881–1890 (2017).
5. Khadka, N. K., Ho, C. S. & Pan, J. Macroscopic and Nanoscopic Heterogeneous Structures in a Three-Component Lipid Bilayer Mixtures Determined by Atomic Force Microscopy. *Langmuir ACS J. Surf. Colloids* **31,** 12417–12425 (2015).
6. Veatch, S. L. & Keller, S. L. Seeing spots: Complex phase behavior in simple membranes. *Biochim. Biophys. Acta BBA - Mol. Cell Res.* **1746,** 172–185 (12).
7. Pataraia, S., Liu, Y., Lipowsky, R. & Dimova, R. Effect of cytochrome c on the phase behavior of charged multicomponent lipid membranes. *Biochim. Biophys. Acta* **1838,** 2036–2045 (2014).
8. Leptihn, S. *et al.* Constructing droplet interface bilayers from the contact of aqueous droplets in oil. *Nat. Protoc.* **8,** 1048–1057 (2013).

9. Gross, L. C. M., Castell, O. K. & Wallace, M. I. Dynamic and Reversible Control of 2D Membrane Protein Concentration in a Droplet Interface Bilayer. *Nano Lett.* **11,** 3324–3328 (2011).

10. Callan-Jones, A., Sorre, B. & Bassereau, P. Curvature-Driven Lipid Sorting in Biomembranes. *Cold Spring Harb. Prespectives Biol.* **10,** 1–14 (2011).

11. Vind-Kezunovic, D., Nielsen, C. H., Wojewodzka, U. & Gniadecki, R. Line tension at lipid phase boundaries regulates formation of membrane vesicles in living cells. *Biochim. Biophys. Acta BBA - Biomembr.* **1778,** 2480–2486 (2008).

12. Campelo, F., McMahon, H. T. & Kozlov, M. M. The Hydrophobic Insertion Mechanism of Membrane Curvature Generation by Proteins. *Biophys. J.* **95,** 2325–2339 (2008).

13. Frolov, V. A., Shnyrova, A. V. & Zimmerberg, J. Lipid Polymorphisms and Membrane Shape. *Cold Spring Harb. Perspect. Biol.* **3,** a004747 (2011).

14. Baumgart, T., Hess, S. T. & Webb, W. W. Imaging coexisting fluid domains in biomembrane models coupling curvature and line tension. *Nature* **425,** 821–824 (2003).

15. Lai, C.-L. *et al.* Membrane Binding and Self-Association of the Epsin N-Terminal Homology Domain. *J. Mol. Biol.* **423,** 800–817 (2012).

16. Ford, M. G. J. *et al.* Curvature of clathrin-coated pits driven by epsin. *Nature* **419,** 361–366 (2002).

17. Tian, A. & Baumgart, T. Sorting of Lipids and Proteins in Membrane Curvature Gradients. *Biophys. J.* **96,** 2676–2688 (2009).

18. Parthasarathy, R., Yu, C. & Groves, J. T. Curvature-Modulated Phase Separation in Lipid Bilayer Membranes. *Langmuir* **22,** 5095–5099 (2006).

19. Anantharam, A., Axelrod, D. & Holz, R. W. Polarized TIRFM reveals changes in plasma membrane topology before and during granule fusion. *Cell. Mol. Neurobiol.* **30,** 1343–1349 (2010).

20. Llewellyn, G. N., Grover, J. R., Olety, B. & Ono, A. HIV-1 Gag associates with specific uropod-directed microdomains in a manner dependent on its MA highly basic region. *J. Virol.* **87,** 6441–6454 (6).

21. Witkowska, A. & Jahn, R. Rapid SNARE-Mediated Fusion of Liposomes and Chromaffin Granules with Giant Unilamellar Vesicles. *Biophys. J.* **113,** 1251–1259 (2017).

22. Kun, L. *et al.* IFITM Proteins Restrict Viral Membrane Hemifusion. *PLoS Pathog.* **9,** (2013).

23. Baumgart, T., Capraro, B. R., Zhu, C. & Das, S. L. Thermodynamics and Mechanics of Membrane Curvature Generation and Sensing by Proteins and Lipids. in *Annual Review of Physical Chemistry, Vol 62* (eds. Leone, S. R., Cremer, P. S., Groves, J. T. & Johnson, M. A.) **62,** 483–506 (Annual Reviews, 2011).

24. Kielian, M., Chanel-Vos, C. & Liao, M. Alphavirus Entry and Membrane Fusion. *Viruses-Basel* **2,** 796–825 (2010).

25. Pucadyil, T. J. & Schmid, S. L. Real-time visualization of dynamin-catalyzed membrane fission and vesicle release. *Cell* **135,** 1263–1275 (2008).

26. Kozlov, M. M., McMahon, H. T. & Chernomordik, L. V. Protein-driven membrane stresses in fusion and fission. *Trends Biochem. Sci.* **35,** 699–706 (2010).

27. Axelrod, D. Cell-substrate contacts illuminated by total internal reflection fluorescence. *J. Cell Biol.* **89,** 141–145 (1981).

28. Mattheyses, A. L., Simon, S. M. & Rappoport, J. Z. Imaging with total internal reflection fluorescence microscopy for the cell biologist. *J. Cell Sci.* **123,** 3621–3628 (2010).

29. Burke, N. V. *et al.* Neuronal peptide release is limited by secretory granule mobility. *Neuron* **19,** 1095–1102 (1997).

30. Oheim, M., Loerke, D., Stühmer, W. & Chow, R. H. The last few milliseconds in the life of a secretory granule. Docking, dynamics and fusion visualized by total internal reflection fluorescence microscopy (TIRFM). *Eur. Biophys. J. EBJ* **27,** 83–98 (1998).

31. Allersma, M. W., Wang, L., Axelrod, D. & Holz, R. W. Visualization of regulated exocytosis with a granule-membrane probe using total internal reflection microscopy. *Mol. Biol. Cell* **15,** 4658–4668 (2004).

32. Anantharam, A., Onoa, B., Edwards, R. H., Holz, R. W. & Axelrod, D. Localized topological changes of the plasma membrane upon exocytosis visualized by polarized TIRFM. *J. Cell Biol.* **188,** 415–428 (2010).

33. Axelrod, D. Carbocyanine dye orientation in red cell membrane studied by microscopic fluorescence polarization. *Biophys. J.* **26,** 557–573 (1979).

34. Anantharam, A., Axelrod, D. & Holz, R. W. Polarized TIRFM Reveals Changes in Plasma Membrane Topology Before and During Granule Fusion. *Cell Mol. Neurobiol.* **30,** 1343–1349 (2010).

35. Kiessling, V., Domanska, M. K. & Tamm, L. K. Single SNARE-Mediated Vesicle Fusion Observed In Vitro by Polarized TIRFM. *Biophys. J.* **99,** 4047–4055 (2010).

36. Oreopoulos, J. & Yip, C. M. Combinatorial microscopy for the study of protein-membrane interactions in supported lipid bilayers: Order parameter measurements by combined polarized TIRFM/AFM. *J. Struct. Biol.* **168,** 21–36 (2009).

37. Beausang, J. F., Schroeder, H. W., Nelson, P. C. & Goldman, Y. E. Twirling of Actin by Myosins II and V Observed via Polarized TIRF in a Modified Gliding Assay. *Biophys. J.* **95,** 5820–5831 (2008).

38. Sridharan, R., Zuber, J., Connelly, S. M., Mathew, E. & Dumont, M. E. Fluorescent approaches for understanding interactions of ligands with G protein coupled receptors. *Biochim. Biophys. Acta BBA - Biomembr.* **1838,** 15–33 (2014).

39. Armendariz, K. P. & Dunn, R. C. Ganglioside Influence on Phospholipid Films Investigated with Single Molecule Fluorescence Measurements. *J. Phys. Chem. B* **117,** 7959–7966 (6).

40. Anantharam, A., Axelrod, D. & Holz, R. W. Real-time imaging of plasma membrane deformations reveals pre-fusion membrane curvature changes and a role for dynamin in the regulation of fusion pore expansion. *J. Neurochem.* **122,** 661–671 (2012).

41. Lipson, S. G., Lipson, H. & Tannhauser, D. S. *Optical physics*. (Cambridge, U.K. ; New York, N.Y. : Cambridge University Press, 1995).

42. Zipfel, W. R., Williams, R. M. & Webb, W. W. Nonlinear magic: multiphoton microscopy in the biosciences. *Nat. Biotechnol.* **21,** 1369–1377 (2003).

43. Benda, A., Aitken, H., Davies, D. S., Whan, R. & Goldsbury, C. STED imaging of tau filaments in Alzheimer's disease cortical grey matter. *J. Struct. Biol.* **195,** 345–352 (2016).

44. Schaller, R. D. *et al.* Nonlinear Chemical Imaging Nanomicroscopy: From Second and Third Harmonic Generation to Multiplex (Broad-Bandwidth) Sum Frequency Generation Near-Field Scanning Optical Microscopy. *J. Phys. Chem. B* **106,** 5143–5154 (2002).

45. Rust, M. J., Bates, M. & Zhuang, X. Sub-diffraction-limit imaging by stochastic optical reconstruction microscopy (STORM). *Nat. Methods* **3,** 793–796 (2006).

46. Betzig, E. *et al.* Imaging intracellular fluorescent proteins at nanometer resolution. *Science* **313,** 1642–1645 (2006).

47. Hess, S. T., Girirajan, T. P. K. & Mason, M. D. Ultra-High Resolution Imaging by Fluorescence Photoactivation Localization Microscopy. *Biophys. J.* **91,** 4258–4272 (2006).

48. Zondervan, R., Kulzer, F., Orlinskii, S. B. & Orrit, M. Photoblinking of Rhodamine 6G in Poly(vinyl alcohol): Radical Dark State Formed through the Triplet. *J. Phys. Chem. A* **107,** 6770–6776 (2003).

49. Dempsey, G. T., Vaughan, J. C., Chen, K. H., Bates, M. & Zhuang, X. Evaluation of fluorophores for optimal performance in localization-based super-resolution imaging. *Nat. Methods* **8,** 1027–1036 (2011).

50. Geertsema, H. J. *et al.* Single-Molecule Imaging at High Fluorophore Concentrations by Local Activation of Dye. *Biophys. J.* **108,** 949–956 (2015).

51. Heilemann, M. *et al.* Subdiffraction-Resolution Fluorescence Imaging with Conventional Fluorescent Probes. *Angew. Chem. Int. Ed.* **47,** 6172–6176 (2008).

52. Steinhauer, C., Forthmann, C., Vogelsang, J. & Tinnefeld, P. Superresolution Microscopy on the Basis of Engineered Dark States. *J. Am. Chem. Soc.* **130,** 16840–16841 (2008).

53. Shi, X., Lim, J. & Ha, T. Acidification of the Oxygen Scavenging System in Single-Molecule Fluorescence Studies: In Situ Sensing with a Ratiometric Dual-Emission Probe. *Anal. Chem.* **82,** 6132–6138 (2010).

54. Vogelsang, J., Cordes, T. & Tinnefeld, P. Single-molecule photophysics of oxazines on DNA and its application in a FRET switch. *Photochem. Photobiol. Sci.* **8,** 486–496 (2009).

55. Olivier, N., Keller, D., Rajan, V. S., Gönczy, P. & Manley, S. Simple buffers for 3D STORM microscopy. *Biomed. Opt. Express* **4,** 885–899 (2013).

56. Thompson, R. E., Larson, D. R. & Webb, W. W. Precise Nanometer Localization Analysis for Individual Fluorescent Probes. *Biophys. J.* **82,** 2775–2783 (2002).

57. Farrow, C. L., Shaw, M., Kim, H., Juhás, P. & Billinge, S. J. L. Nyquist-Shannon sampling theorem applied to refinements of the atomic pair distribution function. *Phys. Rev. B* **84,** 134105 (2011).

58. Huang, B., Jones, S. A., Brandenburg, B. & Zhuang, X. Whole-cell 3D STORM reveals interactions between cellular structures with nanometer-scale resolution. *Nat. Methods* **5,** 1047–1052 (2008).

59. Huang, B., Wang, W., Bates, M. & Zhuang, X. Three-Dimensional Super-Resolution Imaging by Stochastic Optical Reconstruction Microscopy. *Science* **319,** 810–813 (2008).

60. Shtengel, G. *et al.* Interferometric fluorescent super-resolution microscopy resolves 3D cellular ultrastructure. *Proc. Natl. Acad. Sci. U. S. A.* **106,** 3125–3130 (2009).

61. Juette, M. F. *et al.* Three-dimensional sub-100 nm resolution fluorescence microscopy of thick samples. *Nat. Methods* **5,** 527–529 (2008).

62. Aguet, F., Geissbühler, S., Märki, I., Lasser, T. & Unser, M. Super-resolution orientation estimation and localization of fluorescent dipoles using 3-D steerable filters. *Opt. Express* **17,** 6829–6848 (2009).

63. Backlund, M. P. *et al.* Simultaneous, accurate measurement of the 3D position and orientation of single molecules. *Proc. Natl. Acad. Sci. U. S. A.* **109,** 19087–19092 (2012).

64. Backer, A. S., Backlund, M. P., Lew, M. D. & Moerner, W. E. Single-molecule orientation measurements with a quadrated pupil. *Opt. Lett.* **38,** 1521–1523 (2013).

65. Gould, T. J. *et al.* Nanoscale imaging of molecular positions and anisotropies. *Nat. Methods* **5,** 1027–1030 (2008).

66. Patra, D., Gregor, I. & Enderlein, J. Image Analysis of Defocused Single-Molecule Images for Three-Dimensional Molecule Orientation Studies. *J. Phys. Chem. A* **108,** 6836–6841 (2004).

67. Lieb, M. A., Zavislan, J. M. & Novotny, L. Single-molecule orientations determined by direct emission pattern imaging. *J. Opt. Soc. Am. B* **21,** 1210 (2004).

68. Syed, S., Snyder, G. E., Franzini-Armstrong, C., Selvin, P. R. & Goldman, Y. E. Adaptability of myosin V studied by simultaneous detection of position and orientation. *EMBO J.* **25,** 1795–1803 (2006).

69. Pavani, S. R. P. *et al.* Three-dimensional, single-molecule fluorescence imaging beyond the diffraction limit by using a double-helix point spread function. *Proc. Natl. Acad. Sci. U. S. A.* **106,** 2995–2999 (2009).

70. Sick, B., Hecht, B. & Novotny, L. Orientational imaging of single molecules by annular illumination. *Phys. Rev. Lett.* **85,** 4482–4485 (2000).

71. Sinkó, J., Gajdos, T., Czvik, E., Szabó, G. & Erdélyi, M. Polarization sensitive localization based super-resolution microscopy with a birefringent wedge. *Methods Appl. Fluoresc.* **5,** 017001 (2017).

72. McMahon, H. T. & Boucrot, E. Membrane curvature at a glance. *J. Cell Sci.* **128,** 1065–1070 (2015).

73. Kozlov, M. M., McMahon, H. T. & Chernomordik, L. V. Protein-driven membrane stresses in fusion and fission. *Trends Biochem. Sci.* **35,** 699–706 (2010).

74. Ono, A. Viruses and Lipids. *Viruses* **2,** 1236–1238 (2010).

75. Kelly, C. V. *et al.* Stoichiometry and Structure of Poly(amidoamine) Dendrimer−Lipid Complexes. *ACS Nano* **3,** 1886–1896 (2009).

76. McMahon, H. T. & Gallop, J. L. Membrane curvature and mechanisms of dynamic cell membrane remodelling. *Nature* **438,** 590–596 (2005).

77. Raposo, G. & Stoorvogel, W. Extracellular vesicles: exosomes, microvesicles, and friends. *J. Cell Biol.* **200,** 373–383 (2013).

78. Baumgart, T., Capraro, B. R., Zhu, C. & Das, S. L. Thermodynamics and Mechanics of Membrane Curvature Generation and Sensing by Proteins and Lipids. *Annu. Rev. Phys. Chem.* **62,** 483–506 (2011).

79. Zimmerberg, J. & Kozlov, M. M. How proteins produce cellular membrane curvature. *Nat. Rev. Mol. Cell Biol.* **7,** 9–19 (2006).

80. Stachowiak, J. C. *et al.* Membrane bending by protein-protein crowding. *Nat. Cell Biol.* **14,** 944–949 (2012).

81. van de Linde, S. *et al.* Direct stochastic optical reconstruction microscopy with standard fluorescent probes. *Nat. Protoc.* **6,** 991–1009 (2011).

82. Sund, S. E., Swanson, J. A. & Axelrod, D. Cell Membrane Orientation Visualized by Polarized Total Internal Reflection Fluorescence. *Biophys. J.* **7,** 2266–2283 (1999).

83. Anantharam, A., Onoa, B., Edwards, R. H., Holz, R. W. & Axelrod, D. Localized topological changes of the plasma membrane upon exocytosis visualized by polarized TIRFM. *J. Cell Biol.* **188,** 415–428 (2010).

84. Hellen E., H., Fulbright R., M. & Axelrod, D. Total internal reflection fluorescence: theory and applications at biosurfaces. *Spectrosc. Membr. Probes* 47–79 (1988).

85. Veatch, S. Electro-Formation and Fluorescence Microscopy of Giant Vesicles With Coexisting Liquid Phases. in *Lipid Rafts* (ed. McIntosh, T.) **398,** 59–72 (Humana Press, 2007).

86. Ovesný, M., Křížek, P., Borkovec, J., Švindrych, Z. & Hagen, G. M. ThunderSTORM: a comprehensive ImageJ plug-in for PALM and STORM data analysis and super-resolution imaging. *Bioinformatics* **30,** 2389–2390 (2014).

87. Ewers, H. *et al.* Single-particle tracking of murine polyoma virus-like particles on live cells and artificial membranes. *Proc. Natl. Acad. Sci. U. S. A.* **102,** 15110–15115 (2005).

88. Manley, S. *et al.* High-density mapping of single-molecule trajectories with photoactivated localization microscopy. *Nat. Methods* **5,** 155–157 (2008).

89. Lagerholm, B. C., Andrade, D. M., Clausen, M. P. & Eggeling, C. Convergence of lateral dynamic measurements in the plasma membrane of live cells from single particle tracking and STED-FCS. *J. Phys. Appl. Phys.* **50,** 063001 (2017).

90. Kabbani, A. M., Woodward, X. & Kelly, C. V. Resolving the effects of nanoscale membrane curvature on lipid mobility. *ArXiv170600087 Phys.* (2017).

91. Soumpasis, D. M. Theoretical analysis of fluorescence photobleaching recovery experiments. *Biophys. J.* **41,** 95–97 (1983).

92. Veatch, S. L. *et al.* Correlation Functions Quantify Super-Resolution Images and Estimate Apparent Clustering Due to Over-Counting. *PLOS ONE* **7,** 1–13 (2012).

93. Veatch, S. L. *et al.* Correlation Functions Quantify Super-Resolution Images and Estimate Apparent Clustering Due to Over-Counting. *PLOS ONE* **7,** 1–13 (2012).

94. Black, J. C., Cheney, P. P., Campbell, T. & Knowles, M. K. Membrane curvature based lipid sorting using a nanoparticle patterned substrate. *Soft Matter* **10,** 2016–2023 (2014).

95. Kunding, A. H., Mortensen, M. W., Christensen, S. M. & Stamou, D. A fluorescence-based technique to construct size distributions from single-object measurements: application to the extrusion of lipid vesicles. *Biophys. J.* **95,** 1176–1188 (2008).

96. Hsieh, W.-T. *et al.* Curvature Sorting of Peripheral Proteins on Solid-Supported Wavy Membranes. *Langmuir* **28,** 12838–12843 (2012).

97. Ryu, Y.-S. *et al.* Reconstituting ring-rafts in bud-mimicking topography of model membranes. *Nat Commun* **5,** (2014).

98. Ogunyankin, M. O., Huber, D. L., Sasaki, D. Y. & Longo, M. L. Nanoscale Patterning of Membrane-Bound Proteins Formed through Curvature-Induced Partitioning of Phase-Specific Receptor Lipids. *Langmuir* **29,** 6109–6115 (2013).

99. Sanii, B., Smith, A. M., Butti, R., Brozell, A. M. & Parikh, A. N. Bending membranes on demand: fluid phospholipid bilayers on topographically deformable substrates. *Nano Lett.* **8,** 866–871 (2008).

100. Gilmore, S. F., Nanduri, H. & Parikh, A. N. Programmed Bending Reveals Dynamic Mechanochemical Coupling in Supported Lipid Bilayers. *PLoS ONE* **6,** (2011).

101. Cheney, P. P., Weisgerber, A. W., Feuerbach, A. M. & Knowles, M. K. Single Lipid Molecule Dynamics on Supported Lipid Bilayers with Membrane Curvature. *Membranes* **7,** (2017).

102. Roiter, Y. *et al.* Interaction of Nanoparticles with Lipid Membrane. *Nano Lett.* **8,** 941–944 (2008).

103. Larsen, J. B. *et al.* Membrane curvature enables N-Ras lipid anchor sorting to liquid-ordered membrane phases. *Nat. Chem. Biol.* **11,** 192–194 (2015).

104. Lew, M. D., Backlund, M. P. & Moerner, W. E. Rotational mobility of single molecules affects localization accuracy in super-resolution fluorescence microscopy. *Nano Lett.* **13,** 3967–3972 (2013).

105. Agrawal, A., Quirin, S., Grover, G. & Piestun, R. Limits of 3D dipole localization and orientation estimation for single-molecule imaging: towards Green's tensor engineering. *Opt. Express* **20,** 26667–26680 (2012).

106. Kabbani, A. M. & Kelly, C. V. Nanoscale membrane budding induced by CTxB on quasi-one component lipid bilayers detected by polarized localization microscopy. *ArXiv170308865 Phys.* (2017).

107. Bag, N., Yap, D. H. X. & Wohland, T. Temperature dependence of diffusion in model and live cell membranes characterized by imaging fluorescence correlation spectroscopy. *Biochim. Biophys. Acta* **1838,** 802–813 (2014).

108. Sharonov, A. & Hochstrasser, R. M. Wide-field subdiffraction imaging by accumulated binding of diffusing probes. *Proc. Natl. Acad. Sci.* **103,** 18911–18916 (2006).

109. Shim, S.-H. *et al.* Super-resolution fluorescence imaging of organelles in live cells with photoswitchable membrane probes. *Proc. Natl. Acad. Sci. U. S. A.* **109,** 13978–13983 (2012).

110. Dempsey, G. T. *et al.* Photoswitching Mechanism of Cyanine Dyes. *J. Am. Chem. Soc.* **131,** 18192–18193 (2009).

111. Heinrich, M., Tian, A., Esposito, C. & Baumgart, T. Dynamic sorting of lipids and proteins in membrane tubes with a moving phase boundary. *Proc. Natl. Acad. Sci.* **107,** 7208–7213 (2010).

112. A., T. & T., B. Sorting of Lipids and Proteins in Membrane Curvature Gradients. *Biophys. J.* **96,** 2676–2688 (2009).

113. Mikhalyov, I. & Samsonov, A. Lipid raft detecting in membranes of live erythrocytes. *Biochim. Biophys. Acta BBA - Biomembr.* **1808,** 1930–1939 (2011).

114. Baumgart, T. *et al.* Large-scale fluid/fluid phase separation of proteins and lipids in giant plasma membrane vesicles. *Proc. Natl. Acad. Sci. U. S. A.* **104,** 3165–3170 (2007).

115. Day, C. A. & Kenworthy, A. K. Functions of cholera toxin B-subunit as a raft cross-linker. *Essays Biochem.* **57,** 135–145 (2015).

116. Hammond, A. T. *et al.* Crosslinking a lipid raft component triggers liquid ordered-liquid disordered phase separation in model plasma membranes. *Proc. Natl. Acad. Sci. U. S. A.* **102,** 6320–6325 (2005).

117. Windschiegl, B. *et al.* Lipid Reorganization Induced by Shiga Toxin Clustering on Planar Membranes. *PLoS ONE* **4,** (2009).

118. Chinnapen, D. J.-F. *et al.* Lipid-sorting by ceramide structure from plasma membrane to ER for the cholera toxin receptor ganglioside GM1. *Dev. Cell* **23,** 573–586 (2012).

119. Ewers, H. *et al.* GM1 structure determines SV40-induced membrane invagination and infection. *Nat. Cell Biol.* **12,** 11–18 (2010).

120. Yanagisawa, K. GM1 ganglioside and the seeding of amyloid in Alzheimer's disease: endogenous seed for Alzheimer amyloid. *Neurosci. Rev. J. Bringing Neurobiol. Neurol. Psychiatry* **11,** 250–260 (2005).

121. Yanagisawa, K., Odaka, A., Suzuki, N. & Ihara, Y. GM1 ganglioside-bound amyloid beta-protein (A beta): a possible form of preamyloid in Alzheimer's disease. *Nat. Med.* **1,** 1062–1066 (1995).

122. Wolf, A. A., Fujinaga, Y. & Lencer, W. I. Uncoupling of the cholera toxin-G(M1) ganglioside receptor complex from endocytosis, retrograde Golgi trafficking, and downstream signal transduction by depletion of membrane cholesterol. *J. Biol. Chem.* **277,** 16249–16256 (2002).

123. Stoddart, A., Jackson, A. P. & Brodsky, F. M. Plasticity of B cell receptor internalization upon conditional depletion of clathrin. *Mol. Biol. Cell* **16,** 2339–2348 (2005).

124. Moens, P. D. J., Digman, M. A. & Gratton, E. Modes of diffusion of cholera toxin bound to GM1 on live cell membrane by image mean square displacement analysis. *Biophys. J.* **108,** 1448–1458 (2015).

125. Spillane, K. M. *et al.* High-Speed Single-Particle Tracking of GM1 in Model Membranes Reveals Anomalous Diffusion due to Interleaflet Coupling and Molecular Pinning. *Nano Lett.* **14,** 5390–5397 (2014).

126. Hsieh, C.-L., Spindler, S., Ehrig, J. & Sandoghdar, V. Tracking Single Particles on Supported Lipid Membranes: Multimobility Diffusion and Nanoscopic Confinement. *J. Phys. Chem. B* **118,** 1545–1554 (2014).

127. Kirkham, M. *et al.* Ultrastructural identification of uncoated caveolin-independent early endocytic vehicles. *J. Cell Biol.* **168,** 465–476 (2005).

128. Lajoie, P. *et al.* Caveolin-1 regulation of dynamin-dependent, raft-mediated endocytosis of cholera toxin–B sub-unit occurs independently of caveolae. *J. Cell. Mol. Med.* **13,** 3218–3225 (2009).

129. Montesano, R., Roth, J., Robert, A. & Orci, L. Non-coated membrane invaginations are involved in binding and internalization of cholera and tetanus toxins. *Nature* **296,** 651–653 (1982).

130. Römer, W. *et al.* Shiga toxin induces tubular membrane invaginations for its uptake into cells. *Nature* **450,** 670–675 (2007).

131. Day, C. A. *et al.* Microtubule motors power plasma membrane tubulation in clathrin-independent endocytosis. *Traffic Cph. Den.* **16,** 572–590 (2015).

132. Pezeshkian, W. *et al.* Membrane invagination induced by Shiga toxin B-subunit: from molecular structure to tube formation. *Soft Matter* **12,** 5164–5171 (2016).

133. Kabbani, A. M. & Kelly, C. V. The Detection of Nanoscale Membrane Bending with Polarized Localization Microscopy. *https://arxiv.org/abs/1703.01498* **Biophys J Manuscript Number: 2017BIOPHYSJ307664,** (2017).

134. Dempsey, G. T. *et al.* Photoswitching mechanism of cyanine dyes. *J. Am. Chem. Soc.* **131,** 18192–18193 (2009).

135. Sund, S. E., Swanson, J. A. & Axelrod, D. Cell membrane orientation visualized by polarized total internal reflection fluorescence. *Biophys. J.* **77,** 2266–2283 (1999).

136. Veatch, S. Electro-Formation and Fluorescence Microscopy of Giant Vesicles With Coexisting Liquid Phases. in *Lipid Rafts* (ed. McIntosh, T.) **398,** 59–72 (Humana Press, 2007).

137. Shim, S.-H. *et al.* Super-resolution fluorescence imaging of organelles in live cells with photoswitchable membrane probes. *Proc. Natl. Acad. Sci. U. S. A.* **109,** 13978–13983 (2012).

138. Lobovkina, T. *et al.* Protrusive growth and periodic contractile motion in surface-adhered vesicles induced by Ca2+-gradients. *Soft Matter* **6,** 268–272 (2010).

139. Kaizuka, Y. & Groves, J., T. Bending-mediated superstructural organizations in phase-separated lipid membranes. *New J. Phys.* **12,** (2010).

140. Sackmann, E. Supported membranes: Scientific and practical applications. *Science* **271,** 43–48 (1996).

141. Spillane, K. M. *et al.* High-Speed Single-Particle Tracking of GM1 in Model Membranes Reveals Anomalous Diffusion due to Interleaflet Coupling and Molecular Pinning. *Nano Lett.* **14,** 5390–5397 (2014).

142. Hsieh, C.-L., Spindler, S., Ehrig, J. & Sandoghdar, V. Tracking Single Particles on Supported Lipid Membranes: Multimobility Diffusion and Nanoscopic Confinement. *J. Phys. Chem. B* **118,** 1545–1554 (2014).

143. Zhao, J., Wu, J. & Veatch, S. L. Adhesion Stabilizes Robust Lipid Heterogeneity in Supercritical Membranes at Physiological Temperature. *Biophys. J.* **104,** 825–834 (2013).

144. Hartman, K. L., Kim, S., Kim, K. & Nam, J.-M. Supported lipid bilayers as dynamic platforms for tethered particles. *Nanoscale* **7,** 66–76 (2015).

145. Kelly, C. V., Wakefield, D. L., Holowka, D. A., Craighead, H. G. & Baird, B. A. Near-field fluorescence cross-correlation spectroscopy on planar membranes. *ACS Nano* **8,** 7392–7404 (2014).

146. Kaiser, H.-J. *et al.* Order of lipid phases in model and plasma membranes. *Proc. Natl. Acad. Sci. U. S. A.* **106,** 16645–16650 (2009).

147. Glebov, O. O. & Nichols, B. J. Lipid raft proteins have a random distribution during localized activation of the T-cell receptor. *Nat. Cell Biol.* **6,** 238–243 (2004).

148. Stone, M. B. & Veatch, S. L. Steady-state cross-correlations for live two-colour super-resolution localization data sets. *Nat. Commun.* **6,** 7347 (2015).

149. Day, C. A. & Kenworthy, A. K. Mechanisms Underlying the Confined Diffusion of Cholera Toxin B-Subunit in Intact Cell Membranes. *PLoS ONE* **7,** e34923 (2012).

150. Day, C. A. & Kenworthy, A. K. Mechanisms underlying the confined diffusion of cholera toxin B-subunit in intact cell membranes. *PloS One* **7,** e34923 (2012).

151. van Zanten, T. S. *et al.* Direct mapping of nanoscale compositional connectivity on intact cell membranes. *Proc. Natl. Acad. Sci. U. S. A.* **107,** 15437–15442 (2010).

152. Štefl, M. *et al.* Dynamics and Size of Cross-Linking-Induced Lipid Nanodomains in Model Membranes. *Biophys. J.* **102,** 2104–2113 (2012).

153. Watkins, E. B., Miller, C. E., Majewski, J. & Kuhl, T. L. Membrane texture induced by specific protein binding and receptor clustering: active roles for lipids in cellular function. *Proc. Natl. Acad. Sci. U. S. A.* **108,** 6975–6980 (2011).

154. Johannes, L. & Mayor, S. Induced domain formation in endocytic invagination, lipid sorting, and scission. *Cell* **142,** 507–510 (2010).

155. Basu, I. & Mukhopadhyay, C. Insights into Binding of Cholera Toxin to GM1 Containing Membrane. *Langmuir* **30,** 15244–15252 (2014).

156. Black, J. C., Cheney, P. P., Campbell, T. & Knowles, M. K. Membrane curvature based lipid sorting using a nanoparticle patterned substrate. *Soft Matter* **10,** 2016–2023 (2014).

157. Becucci, L., Vizza, F., Duarte, Y. & Guidelli, R. The GM1 Ganglioside Forms GM1-Rich Gel Phase Microdomains within Lipid Rafts. *Coatings* **4,** 450 (2014).

158. Helfrich, W. Elastic properties of lipid bilayers: theory and possible experiments. *Z. Naturforschung Teil C Biochem. Biophys. Biol. Virol.* **28,** 693–703 (1973).

159. Dimova, R. Recent developments in the field of bending rigidity measurements on membranes. *Adv. Colloid Interface Sci.* **208,** 225–234 (2014).

160. Siegel, D. P. & Kozlov, M. M. The Gaussian Curvature Elastic Modulus of N-Monomethylated Dioleoylphosphatidylethanolamine: Relevance to Membrane Fusion and Lipid Phase Behavior. *Biophys. J.* **87,** 366–374 (2004).

161. Tachev, K. D., Angarska, J. K., Danov, K. D. & Kralchevsky, P. A. Erythrocyte attachment to substrates: determination of membrane tension and adhesion energy. *Colloids Surf. B Biointerfaces* **19,** 61–80 (2000).

162. Turnbull, W. B., Precious, B. L. & Homans, S. W. Dissecting the cholera toxin-ganglioside GM1 interaction by isothermal titration calorimetry. *J. Am. Chem. Soc.* **126,** 1047–1054 (2004).

163. Sun, H., Chen, L., Gao, L. & Fang, W. Nanodomain Formation of Ganglioside GM1 in Lipid Membrane: Effects of Cholera Toxin-Mediated Cross-Linking. *Langmuir ACS J. Surf. Colloids* **31,** 9105–9114 (2015).

164. Kabaso, D., Lokar, M., Kralj-Iglič, V., Veranič, P. & Iglič, A. Temperature and cholera toxin B are factors that influence formation of membrane nanotubes in RT4 and T24 urothelial cancer cell lines. *Int. J. Nanomedicine* **6,** 495–509 (2011).

165. Shi, J. *et al.* GM1 clustering inhibits cholera toxin binding in supported phospholipid membranes. *J. Am. Chem. Soc.* **129,** 5954–5961 (2007).

166. Sridhar, A., Kumar, A. & Dasmahapatra, A. K. Multi-scale molecular dynamics study of cholera pentamer binding to a GM1-phospholipid membrane. *J. Mol. Graph. Model.* **68,** 236–251 (2016).

167. Raghunathan, K. *et al.* Glycolipid Crosslinking Is Required for Cholera Toxin to Partition Into and Stabilize Ordered Domains. *Biophys. J.* **111,** 2547–2550 (2016).

168. Grover, C. N. *et al.* Crosslinking and composition influence the surface properties, mechanical stiffness and cell reactivity of collagen-based films. *Acta Biomater.* **8,** 3080–3090 (2012).

169. Tseng, Y. *et al.* How actin crosslinking and bundling proteins cooperate to generate an enhanced cell mechanical response. *Biochem. Biophys. Res. Commun.* **334,** 183–192 (2005).

170. Liang, H.-C., Chang, Y., Hsu, C.-K., Lee, M.-H. & Sung, H.-W. Effects of crosslinking degree of an acellular biological tissue on its tissue regeneration pattern. *Biomaterials* **25,** 3541–3552 (2004).

171. Chazal, N. & Gerlier, D. Virus entry, assembly, budding, and membrane rafts. *Microbiol. Mol. Biol. Rev. MMBR* **67,** 226–237, table of contents (2003).

172. Janes, P. W., Ley, S. C. & Magee, A. I. Aggregation of Lipid Rafts Accompanies Signaling via the T Cell Antigen Receptor. *J. Cell Biol.* **147,** 447–461 (1999).

173. Grakoui, A. *et al.* The immunological synapse: a molecular machine controlling T cell activation. *Science* **285,** 221–227 (1999).

174. Calcium-Dependent Lateral Organization in Phosphatidylinositol 4,5-Bisphosphate (PIP2)- and Cholesterol-Containing Monolayers - Biochemistry (ACS Publications). Available at: http://pubs.acs.org/doi/abs/10.1021/bi9007879. (Accessed: 15th June 2017)

175. Wong, J., Chilkoti, A. & Moy, V. T. Direct force measurements of the streptavidin-biotin interaction. *Biomol. Eng.* **16,** 45–55 (1999).

176. Honigmann, A. *et al.* A lipid bound actin meshwork organizes liquid phase separation in model membranes. *eLife* **3,** e01671 (2014).

177. Momin, N. *et al.* Designing lipids for selective partitioning into liquid ordered membrane domains. *Soft Matter* **11,** 3241–3250 (2015).

178. Darst, S. A. *et al.* Two-dimensional crystals of streptavidin on biotinylated lipid layers and their interactions with biotinylated macromolecules. *Biophys. J.* **59,** 387–396 (1991).

179. Jacobson, K., Mouritsen, O. G. & Anderson, R. G. W. Lipid rafts: at a crossroad between cell biology and physics. *Nat. Cell Biol.* **9,** 7–14 (2007).

180. Polka-Dotted Vesicles: Lipid Bilayer Dynamics and Cross-Linking Effects - Langmuir (ACS Publications). Available at: http://pubs.acs.org/doi/abs/10.1021/la3042007. (Accessed: 15th June 2017)

181. Meerschaert, R. L. & Kelly, C. V. Trace membrane additives affect lipid phases with distinct mechanisms: a modified Ising model. *Eur. Biophys. J. EBJ* **44,** 227–233 (2015).

182. Hughes, L. D., Rawle, R. J. & Boxer, S. G. Choose Your Label Wisely: Water-Soluble Fluorophores Often Interact with Lipid Bilayers. *PLoS ONE* **9,** (2014).

183. Quantitative comparison of long-wavelength Alexa Fluor dyes to Cy dyes: fluorescence of the dyes and their bioconjugates. - PubMed - NCBI. Available at: https://www.ncbi.nlm.nih.gov/pubmed/14623938. (Accessed: 15th June 2017)

184. Manley, S., Horton, M. R., Lecszynski, S. & Gast, A. P. Sorting of Streptavidin Protein Coats on Phase-Separating Model Membranes. *Biophys. J.* **95,** 2301–2307 (2008).

185. Bacia, K., Schwille, P. & Kurzchalia, T. Sterol structure determines the separation of phases and the curvature of the liquid-ordered phase in model membranes. *Proc. Natl. Acad. Sci. U. S. A.* **102,** 3272–3277 (2005).

186. Korlach, J., Schwille, P., Webb, W. W. & Feigenson, G. W. Characterization of lipid bilayer phases by confocal microscopy and fluorescence correlation spectroscopy. *Proc. Natl. Acad. Sci. U. S. A.* **96,** 8461–8466 (1999).

187. Li, L. & Cheng, J.-X. Coexisting Stripe and Patch Shaped Domains in Giant Unilamellar Vesicles. *Biochemistry (Mosc.)* **45,** 11819–11826 (2006).

188. Pezeshkian, W., Nåbo, L. J. & Ipsen, J. H. Cholera toxin B subunit induces local curvature on lipid bilayers. *FEBS Open Bio* **7,** 1638–1645 (2017).

189. Shelby, S. A., Holowka, D., Baird, B. & Veatch, S. L. Distinct Stages of Stimulated FcεRI Receptor Clustering and Immobilization Are Identified through Superresolution Imaging. *Biophys. J.* **105,** 2343–2354 (2013).

190. Lu, B., Huang, X., Mo, J. & Zhao, W. Drug Delivery Using Nanoparticles for Cancer Stem-Like Cell Targeting. *Front. Pharmacol.* **7,** (2016).

191. Green, N. M. Avidin. 1. The use of [14C]biotin for kinetic studies and for assay. *Biochem. J.* **89,** 585–591 (1963).

192. Lauer, S., Goldstein, B., Nolan, R. L. & Nolan, J. P. Analysis of cholera toxin-ganglioside interactions by flow cytometry. *Biochemistry (Mosc.)* **41,** 1742–1751 (2002).

193. Schoen, A. & Freire, E. Thermodynamics of intersubunit interactions in cholera toxin upon binding to the oligosaccharide portion of its cell surface receptor, ganglioside GM1. *Biochemistry (Mosc.)* **28,** 5019–5024 (1989).

194. Kabbani, A. M., Woodward, X. & Kelly, C. V. Revealing the Effects of Nanoscale Membrane Curvature on Lipid Mobility. *Membranes* **7,** (2017).

195. Schneider, S. W., Sritharan, K. C., Geibel, J. P., Oberleithner, H. & Jena, B. P. Surface dynamics in living acinar cells imaged by atomic force microscopy: Identification of plasma membrane structures involved in exocytosis. *Proc. Natl. Acad. Sci.* **94,** 316–321 (1997).

196. Rajagopal, A. *et al.* Proteome of the insulin-secreting Min6 cell porosome complex: involvement of Hsp90 in its assembly and function. *J. Proteomics* **114,** 83–92 (2015).

197. Bacia, K., Schuette, C. G., Kahya, N., Jahn, R. & Schwille, P. SNAREs Prefer Liquid-disordered over "Raft" (Liquid-ordered) Domains When Reconstituted into Giant Unilamellar Vesicles. *J. Biol. Chem.* **279,** 37951–37955 (2004).

ABSTRACT

POLARIZED LOCALIZATION MICROSCOPY (PLM) DETECTS NANOSCALE MEMBRANE CURVATURE AND INDUCED BUDDING BY CHOLERA TOXIN SUBUNIT B (CTxB)

by

ABIR KABBANI

May 2018

Advisor: Dr. Christopher V. Kelly

Major: Physics

Degree: Doctor of Philosophy

The curvature of biological membranes at the nanometer scale is critically important for vesicle trafficking, organelle morphology, and disease propagation. Many proteins and lipids interact with diverse curvature sensing and curvature generating mechanisms. Deciphering the molecular mechanisms of toxin-membrane interactions has been limited by the resolution and drawbacks of conventional experimental techniques. This study reveals the inherent membrane bending capability of cholera toxin subunit B (CTxB) through the development and implementation of Polarized Localization Microscopy (PLM). PLM is a pointillist optical imaging technique for the detection of nanoscale membrane curvature in correlation with single-molecule dynamics and molecular sorting.

PLM combines polarized total internal reflection fluorescence microscopy and fluorescence localization microscopy to reveal membrane orientation without reducing localization precision by point spread function manipulation. Further, membrane curvature detection with PLM requires ≤19% of the localization density required with 3D fluorescence localization microscopy (*e.g.*, PALM or STORM). Engineered hemispherical membrane curvature

with varying radii of 24, 51, and 70 nm were detected with PLM while surrounded by planar supported lipid bilayers. Nanoscale membrane bud growth was spontaneously induced by CTxB on otherwise planar, quasi-one component lipid bilayers, revealing a mechanism of cholera immobilization and cellular internalization. The single lipid and single protein trajectories further quantified the effects of nanoscale membrane curvature and protein-lipid interactions. CTxB sorting to high membrane curvatures was detected and quantified.

Nanoscale membrane budding and tubulation was mainly driven by CTxB valency and structure. We demonstrated that varying either GM1 or CTxB concentrations on the membrane affects the budding structures. The number of crosslinked GM1s to a single CTxB affected the toxin behavior and mechanism on the membrane. Changing the lipid structure altered the bending mechanism and the eventual size and density of induced buds. Through future incorporation of single-particle tracking and live cells, PLM is poised to image the diverse molecular mechanisms that regulate nanoscale membrane bending.

AUTOBIOGRAPHICAL STATEMENT

Education

2011-2018 Doctor of Philosophy in Physics, Wayne State University, Detroit MI

2011-2013 M.S. in Physics, Wayne State University, Detroit MI

2007-2011 Bachelor of Science in Physics, Beirut Arab University, Beirut, Lebanon

Awards

2017 Professor Eugene Victor Perrin, M.D. Endowed Memorial Scholarship

2017 Summer Dissertation Fellowship, Wayne State University

2017 Third place Best Poster Award, Graduate Exhibition, and Wayne State University

2017 Educational Travel Award, 60th Annual Meeting of Biophysical Society

2016 First place Best Poster Award, Lipids @ Wayne Symposium, Wayne State University

2016 First place Best Poster Award, 7th Annual Physics Graduate Research Day, Wayne State University

2016 Third place Best Poster Award, 7th Annual Graduate and Postdoctoral Symposium, Wayne State University

2016 Richard Barber Fellowship, Wayne State University

2016 Teaching Award, Wayne State University

2016 MAC Travel Award, 59th Annual Meeting of Biophysical Society

2015 Second place Best Poster Award, 6th Annual Physics Graduate Research Day, Wayne State University

2015 First place Best Poster Award, 6th Annual Graduate and Postdoctoral Symposium, Wayne State University

2014 Second place Best Poster Award, 5th Annual Physics Graduate Research Day, Wayne State University

2014-2015 Thomas C. Rumble Fellowship, Wayne State University